UNIVERSITA’ DEGLI STUDI DI PADOVA

DIPARTIMENTO DI SCIENZE CHIMICHE

CORSO DI LAUREA MAGISTRALE IN CHIMICA

TESI DI LAUREA MAGISTRALE

Synthesis and study of catalytic antioxidant activity of mono and dinuclear copper(II) complexes

Relatore: Prof. Mauro Carraro

Controrelatore: Prof. Andrea Biffis

Laureanda: Martina Chianese
1155578

Anno Accademico 2017/2018

“Che la nobiltà dell’Uomo, acquisita in cento secoli di prove e di errori,
era consistita nel farsi signore della materia, e che io mi ero iscritto a Chimica
perché a questa nobiltà mi volevo mantenere fedele. Che vincere la materia
è comprenderla, e comprendere la materia è necessario
per comprendere l’universo e noi stessi.”

Primo Levi, “il sistema periodico”

Table of contents

Abbreviations

Ala	Alanine
Aβ	Amyloid β or β-Amyloid
AChE	Acetylcholinesterase
AD	Alzheimer’s Disease
APP	Amyloid Precursor Protein
Arg	Arginine
Asn	Asparagine
Asp	Aspartate
BBB	Blood Brain Barrier
BBS	Borate Buffer Solution
CAT	Catalase
CytC	Cytochrome C
DCM	Dichloromethane
DMSO	Dimethyl sulfoxide
Et_2O	Diethyl ether
ESI	Electrospray ionization
GHS	Glutathione peroxidase
Glu	Glutamic acid
His	Histidine
IC_{50}	Inhibitory concentration of 50% activity
Ile	Isoleucine
IR	Infrared spectroscopy
λ	Wavelength
MeOH	Methanol
Met	Methionine
MPAC	Metal Protein Attenuating Compounds
MS	Mass Spectrometry
NBT	Nitro Blue Tetrazolium

NFTs	Neurofibrillary tangles
NHE	Normal Hydrogen Electrode
NMDAr	N-methyl-d-aspartate receptor
NMR	Nuclear Magnetic Resonance
OPD	o-phenylenediamine
PBS	Phosphate Buffer solution
ROS	Reactive oxygen species
RT	Room Temperature
TEM	Transmission Electron Microscopy
ThT	Thioflavin T
Tyr	Tyrosine
UV-Vis	Ultraviolet-Visible

1. Introduction

1.1 Neurodegenerative disorders and Alzheimer

The word “neurodegeneration” etymologically is composed of the prefix “neuro-“, which designates the neurons, and “degeneration”, which refers, in the biological field, to a process of losing structure or functions. Therefore, neurodegeneration corresponds to any pathological condition primarily affecting neurons. In practice, neurodegenerative diseases represent a set of pathologies of the central nervous system, characterized by a chronic and progressive process of neuronal death. The neurons deterioration is the main cause of the generation of irreversible damage, with consequent alteration of brain functions that lead to cognitive and motor deficits, or behavioural disorders. They arise for unknown reasons and progress in a relentless manner[1]. Among these, the most common are Alzheimer's disease (AD), Parkinson's disease (PD) and Amyotrophic Lateral Sclerosis (ALS).

As regard AD or PD, the main risk factor for developing a neurodegenerative disorder is the increasing age. Over the past century, the growth rate of the population aged 65 has far exceeded that of the whole population. Therefore, the proportion of elderly citizens is destined to increase and, with this, the proportion of persons suffering of a neurodegenerative disorder[1].

Particularly, recent studies have estimated more than 35 million people living with dementia worldwide, the majority of whom are thought to have Alzheimer’s disease (50-75%)[2]. In 2040, the increase in the number of cases could reach 81.1 million of people[3]. A recent report by the *National Center for Health Statistics (NCHS)*, USA, points out that the number of deaths due to heart attack, stroke, AIDS or cancer has decreased significantly, while there is an increase in cases of death due to AD[4].

Therefore, it is clear that AD represents a major public health concern and it must be identified as one of the priorities in research. Even if there are already approved treatments to alleviate the symptoms, there is the need to better understand these pathologies in order to modify the progress of the disease and prevent neuronal death.

The AD was first described in 1907 by the German psychiatrist and neuropathologist Alois Alzheimer, who analysed, by autopsy, the brain tissue of a 55 years woman patient, died for dementia and revealed extracellular plaques and intraneural neurofibrillary tangles, currently considered the hallmarks of the disease[5]. The AD is characterized *pre-mortem* by a progressive loss of memory, speech and recognition of people and *post-mortem* by neuritic plaques containing amyloid β peptide and neurofibrillary tangles, where the phospho-tau protein is accumulated[6].

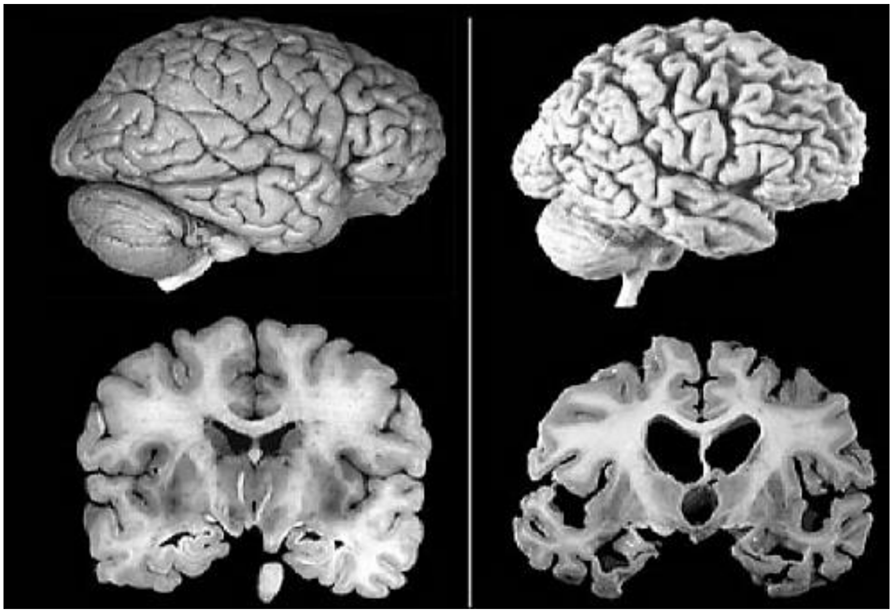

***Figure 1**: Image of a whole brain and in section, of a healthy person (left) and affected by AD (right).*

1.2 Causes of the Alzheimer development

The causes of the disease are not yet clear, but it is possible to identify different factors that increase the probability of disease onset. The early-onset AD is correlated to genetic factors, being genes mutations responsible for only 6%–8% of all Alzheimer disease cases[6]. An example is given by individuals with Down syndrome, a disorder characterized by the presence of three couples per cell of chromosome 21, which causes mental retardation and a characteristic physical appearance. These individuals develop AD by the age of forty. This occurs because the gene encoding APP (amyloid protein precursor), responsible for the production of the β-amyloid protein (Aβ), is located on chromosome 21. Therefore individuals affected by Down syndrome produce APP and consequently Aβ in an accelerate way[7]. Since, the percentage of presenile dementia due to genetic factors is very low, the environmental factors should have an important role in the development of disease pathology. Recent studies highlighted that lower educational and occupational attainment, female sex, low mental ability in early life and reduced physical activity during late life could increase the risk for the disease. As well as epidemiological factors like head trauma, heart disease, diabetes, smoking or obesity could influence the AD development[6]. However, the main cause of the disease is certainly age. In fact, the probability to develop the disease increases considerably exceeded the threshold of 65 years.

From a biological point of view, the AD is characterized by three distinct neuropathological abnormalities:

1) intracellular neurofibrillary tangles;
2) extracellular plaques;
3) high level of oxidative stress.

These factors are responsible of the damage to the biological target and the neuronal death.

1.2.1 Intracellular neurofibrillary tangles

Neurofibrillary tangles (NFTs) are intracellular aggregates of the hyperphosphorylated Tau protein. Tau is a microtubule-associated protein, that stabilized microtubules and is expressed in the axon.

To better understand the role of neurofibrillary tangles in AD, it is important to take into account the morphology of neuronal cells. The neuron is characterized by a central zone, called *pyrenophore*, which contains the nucleus and the organelles and a peripheral one, consisting of the cytoplasmic extensions, the *dendrites* and the *axon*. The latter ends with the synaptic buttons, which have the task of receiving and sending signals, through impulses, respectively towards and from the pyrenophore (*Figure 2*).

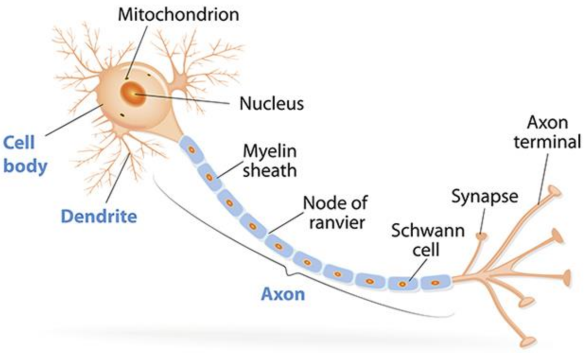

***Figure 2**: Neuron structure.*

The axon inner part is characterized by microtubules which, in normal healthy neurons, are stabilized by Tau protein. In AD, Tau is hyperphosphorylated and disassociated from microtubules, becoming insoluble and forming NFTs. Indeed, phosphorylated Tau is unable to bind microtubules and forms insoluble polymeric aggregates, which assemble in paired helical filaments (*Figure 3*)[8]. This process induces the cell death.

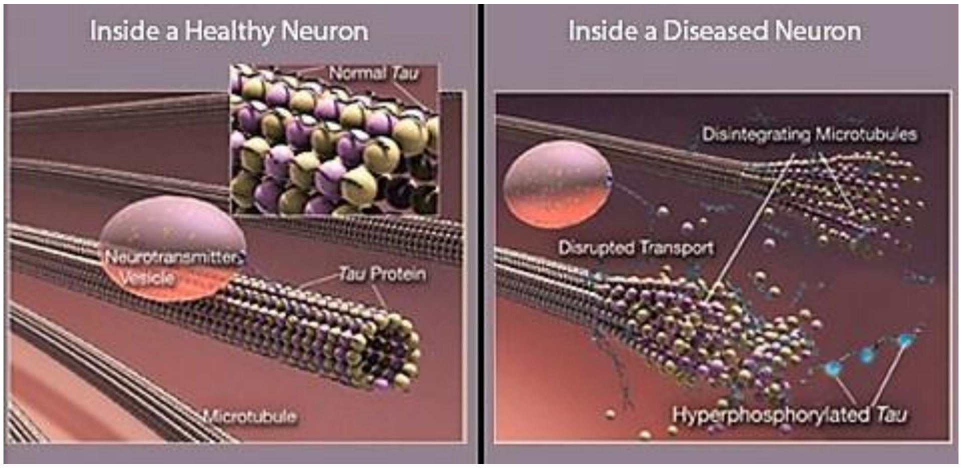

***Figure 3**: Illustration of Tau protein function, in the case of healthy person (left) and in the case of AD (right): while in the first case the protein holds the microtubules together, in the latter they break down leading to axon atrophy.*

1.2.2 Formation of extracellular plaques

Extracellular plaques are formed by fibrils of a protein constituted by 40-42 residues, named β-amyloid peptide (Aβ). It is a fragment of a membrane protein molecule, constituted by 695-770 residues and defined amyloid precursor protein (APP), which has various physiological functions. It comprises three parts, the extracellular N-terminal region, a single hydrophobic transmembrane region and a cytoplasmic C-terminal domain. In the amyloidogenic process, Aβ is released by APP during a step-by-step process, catalysed by two proteolytic enzymes, β- and γ-secretase[7]. In the case of non-amyloidogenic pathway, a third secretase, α-secretase, cleaves Aβ sequence, preventing its production[4] (*Figure 4*).

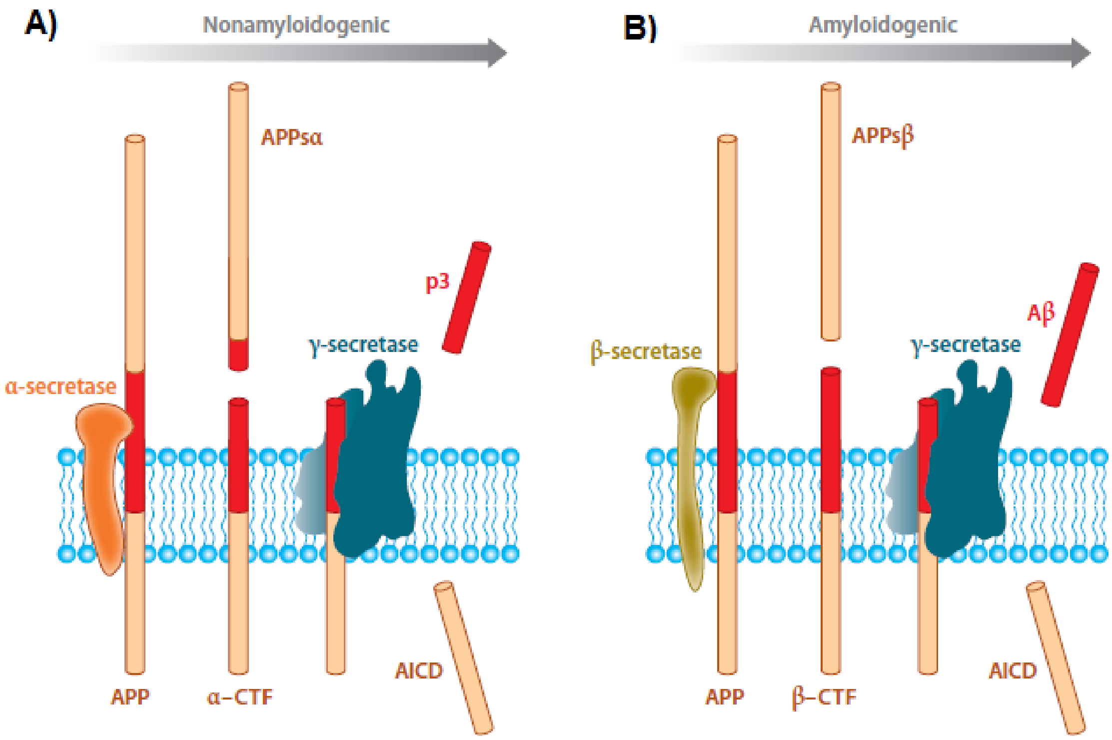

Figure 4: *A) Non-amyloidogenic process, involving α-secretase followed by γ-secretase is show; B) Amyloidogenic process, involving β- and γ-secretase.*

β-amyloid peptides have a pronounced tendency to aggregate in aqueous solution. In AD brain the major forms identified are Aβ (1-40) and Aβ (1-42). The first form is soluble in biological fluids (~90%), while Aβ (1-42) is less abundant in biological fluids but is the predominant species found in plaque deposits, due to its highest propensity for aggregation and fibrillogenesis[9].To explain the occurrence of amyloid deposits, two hypotheses were proposed: *amyloid cascade hypothesis* and *metal ion deposit*.

According to amyloid cascade hypothesis, the neurodegeneration begins with aggregation of monomeric Aβ. The misfolding of the APP protein and the following cleavage, induces a cascade of events leading to the formation of Aβ. The Aβ first aggregated into oligomer, through hydrophobic interactions and hydrogen bonds, then they form protofibrils, that finally generate insoluble plaques[10] (*Figure 6*). According to this hypothesis, the oligomers can act as nucleation centres in the brain for the formation of new oligomers, generating higher-ordered aggregates[4].

The formation of the fibrils involves a structural change of the Aβ, which passes from a random coil state to β-sheet. Spectroscopic analysis of amyloid-based fibrils indicates that these are arranged perpendicular to the axis of the fibril, in a parallel or antiparallel way, in a structure known as *"cross beta structure"*[7] *(Figure 5)*.

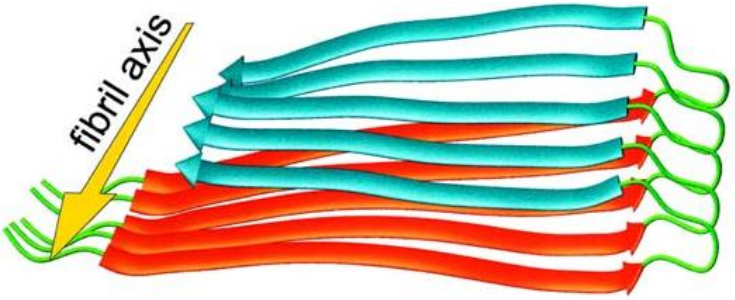

Figure 5: *Cross beta structure.*

The metal ions are important in many cellular processes. They allow the function of different metalloproteins (Cytochrome C-oxidase, Cu/Zn superoxide dismutase) and in the brain they take part in the neuronal activity within the synapses (Zn^{2+} and Cu^{2+} especially). Therefore, cells have developed a sophisticated machinery for controlling metal-ion homeostasis. A breakdown of these mechanisms could alter the ionic balance, causing several neurodegenerative disorders, like AD[9]. In fact, people who are affected of AD present higher concentration of metal ions than healthy individuals (metal ion deposit). Hence, in the aggregation process, also the role of the metal ion should be taken into account. Studies highlight that copper (II) can be bound by Aβ, enhancing the aggregations, the stabilization of the oligomeric state and the generation of reactive oxygen species (ROS)[4] (*Figure 6*).

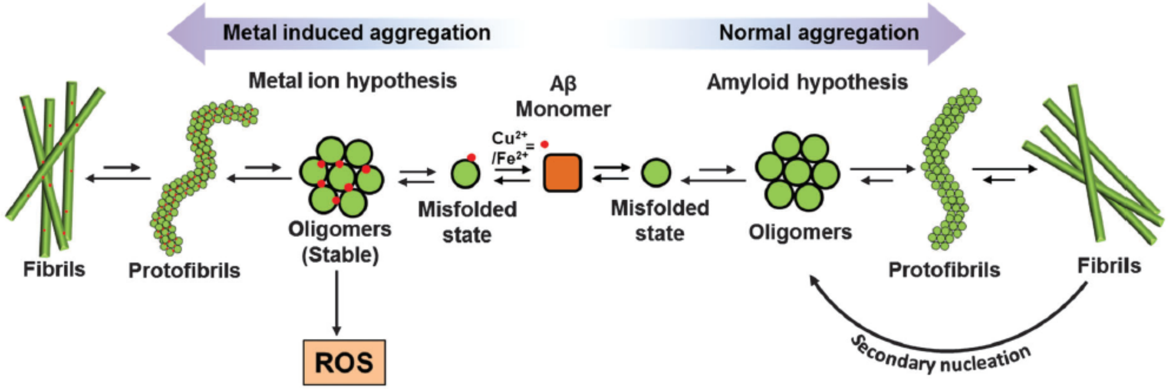

Figure 6: *Mechanism for the amyloid plaques formation: amyloid cascade hypothesis (right) and metal ion deposit (left)[4].*

In vitro experiments show that the precipitation of Aβ peptides is rapidly induced by Zn (II) and Cu (II) ions under physiological conditions (pH = 7.4). Besides, Cu(II) binding to soluble Aβ accelerates the aggregation, especially under mild acid conditions, similar to that found in AD brains[11]. Fe (III) ions exhibits a similar behaviour, too[10].

These metals, besides participating in the aggregation of Aβ peptides, can also facilitate the generation of reactive oxygen species (ROS) including hydrogen peroxide (H_2O_2), which may form hydroxyl radicals through the Fenton reaction. Hence, the Aβ toxicity is also attributable to the production of oxidizing species, responsible for cellular and tissue oxidative stress.

1.2.3 ROS and oxidative stress

One of the main causes of cellular damage and degenerative diseases is given by free radicals. A predominant cellular free radical is the superoxide anion: together with hydrogen peroxide and hydroxyl radicals, it is defined as Reactive Oxygen Species (ROS)[12]. ROS give rise to fast short-range and non-selective oxidation steps, being responsible for the "oxidative stress"[13]. The oxidative stress is a process, characterized by unbalance between the production and the elimination of oxidizing chemical species. Recent studies point out that the human brain produces more than 10^{11} free radicals per day, hence, the breakdown of the equilibrium in pro-oxidant vs antioxidant homeostasis result in oxidative stress, generating free radicals that could damage the biological target, like DNA, proteins and nucleic acids[14] (*Figure 7*).

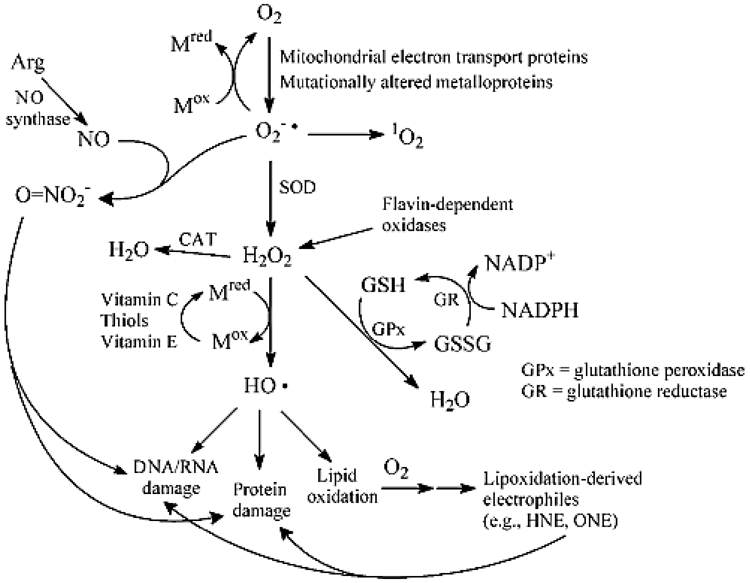

***Figure 7**: Process of production/elimination of ROS*

Superoxide anion is called primary ROS, since it is directly produced from mitochondria during the first reduction within the respiratory chain (1):

$$O_2 + e^- \rightarrow O_2^{\bullet-} \quad (1)$$

At a cellular level, the antioxidant activity is carried out by the combined action of specific enzymes: superoxide dismutase (SOD), catalase (CAT) and glutathione peroxidase (GHS). The SOD induce the superoxide anion dismutation to molecular oxygen and hydrogen peroxide, according to the reaction (2):

$$\begin{array}{c} O_2^{\bullet-} \rightarrow O_2 + e^- \\ O_2^{\bullet-} + 2H^+ + e^- \rightarrow H_2O_2 \\ \hline 2O_2^{\bullet-} + 2H^+ \xrightarrow{SOD} H_2O_2 + O_2 \quad (2) \end{array}$$

Subsequently, CAT and GHS use hydrogen peroxide as primary substrate to catalyse its conversion in water through the reaction 3, and activation through reaction 4:

$$H_2O_2 \rightarrow O_2 + 2H^+ + 2e^-$$

$$\underline{H_2O_2 + 2H^+ + 2e^- \rightarrow 2H_2O_2}$$

$$2H_2O_2 \xrightarrow{CAT} H_2O + O_2 \quad (3)$$

$$H_2O_2 \xrightarrow{2GHS} 2H_2O \quad (4)$$

These reactions point out that CAT enzymes during the dismutation of hydrogen peroxide produce oxygen and water, while the role of GSH is to deactivate oxidizing compound. During this process GHS is converted to its oxidizing form, GSSG, which subsequently is reduced to GHS, through GHS reductase, inducing the transformation of NAPH into NADP$^+$ (*Figure 8*).

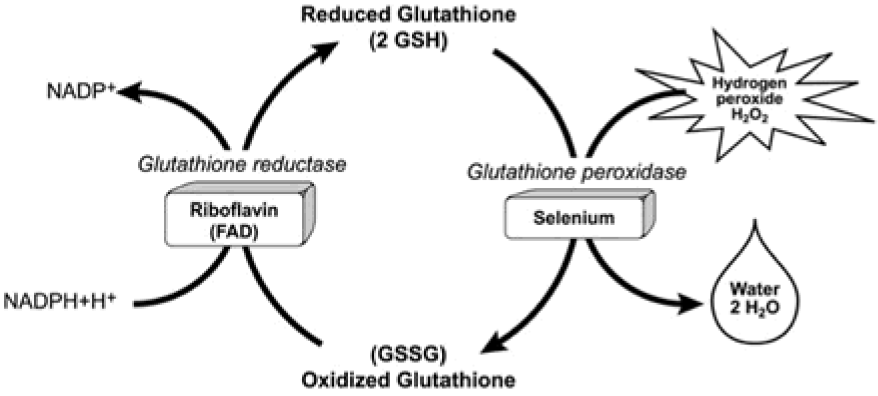

Figure 8: *Oxidation/reduction cycle of glutathione*

Other ROS are generated by Fenton reaction (reaction 6), that involves the metallic ions, previously reduced by superoxide radical anion, and H_2O_2, to produce hydroxyl radical OH•[14]:

$$Fe^{3+}/Cu^{2+} + O_2^{\bullet -} \rightarrow Fe^{2+}/Cu^{+} + O_2 \quad (5)$$

$$\underline{Fe^{2+}/Cu^{+} + H_2O_2 \rightarrow Fe^{3+}/Cu^{2+} + OH\bullet + OH^- \quad (6)}$$

$$O_2^{\bullet -} + H_2O_2 \rightarrow O_2 + OH\bullet + OH^- \quad (7)$$

The reaction 7 is the *Haber Weiss cycle* and promote the formation of hydroxyl radical from superoxide radical anion and hydrogen peroxide.

1.2.4 The correlation between oxidative stress and β-amyloid peptides

Transition metal ions, particularly Fe(III) and Cu (II) could form complexes with the β-amyloid peptides. Recent studies highlight that the copper ions, accumulated in amyloid plaques forms Cu–Aβ complexes, which catalyses the production of ROS (*Figure 9*).

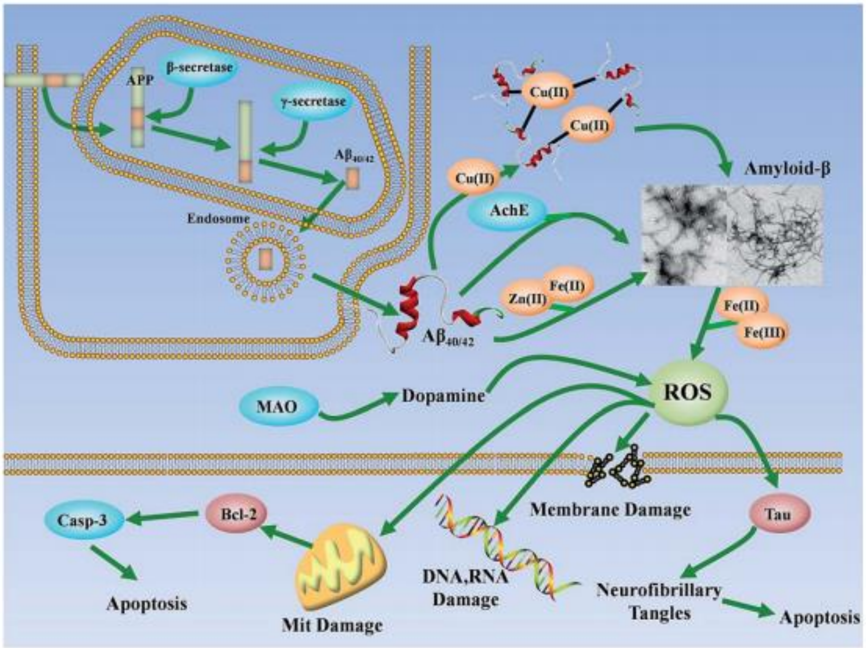

Figure 9: *The pathogenesis of AD showing the involvement of metal ions*

Aβ peptides have the ability to reduce Cu^{2+} to Cu^{+} and Fe^{3+} to Fe^{2+} (8) and these reduced metal ions can react with O_2 to produce superoxide anions (9) that easily generates hydrogen peroxide (10). The generated H_2O_2 species may react with another reduced metal species forming $OH^{\bullet}$ radicals via the Fenton (6) and Haber Weiss (7) reactions[10].

$$A\beta + Fe^{3+}/Cu^{2+} \rightarrow A\beta + Fe^{2+}/Cu^{+} \quad (8)$$

$$Fe^{2+}/Cu^{+} + O_2 \rightarrow Fe^{3+}/Cu^{2+} + O_2^{\bullet -} \quad (9)$$

$$2O_2^{\bullet -} + 2H^{+} \rightarrow H_2O_2 + O_2 \quad (10)$$

The reduction of metal ions is accompanied by oxidation of Aβ, in particular of the Met35 amino acid residue, located in the C-terminal portion of the Aβ peptide, within the transmembrane domain. The methionine residue is oxidized to the corresponding sulfoxide. The Aβ aggregates penetrate the membrane cell, through the transmembrane domain, assuming an α-helix structure, which has 3.6 residues per turn. This is the key to foster the oxidation of methionine residue, since Met35 is close to Ile31. The oxygen of Ile31 is more electronegative than sulphur and it pulls the electron density toward it, facilitating the one-electron oxidation of Met-35 to form sulfuranyl free radical MetS$^{\bullet+}$. Subsequently, the sulfaranyl radical causes the peroxidation of membrane lipids[15] (*Figure 10*).

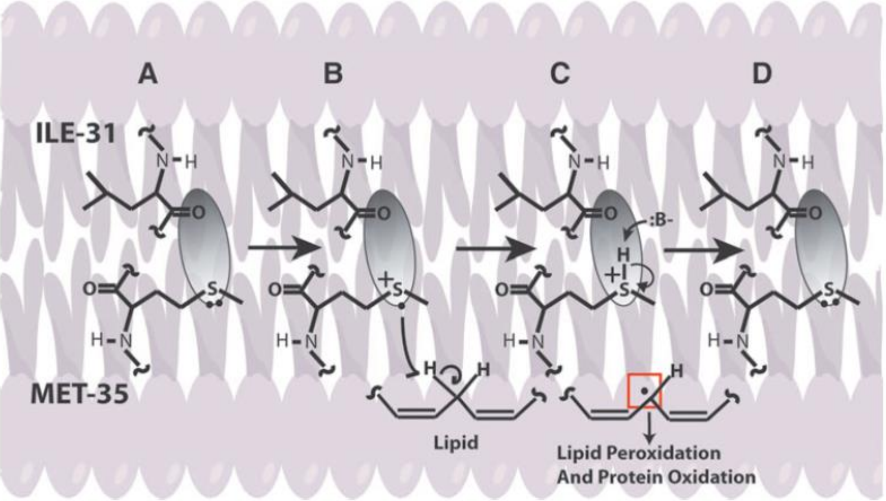

Figure 10: *Peroxidation mechanism of membrane lipids by amyloid peptides*

1.3 Therapeutic solutions and new perspective

In the last decades, the research focused on understanding the pathogenesis of AD failed in the development of drugs for the etiological treatment, i.e. drugs that act on the causes of the disease. Among the five approved drugs by the *"US Food and Drug Administration*", four are inhibitors of acetylcholinesterase (AChEIs) and only one is a non-cholinergic drug, the *N-methyl-d-aspartate* receptor (NMDAr) antagonist. In fact, another peculiarity observed in AD consists in the loss of the neurotransmitters functionality, such as acetylcholine due to the hydrolysis caused by the enzyme Acetylcholinesterase (AChE)[16]. Other approaces focus on different target of the disease and are based on the use of:

- metal chelators;
- modulators of the aggregation of Aβ peptides;
- antioxidants.

Nevertheless, the AD is a complex pathology and the therapies developed in the last 20 years can only alleviate the symptoms of disease, temporary slowing down the loss of memory and of cognitive functions, without modifying or blocking neuronal degeneration. Furthermore, they are efficient for a limited period of time and when the disease is still at an early stage. The lack of effective therapies lies in the numerous aspects that make AD so critical. This led the research in recent years to focus on the development of multi-target drugs, with features that can promote multiple approaches, simultaneously.

1.3.1 Metals chelators

The brain requires high metal ion concentrations to carry out its numerous essential function, within the synapses (Zn^{2+}) and for the metalloproteins functioning (Cu/Zn-SOD). However, the metal ion homeostasis is severely dysregulate in AD, indeed, people affected by this neurodegenerative disease presented abnormal levels of Cu(II), Zn(II) and Fe(III)[9].

The intracellular concentration of free copper, that does not cause oxidative damage is 10^{-18} M[14]. The extracellular copper concentration in normal brain is about 0.2-1.7μM, while in the amyloid plaques the copper concentration could reach 400μM. In contrasts, intracellular Cu level are lower in AD brain[9].

An interesting approach is the one based on the design of drugs, capable of sequestrating the excess of metal ion. These molecules compete with the peptides for the metal ions, reducing the neurotoxicity initiated by the Aβ-complexes and refurbishing metal ion homeostasis in the brain. These drugs are known as MPAC, *Metal Protein Attenuating Compounds* and must have particular features: a moderate chelating ability, to compete with the formation of the metal complex with Aβ, without disturbing the metal homeostasis. Moreover they must be characterized by a low toxicity and low molecular weights (<500 Da). Finally, they must be sufficiently hydrophilic to be soluble and stable in a physiological environment and simultaneously have sufficient hydrophobicity to cross the Blood Brain Barrier (BBB), an anatomical brain component with the function of selecting the passage of only agents useful for metabolic functions [4,10,17].

The clioquinol (CQ, 5-chloro-7-iodo-8-hydroxyquinoline) is the prototypic MPAC, since its small hydrophobicity, moderate affinity for metal ions and its capacity to cross the Blood Brain Barrier (BBB)[17]. In addition, it also has the ability to chelate copper (II) and zinc (II) with the ratio of 2 : 1, CQ : metal[10] (*Figure 11*), whose binding constants are log K_1 (Cu) = 12.5, log K_2 (Cu) = 10.9, log K_1 (Zn) = 8.5 and log K_2 (Zn)= 7.6[9]. However, due to the possible neurotoxicity and mutagenic impurities the development of CQ as anti-Alzheimer's drug was suspended.

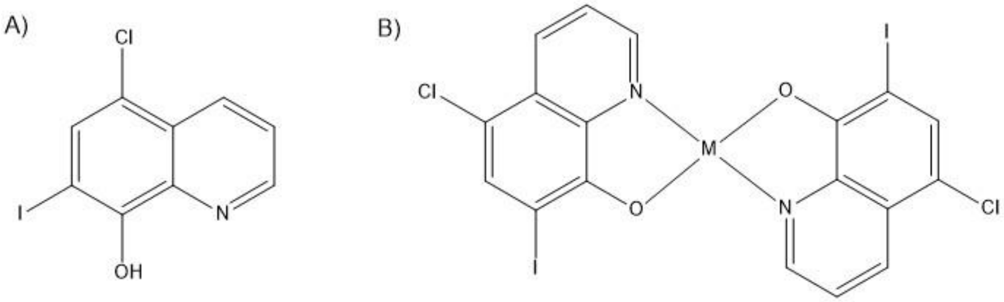

***Figure 11**: A) CQ and B) complex CQ : metal 2:1 structures.*

Prana Biotechnology, in collaboration with Barnham and coworkers, synthesized a second generation MPAC PBT2, that has higher solubility and increased BBB permeability as compared with CQ[9].

PBT2 is a 8-OH quinoline derivative of CQ without iodine atom (*Figure 12*), that has been demonstrated to be able to prevent the production of Aβ oligomers and to dissolve the existing Aβ oligomers. In people with mild Alzheimer's dementia, PTB2 appears to be safe and well tolerated. Unfortunately, recent studies showed that there is no significant decrease of the Aβ levels in mild AD patients.

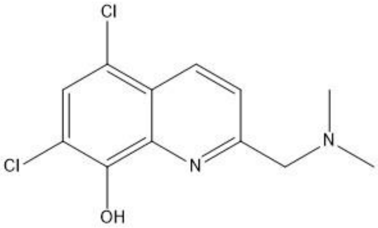

***Figure 12**: Structure of PB2*

To increase the chances of success, currently, the chelators are also designed to integrate the chelating function with other features, in order to block also other molecular events involved in the disease. For example, Deferiprone(DFP, 3-hydroxy-1,2-dimethylpyridin-4(1H)-one) is a chelator used for the treatment of thalassaemia. Its shows strong affinity for iron, copper and zinc. Although its scaffold presents too low hydrophobicity to cross BBB, its low molecular weight (MW = 139) and suitable structure make DFP amenable to an optimization . Another example is given by the curcumin, whose enolic form possess a good chelating ability to bind copper (II). Cu(II)–curcumin complex can also scavenge free-radical. Moreover, studying led on transgenic mouse demonstrated few side effect end toxicity issues (*Figure 13)*[10].

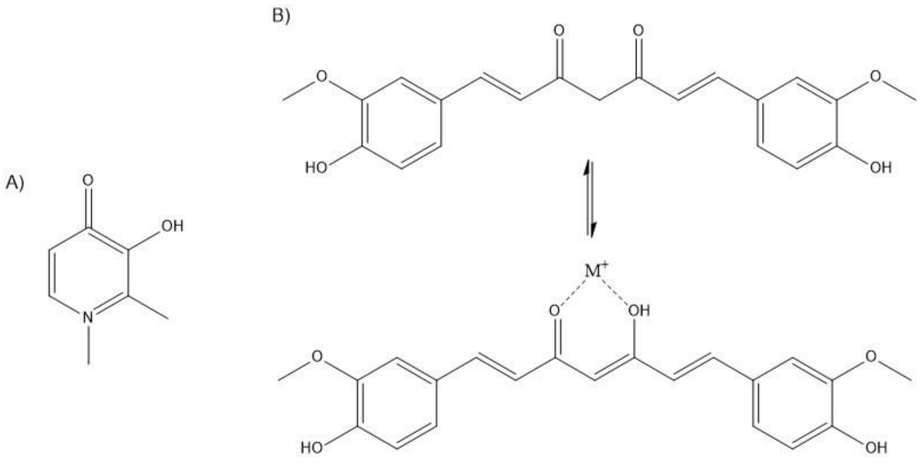

Figure 13*: A) structure of DFP and B) Cheto-enolic equilibrium of curcumin*

1.3.2 Modulator for Aβ peptides aggregation

Neurodegenerative disorders are characterized, in part, by the misfolding and subsequent aggregation of different peptides and proteins into various structures[18]. In particular, in the AD the APP cleavage causes the formation of amyloid fibrils, one of the main factor of the neurons death. Hence, targeting Aβ aggregation is considered an effective therapeutic strategy[4]. The strategies that allow the inhibition of protein aggregation and amyloid fibril formation involve:

- blocking the peptide switches from a nontoxic α-helical state to a toxic β-sheet conformation;

- limitation of the amyloid monomer proliferation, through the inhibition of secretase enzymes;
- redirection of the amyloid fibril formation into non cytotoxic pathway. In fact, the fibril toxicity is correlated to the formation of transmembrane ion channels, due to the permeation of the amyloid oligomers in the cell membrane; the interaction between the latter and the oligomers activates a sequence of negative events for the cell[19,18].

In the recent years, modulators of Aβ aggregation are developed, depending upon their chemical structure they are defined as peptide-based modulators and small molecule-based modulators. Peptide-based inhibitors are based on sequence from 5 to 15 of natural or unnatural amino acids. The key point in the design of the molecules is related to the hydrophobic core (KLVFF) of Aβ peptides. The KLVFF sequence plays a central role in the initiation of Aβ aggregation and in the fibrils elongation. Hence, the challenge is to find hydrophobic peptides that competes with the hydrophobic core of the Aβ peptide. KLVFF and LPFFD have been reported to be effective in the inhibition of Ab fibrillogenesis both in vitro and in vivo[20,21]. Even if peptide-based drugs are very specific and effective, their poor bioavailability limit their use as potential therapeutic agents.

The modulation of Aβ aggregation using small molecules can also exploit hydrophobic interactions. Natural phenol, like curcumin, resveratrol, and epigallocatechin-3-gallate (EGCG) have been shown to be effective in decreasing the development of Aβ plaques in the brain, through their antioxidant and aggregation inhibition properties[22] (*Figure 14*). HEWL study (Hen egg white lysozyme) a protein known to stack in an analogue way, demonstrated that the presence of almost three OH groups on various phenolic group are essential for efficient inhibition of the aggregation by polyphenols[18].

Since these drugs have a limited efficacy, the attention is moving towards others solutions. Indeed, the institutions such as the *Alzheimer's Drug Discovery Foundation* and the *European Research Council* are discouraging the search in the field of anti-amyloidogenic drugs.

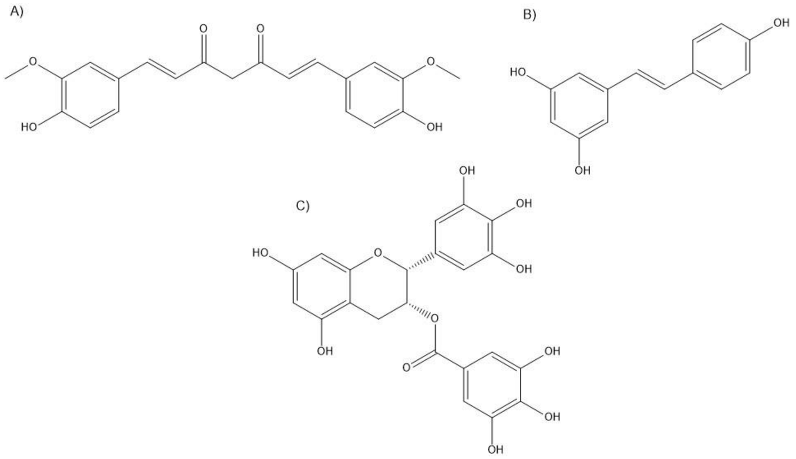

***Figure 14**: Structure of A) Curcumin, B) resveratrol and C)ECGC*

1.3.3 Molecules with antioxidant biomimetic activity

As described previously, one of the main cause of AD is ROS overproduction. At the cellular level, the ROS detoxification occurs via the combined action of antioxidant enzymes: superoxide dismutase (SOD), catalase (CAT) and glutathione peroxidase (GHS). Therefore, recent studies are focused on the design of molecule able to mimic the activity of these natural enzymes. In order to keep the level of superoxide radicals under control, mammals possess two classes of SODs. Mn-SODs are located in the mitochondrial matrix, as tetramers, and in the cytoplasm of bacteria, as dimers. The active centre is characterized by a distorted trigonal bipyramidal geometry, where the single Mn is coordinated by two histidines and one aspartic acid residue in the equatorial plane, while one histidine and one solvent molecule occupy the axial position. Cu/Zn-SOD is present in the cytosol and contains a dinuclear core of copper and zinc (*Figure 15*).

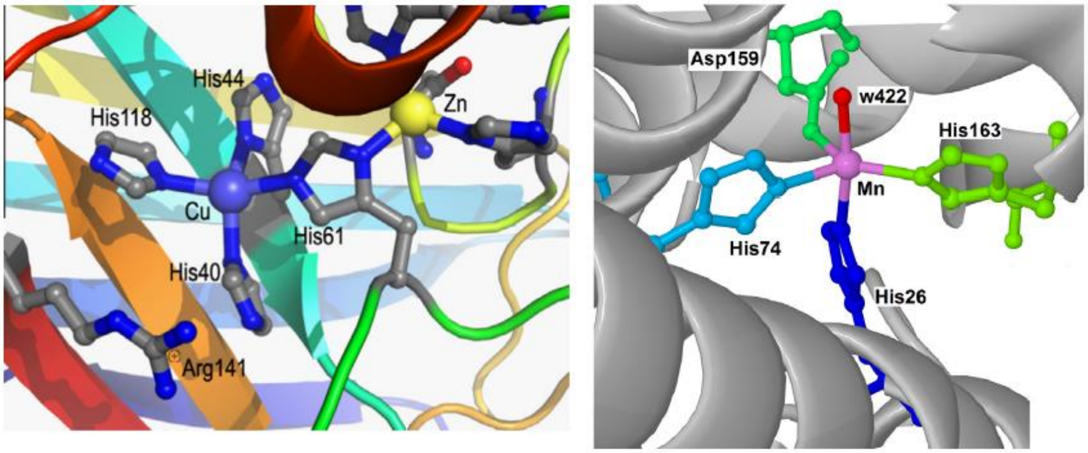

Figure 15: *Active sites of Cu/Zn-SOD (left) and Mn-SOD (right)*

The copper (II) is a distorted square pyramidal geometry. The coordination in the reduced state differs from the one in the oxidized state. In the first case, Cu(II) is coordinated by three histidine nitrogen atoms (His44, His118, His46), while in the oxidized state there is a water molecule and the His61, which is a bridge between the two metal centres[23]. Zn (II) is in a distorted tetrahedral geometry, bound to the nitrogen atoms of His78, His65, His61 and by the oxygen of the Asp81 residue (*Figure 16*).

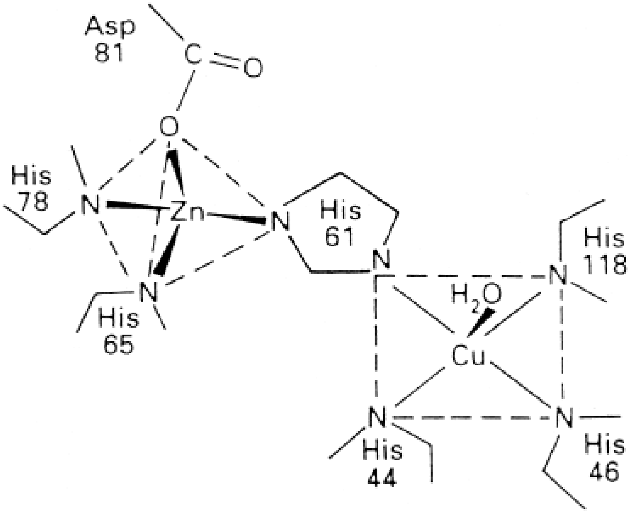

Figure 16*: Coordination geometry of Cu(II) and Zn (II) in Cu/Zn-SOD*

The superoxide radical anion binds selectively to the sterically hindered active site[24], through a funnelling effect, that electrostatically guides the radical anion through a channel formed by positively charged amino acid residues[25].

During the SOD turnover, the redox active copper centre cycles between Cu(II) and Cu (I) oxidation states upon interaction with $O_2^{\bullet-}$ (reaction 11 and 12), while Zinc appears to play a role in the overall enzyme stability and in facilitating a broader pH independence, in the rage 7-7.8[26,27,28].

$$O_2^{\bullet-} + Cu^{II}Zn^{II-}SOD \rightarrow O_2 + Cu^{I}Zn^{II-}SOD \ (11)$$

$$O_2^{\bullet-} + 2H^+ + Cu^{I}Zn^{II-}SOD \rightarrow H_2O_2 + Cu^{II}Zn^{II-}SOD \ (12)$$

Through an inner sphere electron transfer mechanism, there is simultaneously the oxidation of the superoxide radical anion and the reduction of the metal centre, with the release of molecular oxygen. At the structural level, the concomitant breaking of the copper–imidazolate bond is fostered by protonation of the imidazolate, which is assisted by the solvent. After, a second $O_2^{\bullet-}$ is reduced and associated with two protons, producing hydrogen peroxide and re-oxidizing copper. In this second step, the His induces the exit of hydrogen peroxide, protonating the superoxide radical anion coordinated on Cu (I), which is oxidized again to Cu (II)[25] (*Figure 17*).

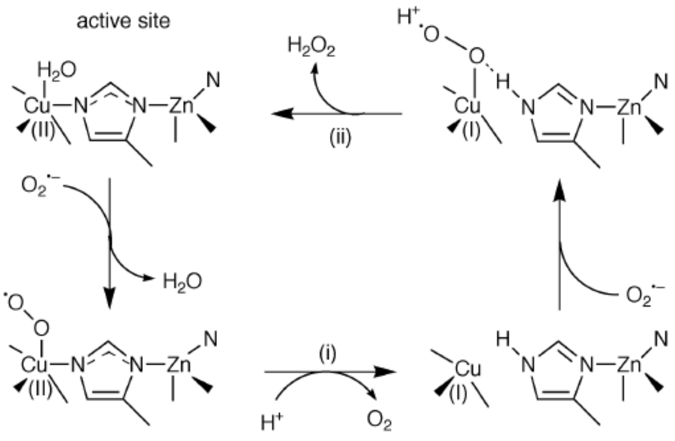

Figure 17: *Mechanism of $O_2^{\bullet-}$ dismutation, catalysed by Cu/Zn-SOD*[25]

The two steps occur with a rate constant of $k_{cat} \approx 2 \cdot 10^9\ M^{-1}s^{-1}$, the rate is close to the diffusion control and show independence from the pH in the range between 5 and 9.5[7].

SOD enzymes are not enough to detoxify the cell. First, the dismutation of superoxide radical anion, mediated by the SOD, yields H_2O_2, which is a strongly oxidizing species, able to diffuse within the cell compartments, causing several damages. Moreover, in the condition of oxidative stress, the Cu/Zn-SOD could react with H_2O_2, generating radical species, according to the Fenton-like reaction:

$$H_2O_2 + Cu^{II}Zn^{II-}SOD \rightarrow H^+ + HO_2\bullet + Cu^{I}Zn^{II-}SOD \ (13)$$

$$H_2O_2 + Cu^{I}Zn^{II-}SOD \rightarrow OH\bullet + OH^- + Cu^{II}Zn^{II-}SOD \ (14)$$

Studies have demonstrated that the hydroxyl radical generate in the active site can break the bond between the copper and the histidine, causing copper loss with deactivation of the enzyme[24].

As regard the hydrogen peroxide, its concentration is regulated by two enzymes: the catalase (CAT) and glutathione peroxidase (GSH). The latter induces the activation of H_2O_2, oxidizing the NAPH or others substrates. While CAT role is to convert H_2O_2 in water and molecular oxygen with high efficiency.

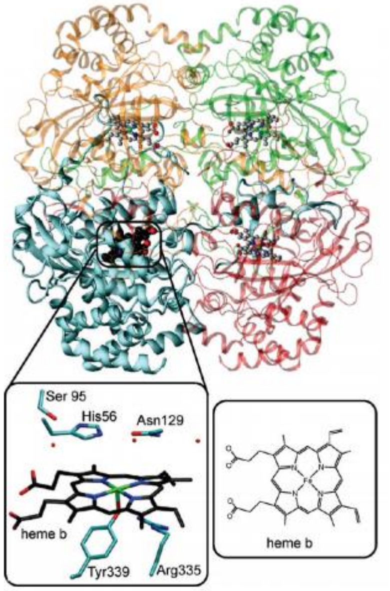

Figure 18: *Structure of Fe-CAT and Fe coordination in the active site*[29].

Two families of natural catalase are known. The most common catalase is the one based on iron-heme cofactor. These catalases are characterized by tetramers of identical subunits containing a ferriprotoporphyrin as prosthetic group. Above the protoporphyrin plane, the Fe (II) is bound to different His and to one Asn, while below there are Tyr and Arg residues[29] (*Figure 18*).

The dismutation of hydrogen peroxide, through Fe-CAT precedes with a two steps mechanism. First, the oxidation of prosthetic group causes the concomitant oxidation of Fe(III) to Fe(IV), generating a radical cation on the porphyrin (15). After, a second H_2O_2 reacts with radical cation, regenerating the enzyme and producing water and molecular oxygen (16).

$$Fe^{III}Por + H_2O_2 \rightarrow (Fe^{IV} = O)Por^{+\bullet} + H_2O \quad (15)$$

$$(Fe^{IV} = O)Por^{+\bullet} + H_2O_2 \rightarrow Fe^{III}Por + H_2O + O_2 \quad (16)$$

The second class of catalase enzyme are the MnCAT. The active site of binuclear manganese enzyme contains two Mn ions, triply bridged, by $\mu_{1,3}$-carboxylate from a Glu residue (Glu66) and by two water molecule (W1 and W2). Glu35 is coordinated to Mn1 and simultaneously establishes a hydrogen bond with the W2 water molecule. While Glu148 acts as bidentate ligand, coordinating the Mn2 with the two carboxylate oxygens. The last coordination site for Mn1 and Mn2 is occupied by His69 and His181, respectively. The arrangement of the ligands produces octahedral coordination at both metal centres[30] (*Figure 19*).

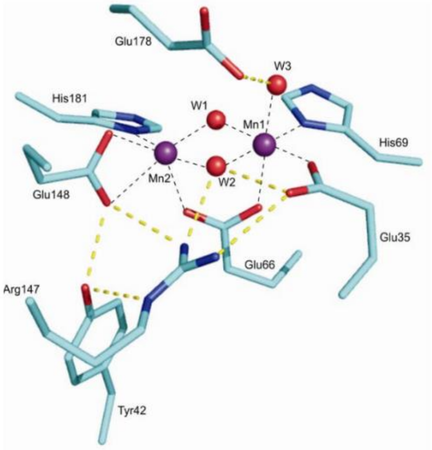

***Figure 19**: Binding site of L. Plantarum MnCAT[30].*

As regard the mechanism, during the catalytic cycle, each two metal centres perform a one-electron redox cycle, through two half reactions:

$$H_2O_2 + \{Mn_2\ (III,III)\} \rightarrow O_2 + \{Mn_2\ (II,II) + 2H^+\} \quad (17)$$

$$H_2O_2 + \{Mn_2\ (II,II) + 2H^+\} \rightarrow H_2O + \{Mn_2\ (III,III)\} \quad (18)$$

In the oxidative half-reaction (17) hydrogen peroxide is oxidized to dioxygen, and the manganese cluster is reduced. While, in the reductive half-reaction (18) the reduced metallocluster delivers the electrons and protons to a second molecule of H_2O_2 to form two water molecules[31].

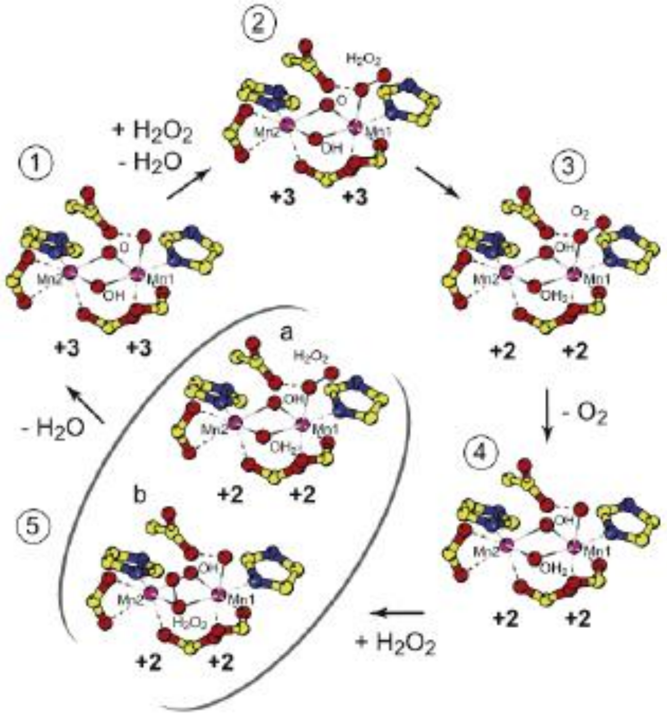

***Figure 20**: Hydrogen peroxide dismutation mechanism[31].*

In the molecular mechanism, based on structural data, the neutral hydrogen peroxide substrate reaches the active site and coordinates to Mn1, displacing the water molecule in the apical position (*Figure 20*,2). At this point an electron transfer from hydrogen peroxide to the mental centres occurs, while the Glu178 plays a role in facilitating movement of protons from the bound substrate to the bridging solvents. This proton-coupled electron transfer generate the dioxygen product of the reaction 17 and reduces Mn(III) to Mn(II) (*Figure 20*,3). The dioxygen molecule exits from the active site and a solvent molecule replaces dioxygen in the axial position of Mn1 (*Figure 20*,4). Subsequently, a second molecule of hydrogen peroxide enters the active site and bind terminally to Mn1 (*Figure 20*,5a), or inserts into the cluster core to form a bridging peroxo complex (*Figure 20*,5b). During the cleavage of the O–O bond, two protons and two electrons are donated to the solvent and to the metal centre, respectively. This allows the production of two water molecules and the oxidation of two Mn(II) to Mn(III) (*Figure 20*,1)[31].

The heme-containing catalases are characterized by constant rate near to the diffusion-controlled turnover($k_{cat}=4\cdot10^7 s^{-1}$), on the other hand non-heme manganese catalases exhibit much slower kinetics (for *L. Plantarum Catalase* $k_{cat} = 2\cdot10^5\ s^{-1}$)[31].

Despite these interesting features, natural CATs and SODs cannot be applied as pharmaceutical agents. In fact, they present some limitations due to the low stability in solution, short half-life and elevated cost of production[32]. To help the body fight off oxidative stress, antioxidant-rich diet, based on vitamins and polyphenols is still the preferred recommendation. Nevertheless, these nutritional antioxidants are non be able to react faster with the ROS than the vital biomolecules, so that a high excess is required.

To overcome these limitations, the scientific research, in the past 30 years has been focused on the design of small molecules able to act as catalytic antioxidant, in order to mimic both SOD and CAT natural enzymes. The first attempts, focused on the elimination of $O_2^{\bullet -}$ was introduced in 1979 by Pasternack et al., who used metalloporphyrins as SOD mimic[33].

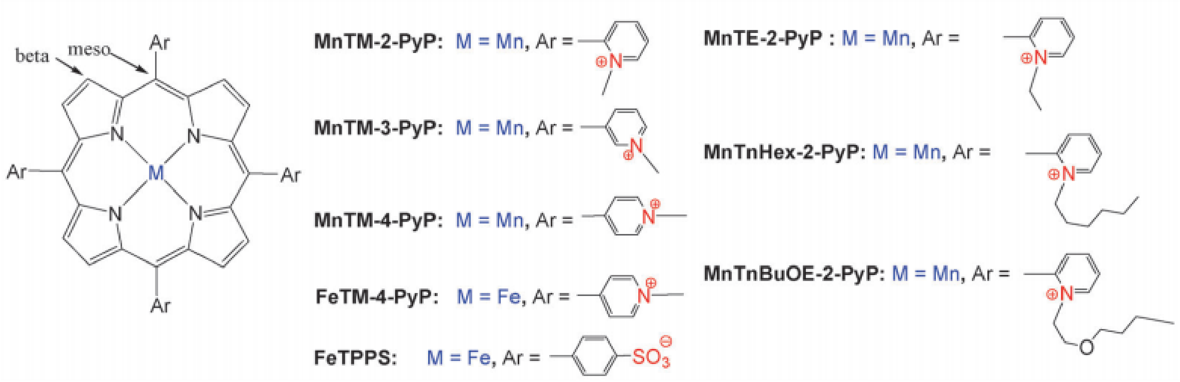

Figure 21*: First porphyrin studied, with biomimetic activity.*

Successive researches were focused on the synthesis of porphyrin, differently substituted with Mn (III) and Fe(III) (*Figure 21*). Among these, the best Mn porphyrin was *MnTnBuOE-2-PyP* with $k_{cat} = 6.8\cdot10^7\ M^{-1}s^{-1}$, while for Fe, *FeTM-4-PyP* with k_{cat}

= 3·10^7 $M^{-1}s^{-1}$, compared with the value of natural SOD, k_{cat}=2.3·10^9 $M^{-1}s^{-1}$. Even if the Fe porphyrins display a better SOD-like activity, they are cytotoxic, due to the tendency to lose metal ion at low pH, inducing Fenton chemistry [32].

Recent efforts have been dedicated on the discovery of structures that combine the synergistic SOD-CAT activity. While enzymes cannot show both anti-oxidant activity, due to their specific proprieties, these can be achieved with synthetic catalyst[47]. Mn complexes with multidentate ligands, as Salen, Shiff's bases are the most studied in the recent years. However, these complexes are soluble in organic solvent, hence the main problem is correlated to the low solubility and stability in aqueous media. Bonchio and coworkers[26] developed new dinuclear Mn(II) complexes, with both SOD/CAT activity in physiological condition. The structure is based on a single site Mn(III)-heme, implemented with a di-nuclear, non-heme, Mn_2(II)L_2 catalytic unit (*Figure 22*). The main feature is correlated to "built-in-self-protection" against the oxidative risk. The SOD activity, expressed as IC_{50} values, the initial rate, R_0 and the ratio k_{cat}/K_M are reported in *Table 1* and highlight the positive effect in the antioxidant activity, expressed by the two units.

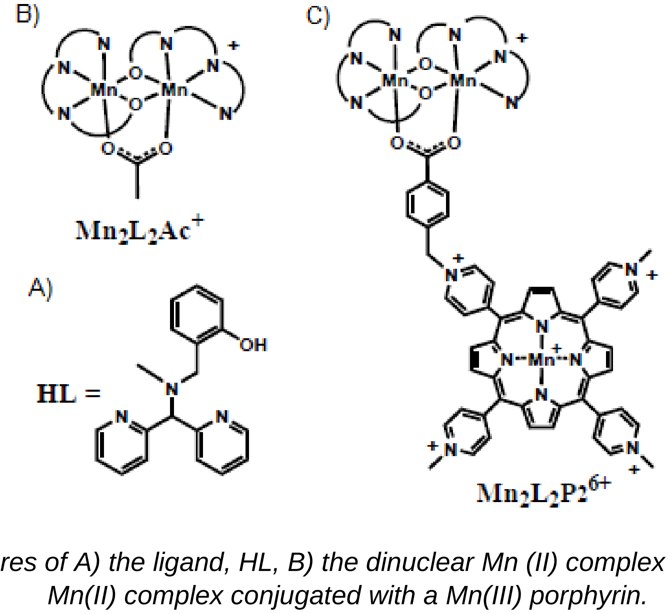

Figure 22*: Structures of A) the ligand, HL, B) the dinuclear Mn (II) complex and C) the dinuclear Mn(II) complex conjugated with a Mn(III) porphyrin.*

Table 1: *SOD/ CAT values obtained for $Mn_2L_2Ac^+$ and $Mn_2L_2P_2^{6+}$: a) SOD activity based on the cyt c assay; IC_{50} indicates the catalyst concentration required to attain 50% inhibition of the cyt-c reduction; Conditions: [xanthine] = 40 µM, [xanthine oxidase]=0.0053 U/ml, [CytC]=10 µM, [catalase]= 15 µg/ml, in 50 mM phosphate buffer, pH=7.8. b) R_0 is obtained by linear regression of data within 10 % H_2O_2 conversion. Conditions: [catalyst]= 50 µM, [H_2O_2]=10 mM, 25 °C; Michaelis Menten parameters $k_{cat}(H_2O_2)/K_M$ were determined with conditions: [catalyst]= 10 µM, [H_2O_2]= 0.1-10 mM in BBS 50 mM pH=7.8 at 25 °C.*

Complexes	IC_{50}(µM)^a	R_0(µmol/min)^b	$k_{cat}/K_M(M^{-1}s^{-1})$
$Mn_2L_2Ac^+$	1.04	1620	1245
$Mn_2L_2P_2^{6+}$	2.34	2160	1890

Besides manganese, also copper(II) has an important biological. Due to the redox behaviour of the Cu(II)/Cu(I) system and the interaction of copper complexes with molecular oxygen, biomimetic complexes with interesting ligand have been investigated*. Riberio et al* studied mononuclear copper (II) complex, stabilized by N_3O ligand donor set, with antioxidant biomimetic activity (*Figure 23*). They found out a low value for IC_{50} (0.43 µM), indicative of a high SOD-like activity[34].

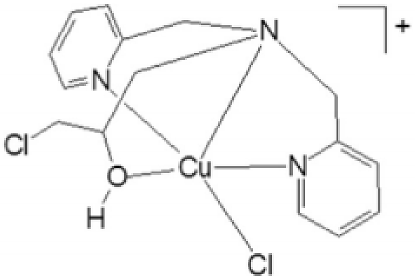

Figure 23: *Mononuclear copper(II) complex studied by Riberio et al.*

Others mononuclear copper(II) complexes with relevant SOD and CAT-like activity are the ones studied by *Pap et al*[35]. In these complexes, the copper (II) centre is stabilized by N_3 or N_3O -donor set ligand (N-methylpropanoate-N,N-bis-(2-pyridylmethyl)amine= MPBMPA, and N-propanoate-N,N-bis-(2-pyridylmethyl)amine = HPBMPA) (*Figure 24*). The atoms around the copper(II) are in a square-planar pyramidal arrangement, where, in the case of HPBMPA, the apical position is occupied by the counter ion Cl, while in the complex with MPBMPA, the oxygen of the carboxylate group occupies such position. The SOD and CAT values are reported in *Table 2*.

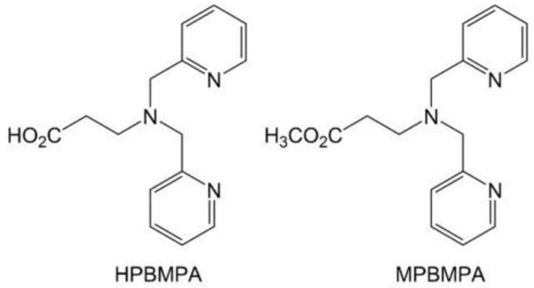

***Figure 24**: Ligands structure of HBMPA and MPBMPA.*

***Table 2:** SOD/CAT values obtained for the complexes studied by Pap et al. The IC50 value is obtained with CytC assay at pH 7.6, while the CAT experiments were carried out at pH 11.*

Catalysts	IC_{50} (μM)	$R_0(10^{-4}M/s)$
Cu(PBMPA)Cl	1.04	0.35
$Cu(MPBMPA)Cl_2$	0.62	0.36

Another example, studied in the laboratory where the thesis internship was held, is characterized by dinuclear copper(II) complexes, stabilized by N_3O-donor set ligands. The complexes present an optimal combined superoxide dismutase and catalase-like activity, in physiological-like conditions. As regard the structures, the complexes are characterized by a distorted octahedral geometry, where each Cu(II) atom is coordinated in a facial configuration by the three N atoms of the tetradentate ligand, while the phenolate ligands acts as a bridge between the two metal centres[26] (*Figure 25*). All the three complexes work as artificial SODs in phosphate buffer, at pH= 7.8, following a trend that depends on their structure $Cu_2L^1_2 < Cu_2L^2_2 < Cu_2L^3_2$. The same trend is observed also for the CAT-like activity, where the experiments were carried out in a borate buffer at pH 7.8. The values relative to the SOD and CAT activity are reported in *Table 3*.

***Table 3**: SOD/ CAT values obtained for $Cu_2L^1_2$, $Cu_2L^2_2$, $Cu_2L^3_2$. a) SOD activity based on the Cyt c assay where radical anions are generated by the xanthine/xanthine oxidase system. Conditions: [xanthine] = 40 μM, [xanthine oxidase]=0.0053 U/ml, [CytC]=10 μM, [catalase]= 15 μg/ml, in 50 mM phosphate buffer, pH=7.8; IC_{50} indicates the catalyst concentration required to attain 50% inhibition of the cyt-c reduction; log $k_{cat}(O_2^{\bullet-})$ refers to the rate constant of catalytic superoxide dismutation. b) CAT activity is based on oxygen evolution kinetics, monitored by a pressure transducer. R_0 where obtained by linear regression of data within 10 % H_2O_2 conversion; Measured in 50 mM BBS, pH 7.8 at 25 °C.*

Catalysts	**SOD Activity^a**		**CAT Activity^b**	
	IC_{50} (μM)	**log k_{cat} ($O_2^{\bullet-}$)**	**R_0 (μmol O_2/s)**	**TON**
$Cu_2L^1_2$	0.40	6.80	0.87	52
$Cu_2L^2_2$	0.14	7.27	4.4	60
$Cu_2L^3_2$	0.072	7.55	4.3	60

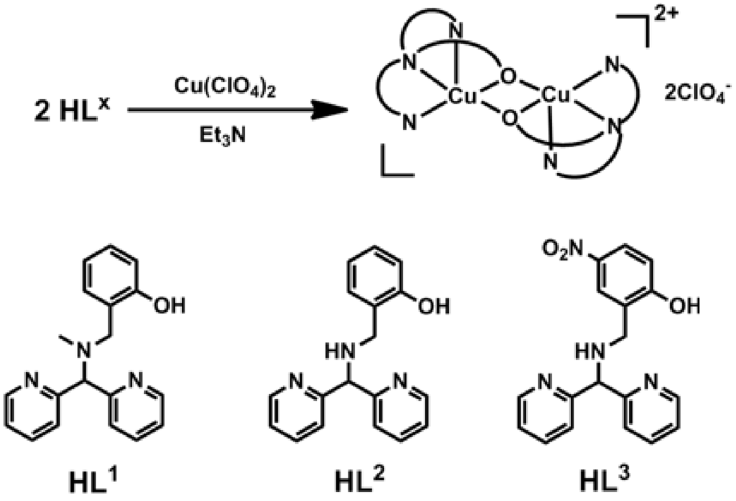

***Figure 25:** Synthesis and structure of dinuclear complexes studied by Squarcina et al.[26]*

1.3.4 Multivalent approach

As already introduced above, in the development of neurodegenerative disorders, different factors must be taken into account. The existing approaches focus only on one target that determines the neurodegenerative disorders. Hence, the attention is moving to multivalent drugs, able to inhibit more than one causes of the AD.

Multifunctional metal chelators have been tested for both chelating and antiaggregation ability. These agents can show good uptake across the BBB, high selectivity for metal, antioxidant capabilities and inhibition of Aβ peptide aggregation.

One example is given by the molecules studied by Xingshu Li and coworkers, obtained from a combination of resveratrol with the CQ (*Figure 26*)[36].

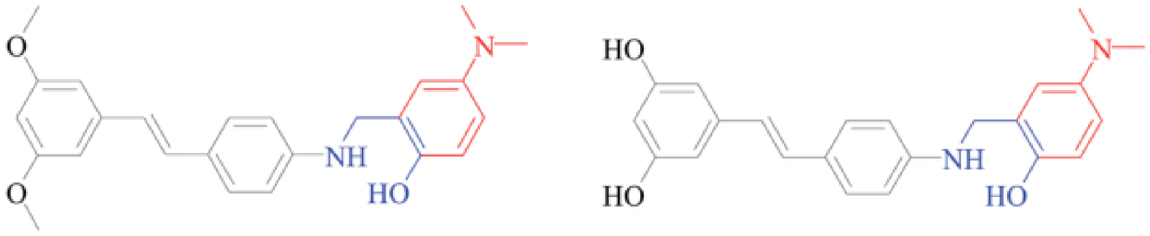

***Figure 26**: Chemical structures of molecules having bifunctionality: the metal chelation (blue) and Aβ interaction (red)[10].*

Others studies are dedicated to the synthesis of molecules that combine the chelating and antioxidant activity. BHAPI is an oxidant-triggered prochelator, which transforms into a chelator (HAPI) upon reaction with hydrogen peroxide (*Figure 27*).

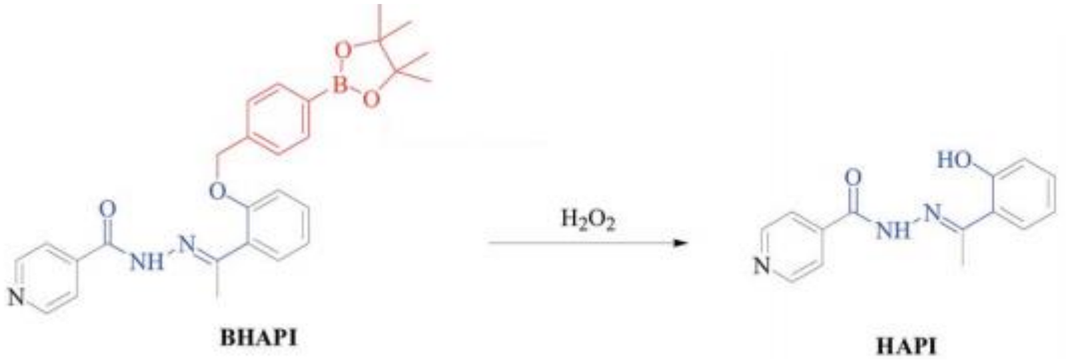

***Figure 27:** Chemical structure of BHAPI and HAPI. The blue colour represents the metal binding site, while the red one the antioxidant site[10].*

In other works, the attention was pointed on substrates obtained from modified Thioflavin-T, a dye used as a marker to detect amyloid deposits in tissues, due to its strong affinity for amyloid fibrils. *Dedeoglu et al.* designed and synthesized bifunctional molecule with both amyloid-binding and metal-chelating moieties[37] (*Figure 28*).

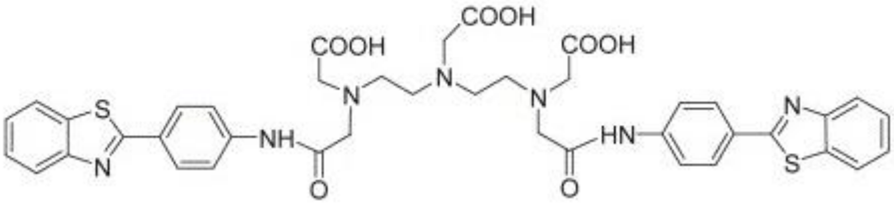

***Figure 28**: Structure of Thioflavin-T derivative synthetized by Dedeoglu et al[37].*

The multitarget approach is complex, but it allows to attack simultaneously the different causes of AD. Even if many multifunctional agents have been proposed, many other factors need to be studied to obtain a good multitargeting drug.

1.4 Aim of the thesis

This work is focused on the synthesis and study of mononuclear and dinuclear copper complexes able to inhibit the oxidative stress, mimicking the activity of natural enzymes, as well as the formation of Aβ aggregates. The selected N_3O-type ligands were initially screened for their capability to form copper complexes in aqueous mixtures, by evaluating the stoichiometry and biding constants, so to assess their potential as copper chelators. The respective complexes were characterized to get information about the structural, spectral and electrochemical features. The complexes formed *in situ* were investigated by potentiometry, in order to understand how which species are predominant at physiological pH. Then, their ability as SOD and CAT-like was investigated in aqueous media, under physiological-like condition. Peroxidase-like activity was also taken into account in order to compare the residual oxidant activity with the antioxidant features. Finally, biochemical tests were carried out, to verify their capability to interact with amyloid peptides, in order to prevent their aggregation.

2. Results and discussion

The aim of this work is to synthesize small molecules that may mimic the active sites of superoxide dismutase and catalase enzymes. Structural modelling of these active sites with small coordination complexes is a useful tool to replicate their activity while understanding the reaction mechanisms in which they are involved[38]. This study presents the synthesis of mononuclear and dinuclear copper complexes stabilized by ligands based on an a N_3O donor set, similar to that observed in the active sites of the enzymes mentioned. The syntheses of the ligands were carried out exploiting a common intermediate, BPMA (bis-(2-pyridylmethyl) amine). Afterwards, the chelating ability and the catalytic activity were evaluated, in order to highlight their potential antioxidant biomimetic activity.

2.1 Synthesis and characterization of the intermediate BPMA

The BPMA (bis-(2-pyridylmethyl) amine) is the common intermediate for the synthesis of all the ligands studied. It was obtained according to the procedure described by *Hamman et al*.[39], through the reductive amination of pyridine-2-carboxaldehyde with 2-(aminomethyl)pyridine. In the first step, the mixing between the two reactants carried out the formation of the imine, that was reduced in the second step by $NaBH_4$ to obtain a brown oil (*Figure 29*). The BPMA was characterized by ESI-MS (+) and by ^{1}H-NMR. Concerning the ESI-MS (+) spectrum, it is possible to observe the peak at m/z 200.1, ascribed to the species $[HBPMA]^+$ (m/z calc: 200.12). The ^{1}H-NMR shows four signals of the aromatic proton (δ= 8.65 - 7.18 ppm), one signal for the methylene protons at 4.05 ppm and one for the proton of the group -NH at 2.67 ppm (*Appendix, chapter 5.1.1*).

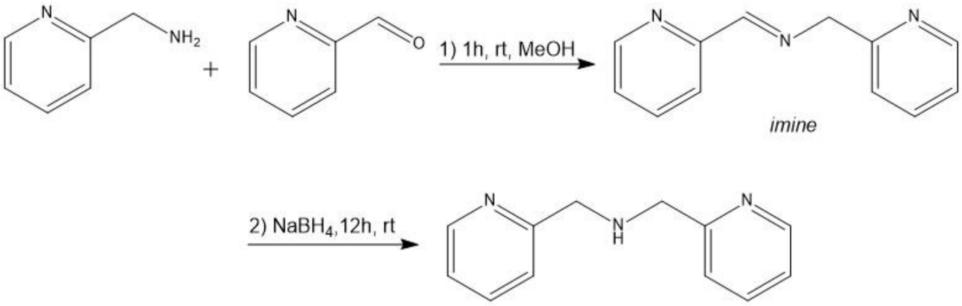

Figure 29: *reaction steps for BPMA synthesis*

2.2 Synthesis and characterization of ligands and complexes

2.2.1 Synthesis and characterization of HL1 and Cu(HL1)(ClO_4)$_2$

The reductive amination reaction was exploited for the synthesis of the ligand N-(2-hydroxylbenzyl)-N,N-bis(2-pyridylmethyl)amine (HL1), according to the procedure describe in literature by *Connor et al*.[40]. The mechanism involves, at first, the formation of an imine between BPMA and salicylaldehyde, which then is reduced to a tertiary amine by $NaBH_3CN$ (*Figure 30*)

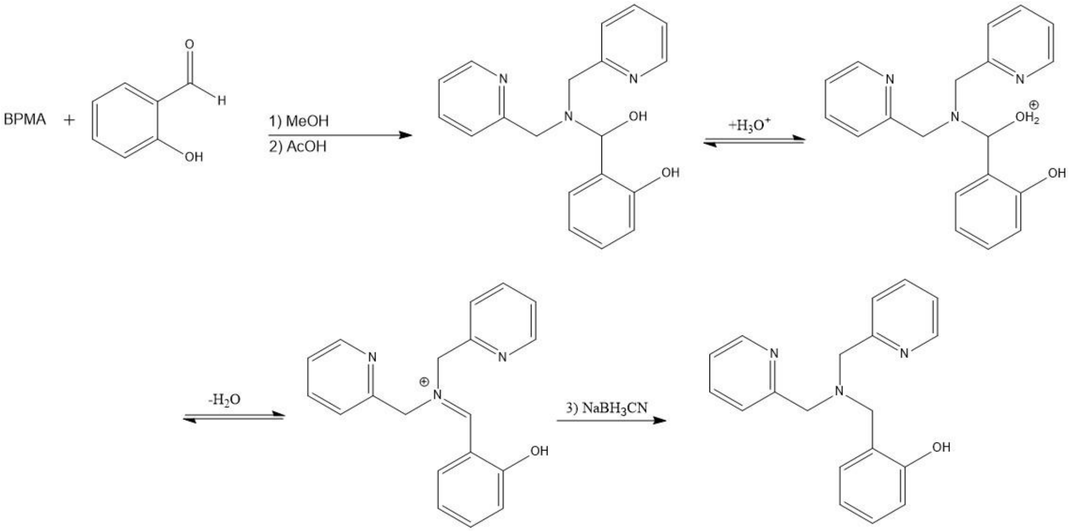

Figure 30: *Reaction mechanism for HL1 synthesis*

The ligand, obtained as a dark red oil was purified with a chromatographic column (silica, eluent DCM:MeOH 8:2, saturated with NH_4Cl), with a yield of 54% and characterized by:

- ESI-MS (+) in CH_3CN, that highlights the presence of the species $[H_2L1]^+$ at m/z 306.1 (m/z calc. 306.16) (*Appendix, chapter 5.1.2*);
- ^{1}H-NMR, that it is crowded from 8.62 to 6.77 ppm, corresponding to the aromatic protons zone (*Appendix, chapter 5.1.2*);
- FT-IR spectroscopy (ν<1800 cm^{-1}, *Figure 31*), where it is possible to observe the sharp signals relative to the C-H stretching of the aromatic groups (761 cm^{-1}), the C-N stretching vibration characteristic of the tertiary amine at 1374-1369 cm^{-1}, a band at 1242 cm^{-1} typical of the C-OH stretching of the phenolic group and the stretching of $C \overset{\cdots}{-} C$ and $C \overset{\cdots}{-} N$ of the aromatic ring from 1586 cm^{-1} to 1435 cm^{-1};

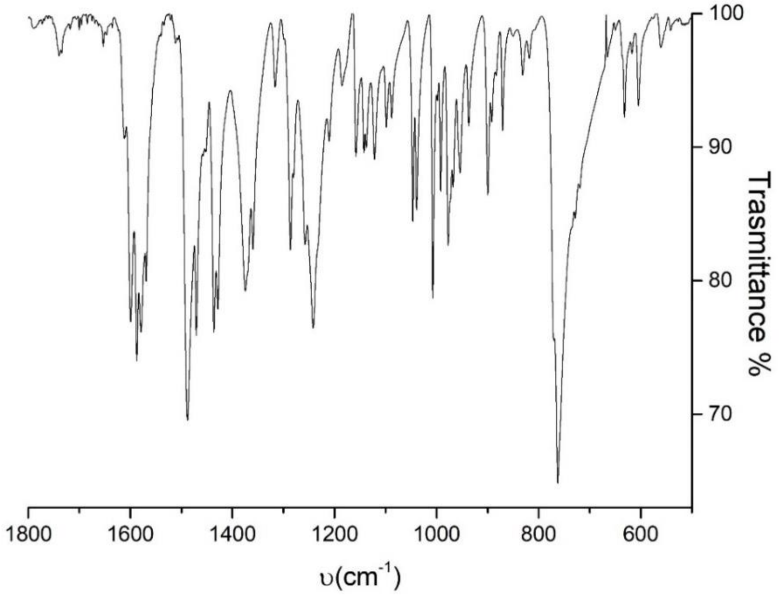

Figure 31: *FT-IR spectrum of HL1 from ν<1800 cm^{-1} (KBr)*

- UV-vis spectrum (*Figure 32*) highlights the presence of a band, with the maximum at 261 nm, typical of the $\pi \rightarrow \pi^*$ transition of the aromatic group. It is possible to observe two smaller bands at 256 nm and 267 nm and a shoulder at 279 nm.

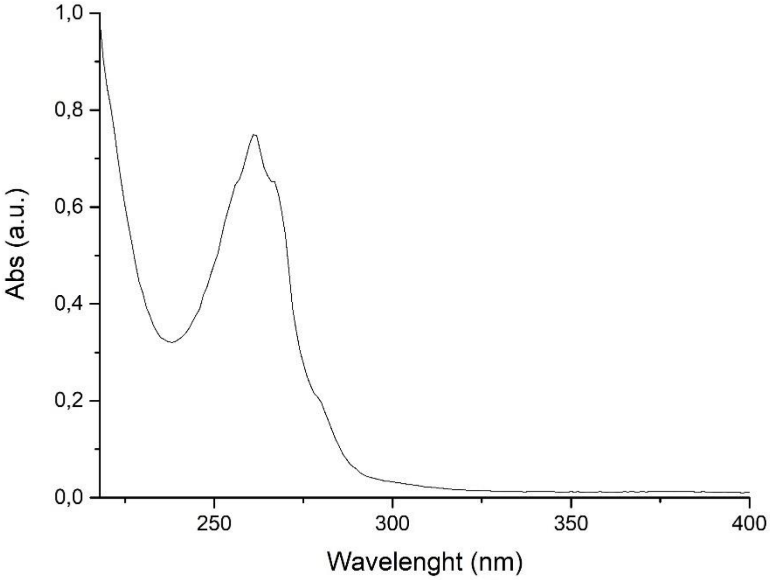

Figure 32: *UV-vis spectra of the ligand HL1 MeOH(5%v/v)/H_2O, 0.1 mM*

HL1 is an N_3O ligand, that in the mononuclear complex can coordinate the metal centre through the two pyridine nitrogen, the nitrogen of the tertiary amine and the oxygen of the alcoholic group. The synthesis of the mononuclear complex was carried out blending equimolar solutions of the ligand (yellow solution) and $Cu(ClO_4)_2$ (light blue solution) in MeOH or CH_3CN (*Figure 33*). When the two solutions were mixed, the resulting solution appeared blue. For the crystallization, the slow evaporation and liquid / vapour diffusion methods were used.

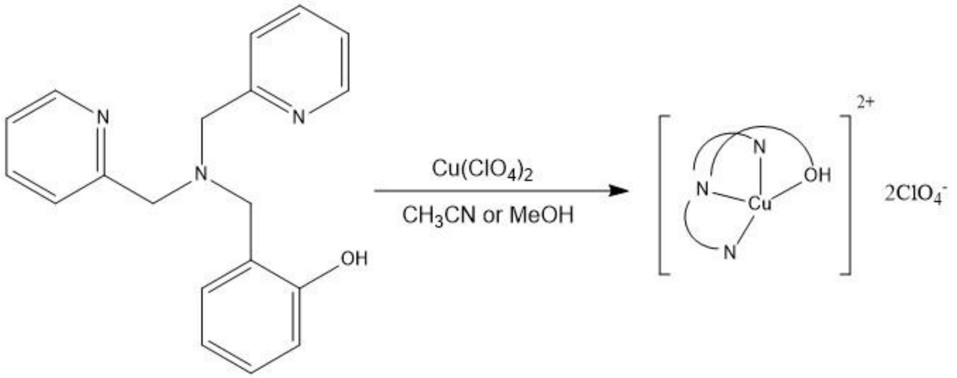

Figure 33: *Reaction for the synthesis of the mononuclear complex Cu(HL1)(ClO_4)$_2$*

The blue crystals obtained were characterized by:

- ESI-MS (+) in CH_3CN, which shows the characteristic peak at m/z 367.1 , relative to the species $[CuL1]^+$ (calc: 367.07) and a peak at m/z 403.1 (calc: 403.05), due to the adducts with Cl^- $[CuHL1Cl]^+$ (*Appendix, chapter 5.1.3*);
- Elemental analysis (*calc:* C, 37.79; H, 3.84, N, 6.96; *found:* C, 37.25; H, 3.78; N, 7.18) that highlights the presence of two molecules of water in the complex $[Cu(HL1)(ClO_4)_2]\cdot 2H_2O$;
- FT-IR spectroscopy ($\nu < 1400$ cm^{-1}, *Figure 34*), where it is possible to observe an intense band at 1101 cm^{-1} and a sharp one at 622 cm^{-1}, probably due to the stretching and the bending of the metal centre with the atoms of the ligand;

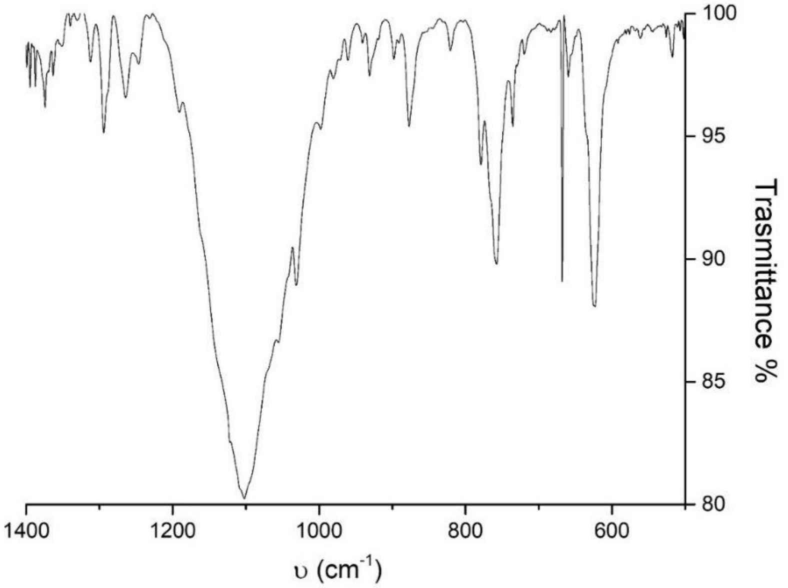

Figure 34: *FT-IR spectrum of the complex $Cu(HL1)(ClO_4)_2$ from $\nu < 1400$ cm^{-1} (KBr), the signal at 700 cm^{-1} is due to electrical spike.*

- UV-vis spectroscopy (*Figure 35*) highlights the presence of one band at 255 nm relative to the $\pi \rightarrow \pi^*$ transition of the aromatic groups and a band at 660 nm for the d→d transitions.

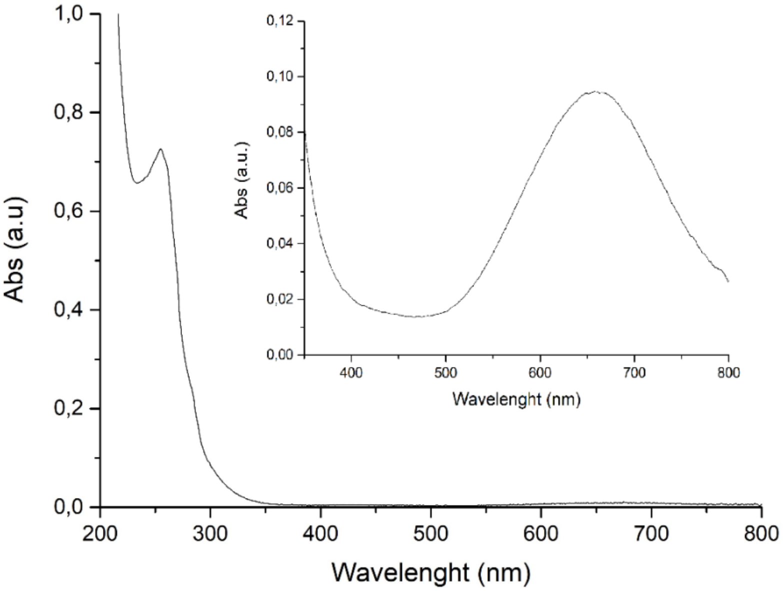

Figure 35: *UV-vis spectra of the complex Cu(HL1)(ClO_4)$_2$ in MeOH(5%v/v)/H_2O, 0.1 mM; zoom: band at 660 nm of the complex at the concentration 1.5 mM, in MeOH(5%v/v)/H_2O.*

In solution the mononuclear complex studied exhibits a distorted square-pyramidal arrangement. Complexes with this geometry, indeed, presents a single broad d-d absorption band at about 700 nm. Indeed, the UV-vis spectrum of Cu(HL1)(ClO_4)$_2$ points out the presence of a band at 660 nm, that confirms this arrangement.

The complex structure was also solved at the solid state by X-ray diffraction. The single-crystal X-ray diffraction study was carried out only for the crystals grown from CH_3CN/Et_2O. Crystals grown from MeOH/Et_2O, instead, decomposed too quickly once exposed to the air. The crystallographic study revealed that the crystallization solvent always enters the coordination sphere of the Cu (II) ions, occupying one of the four equatorial positions. Therefore, the crystallized complex is best formulated as [Cu(HL1)(CH_3CN)ClO_4](ClO_4)·CH_3CN.

The crystal structure of this compound is already present in literature, with acetone as the crystallization solvent[41]. The monomeric structure of [Cu(HL1)(CH_3CN)ClO_4](ClO_4)·CH_3CN contains a central copper metal atom with a distorted octahedral arrangement (*Figure 36*).

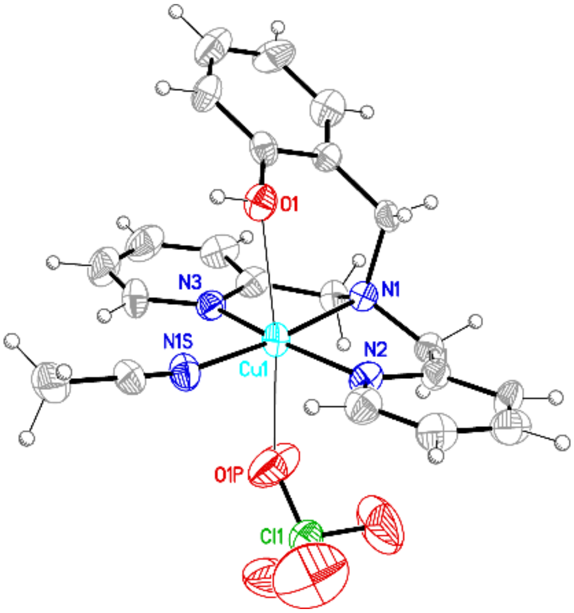

Figure 36: *Crystal structure of the complex [Cu(HL1)(CH_3CN)ClO_4](ClO_4)·CH_3CN.*

The square plane is defined by the three nitrogen atoms of the ligand (N1, N2, N3) and by the nitrogen atom of the solvent (N1S), CH_3CN. The oxygen of the alcoholic group of the ligand is in the apical position, while a perchlorate anion occupies the opposite position. The geometry is distorted, since the atoms bound to the copper metal centre do not lay in the equatorial plane and the bonds between the copper and the oxygens in the apical position are not perfectly perpendicular to the equatorial plane. Main bond lengths are shown in *Table 4*.

Table 4*: Selected bond lengths of [Cu(HL1)(CH_3CN)ClO_4](ClO_4)·CH_3CN*

Atoms	Distances (Å)
Cu1-N1	2.051
Cu1-N2	1.986
Cu1-N3	1.990
Cu1-N1S	2.012
Cu1-O1	2.494
Cu1-O1P	2.530

2.2.2 Synthesis and characterization of HL5 and Cu(HL5)(ClO_4)$_2$

The synthesis of the 2-{[Bis(pyridin-2-ylmethyl)amino]methyl}-6-methoxyphenol (HL5) was carried out following the same procedure used for the ligand HL1. In this case, the reagent employed for the reductive amination was the o-vanillin, that reacted with the secondary amine group of the BPMA. The imine formed was reduced to tertiary amine by $NaBH_3CN$ (*Figure 37*). The product was purified with a chromatographic column, using DCM : MeOH 8:2, saturated with NH_4Cl, as eluent, in order to obtain a dark orange oil, with 44% yield.

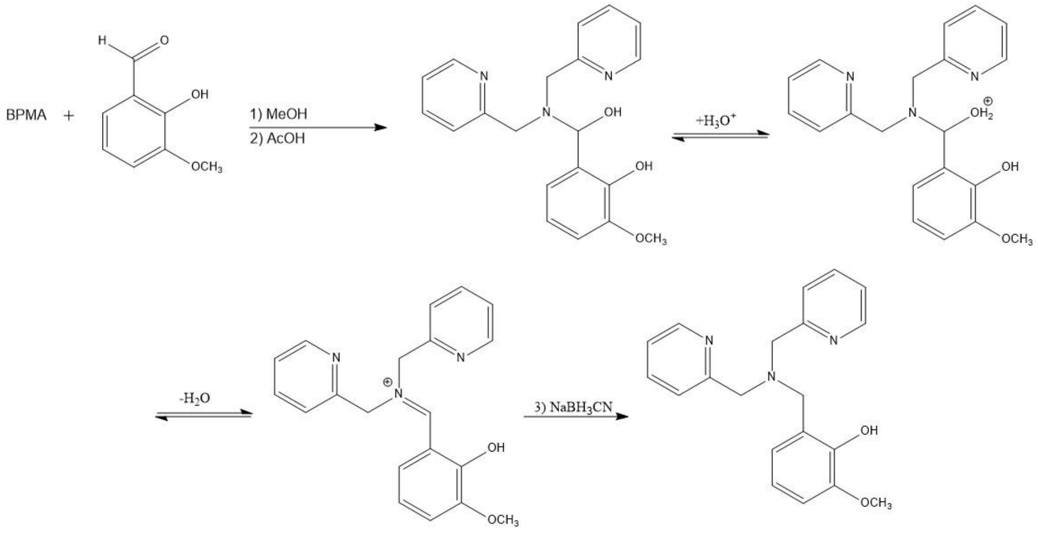

Figure 37: *Reaction mechanism of the ligand synthesis HL5*

The ligand was characterized by:

- ESI-MS (+) in CH_3CN, that shows one peak relative to the protonated species $[H_2L5]^+$ at m/z 336.2 (calc: 336.17) (*Appendix, chapter 5.1.4*);
- ^{1}H-NMR spectrum points out the signal at 3.90 ppm relative to the methoxy group, besides the peaks from 8.65 to 6.66 ppm, due to the protons on the aromatic rings (*Appendix, chapter 5.1.4*);
- FT-IR spectroscopy (ν<1800 cm^{-1}, *Figure 38*), in which it is possible to observe the same signals of HL1, due to the similar structure: the C-H stretching of the aromatic group at 762 cm^{-1}, the C-N stretching vibration

characteristic of the tertiary amine at 1373-1387 cm^{-1} and the stretching of C⩶C and C⩶N of the aromatic rings from 1585 cm^{-1} to 1433 cm^{-1}; the specific peak of this ligand is the C-O stretching of the methoxy group at 1249 cm^{-1}.

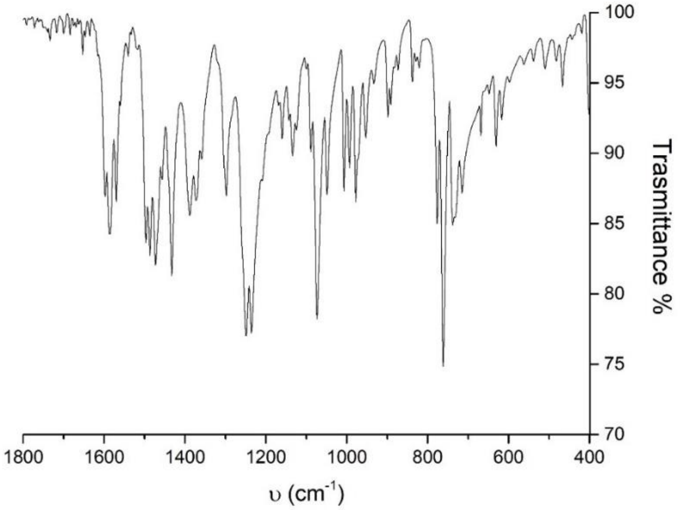

***Figure 38**: FT-IR spectrum of HL5 from ν <1800 cm^{-1} (KBr)*

- UV-vis (*Figure 39*), that points out a maximum absorption at 261 nm, due to π→π* transition of the aromatic group and the shoulders 256, 267 and 284 nm.

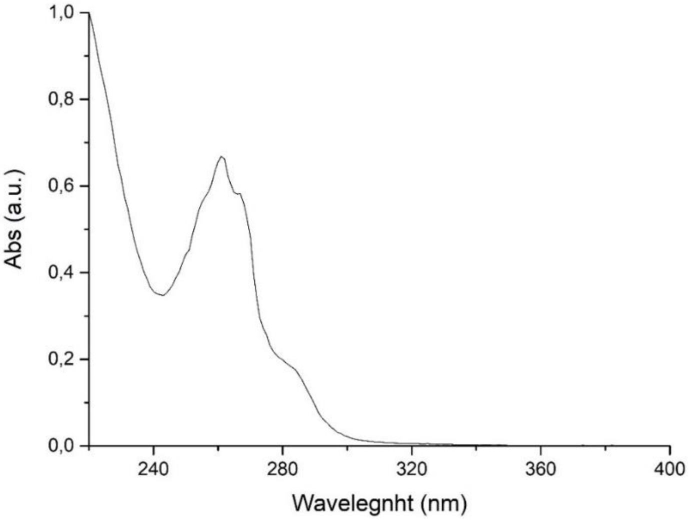

***Figure 39:** UV-vis spectra of the ligand HL5 MeOH(5%v/v)/H_2O, 0.1 Mm*

The synthesis of the mononuclear complex was carried out with the same procedure employed for the complex with HL1, using CH_3CN and MeOH as solvents (*Figure*

40). The blue crystals were obtained through the slow evaporation and liquid/ vapour methods.

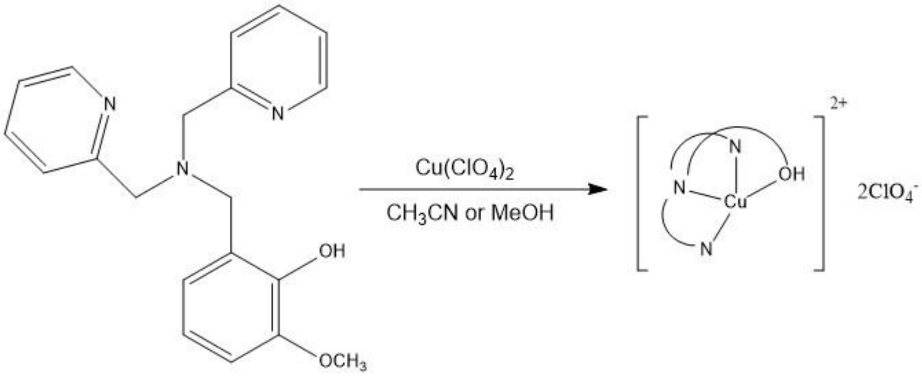

Figure 40: *Reaction for the synthesis of the mononuclear complex Cu(HL5)(ClO$_4$)$_2$*

The crystals were analysed by:

- ESI-MS (+) in CH_3CN, which shows two characteristic peak at m/z 397.1 (calc: 397.08) and m/z 497.0 (calc: 497.04) relative to the species $[CuL5]^+$ and $[CuHL5(ClO_4)]^+$, respectively (*Appendix, chapter 5.1.5*);
- Elemental analysis points out the presence of one molecule of water (*calc:* C, 39.01; H, 3.76; N, 6.82; *found:* C, 39.06; H, 4.00; N, 6.86, relative to the species $[Cu(HL5)(ClO_4)_2]\cdot H_2O$).
- FT-IR spectroscopy ($\nu < 1800$ cm^{-1},*Figure 41*), where it possible to observe, besides the signals relative to the ligand, a broad band at 1101 cm^{-1} and a sharp one at 625 cm^{-1}, due to the stretching and the bending of the copper with the atoms bounded.
- UV-vis spectroscopy (*Figure 42*) highlights the presence of one band at 256 nm relative to the $\pi \rightarrow \pi^*$ transition of the ligand aromatic groups and a shoulder at 287 nm, while at 662 nm it is possible to observe the d→d

absorption. The band at 662 nm is characteristic of a complex with a central metal copper in a distort square-pyramidal arrangement.

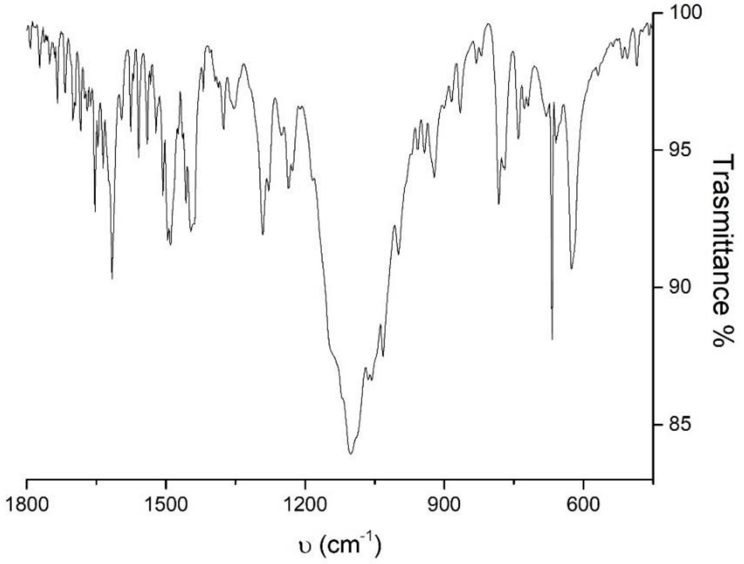

***Figure 41**: FT-IR spectrum of the complex Cu(HL5)(ClO$_4$)$_2$ from ν < 1800 cm^{-1} (KBr)*

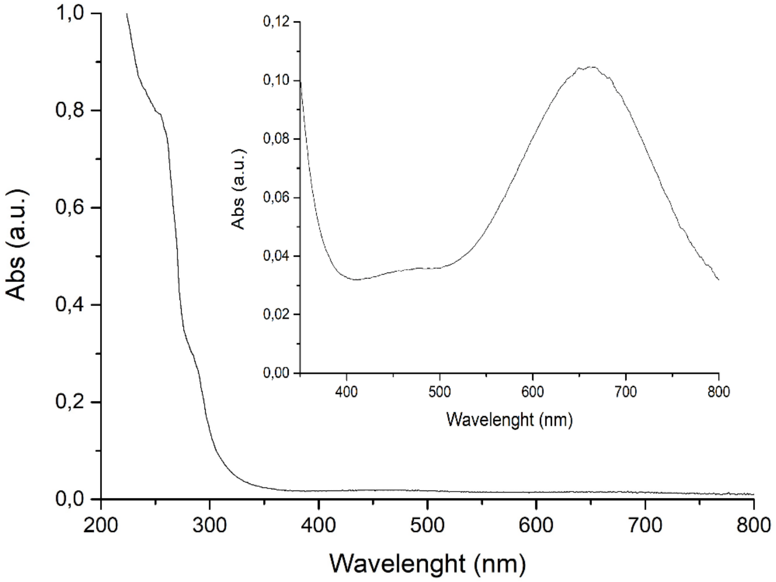

***Figure 42:** UV-vis spectra of the complex Cu(HL5)(ClO$_4$)$_2$ in MeOH(5%v/v)/H$_2$O, 0.1 mM; zoom: band at 662 nm of the complex at the concentration 1.5 mM, in MeOH(5%v/v)/H$_2$O.*

The geometry of the complexes was also studied by single-crystal X-ray diffraction. The data were collected for both the crystals grown from CH$_3$CN/Et$_2$O and from

MeOH/Et_2O. In the latter case, the experiment was carried out at 150K, in order to delay the crystal decomposition.

Since the crystallization solvent always enters the coordination sphere of Cu (II), occupying one of the equatorial position, as described for the complex with HL1, the crystallized complexes are formulated as $[Cu(HL5)(CH_3CN)ClO_4](ClO_4)$ and $[Cu(HL5)(MeOH)ClO_4](ClO_4)$.

The monomeric structures of $[Cu(HL5)(CH_3CN)ClO_4](ClO_4)$ and $[Cu(HL5)(MeOH)ClO_4](ClO_4)$ contain a central copper metal atom with a distorted octahedral arrangement (*Figure 43*). The square plane is defined by the three nitrogen atoms of the ligand (N1, N2, N3) and by the nitrogen atom of the solvent (N1S), in the case of the first structure, while for the crystal grown from MeOH/Et_2O, the forth atom in the square plane is the oxygen (O1S), relative to the methanol.

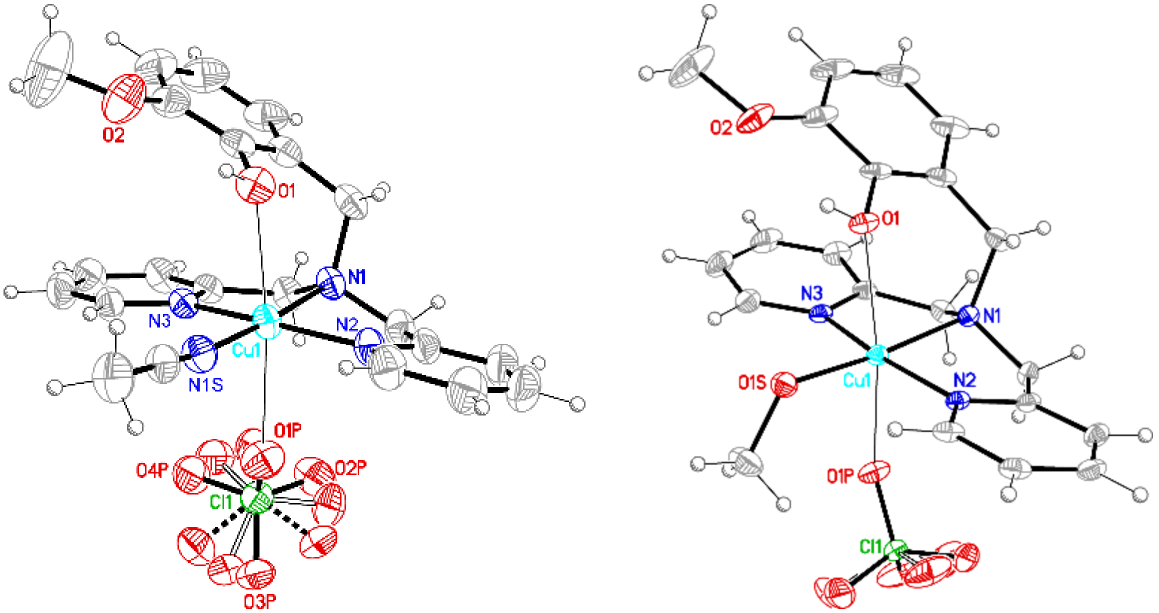

***Figure 43**: Crystal structure of $[Cu(HL5)(CH_3CN)ClO_4](ClO_4)$ (left) and $[Cu(HL5)(MeOH)ClO_4](ClO_4)$ (right).*

The oxygen of the alcoholic group of the ligand and a perchlorate anion occupy the apical positions. The distortion of the geometry is due to the atoms bound to the copper metal centre, which do not lay in the equatorial plane and to the bonds between the copper and the oxygen in the apical position that are not perfectly perpendicular to the equatorial plane. Main bond lengths are shown in *Table 5*.

***Table 5**: Selected bond lengths of [Cu(HL5)(CH_3CN)ClO_4](ClO_4) and [Cu(HL5)(MeOH)ClO_4](ClO_4)*

Atoms	**Distances (Å)for [Cu(HL5)(CH_3CN)ClO_4](ClO_4)**	**Distances (Å) for [Cu(HL5)(MeOH)ClO_4](ClO_4)**
Cu1-N1	2.019	2.027
Cu1-N2	1.978	1.968
Cu1-N3	1.975	1.979
Cu1-N1S/O1S	1.981	1.985
Cu1-O1	2.485	2.470
Cu1-O1P	2.575	2.504

2.2.3 Synthesis and characterization of HBPMP and $Cu_2(BPMP)(H_2O)_2(ClO_4)_3$

The ligand HBPMP was synthesized through an alkylation reaction of the secondary amine (BPMA) with 2,6-bis(chloromethyl)-4-methylphenol, according to the procedure described by *Torelli et al*.[42]. The mechanism is illustrated in the *Figure 44*.

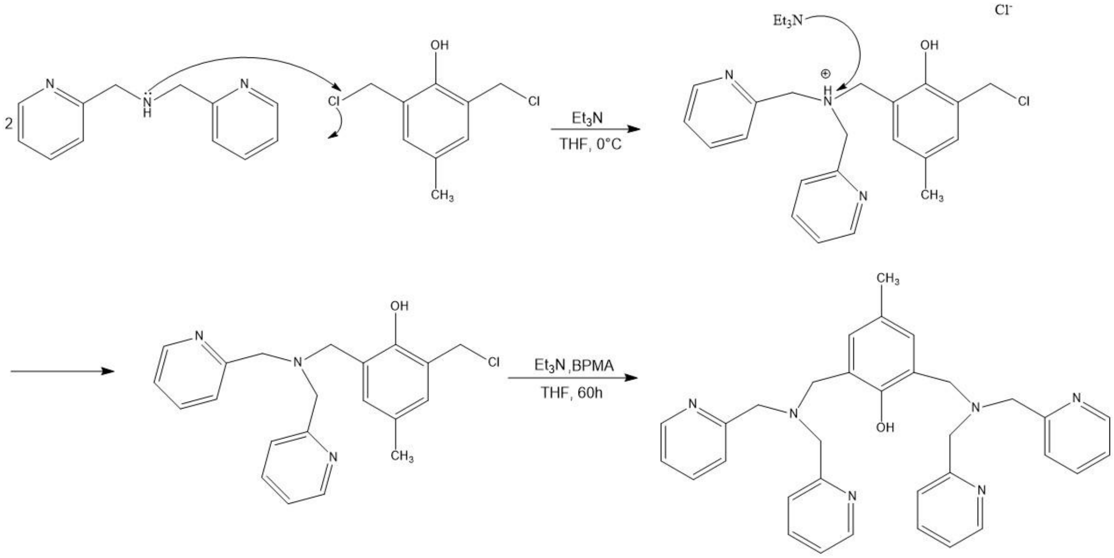

***Figure 44**: Reaction mechanism for the synthesis of HBPMP*

The product was purified with a chromatographic column, using a mixture of acetone:MeOH 8:2 as eluent, to obtain a pale yellow oil with 20% yield.

The ligand was characterized by:

- ESI-MS (+) in CH_3CN, that shows the peak at m/z 531.2 (calc: 531.29) ascribed to the species $[H_2BPMP]^+$ (*Appendix, chapter 1.5.6*);
- ^{1}H-NMR, that is crowded from 8.68 to 7.19 ppm, corresponding to the aromatic zone (*Appendix, chapter 1.5.6*);
- FT-IR spectrum (ν<1800 cm^{-1}, *Figure 45*), points out the sharp signals relative to the C-H stretching of the aromatic groups at 756 cm^{-1}, the C-N stretching vibration characteristic of the tertiary amine at 1362-1374cm^{-1}, a band at 1232 cm^{-1} typical of the C-OH stretching of the phenolic group and the stretching of C$\equiv$C and C$\equiv$N of the aromatic ring from 1586 cm^{-1} to 1430 cm^{-1}.

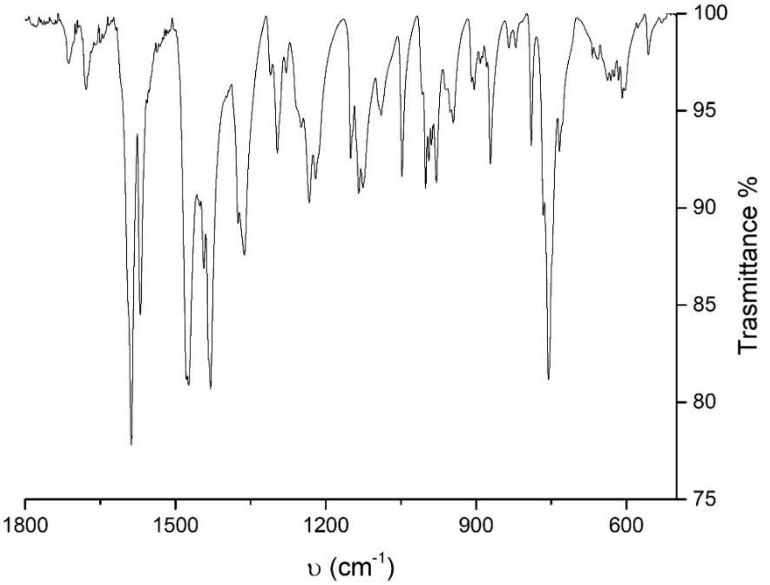

Figure 45: *FT-IR spectrum of HBPMP from ν<1800 cm^{-1} (KBr)*

- UV-vis spectroscopy (*Figure 46*), that highlights the presence of a band characteristic of the $\pi\rightarrow\pi^*$ transition of the aromatic group at 261 nm, with two shoulders at 289 nm and 345 nm.

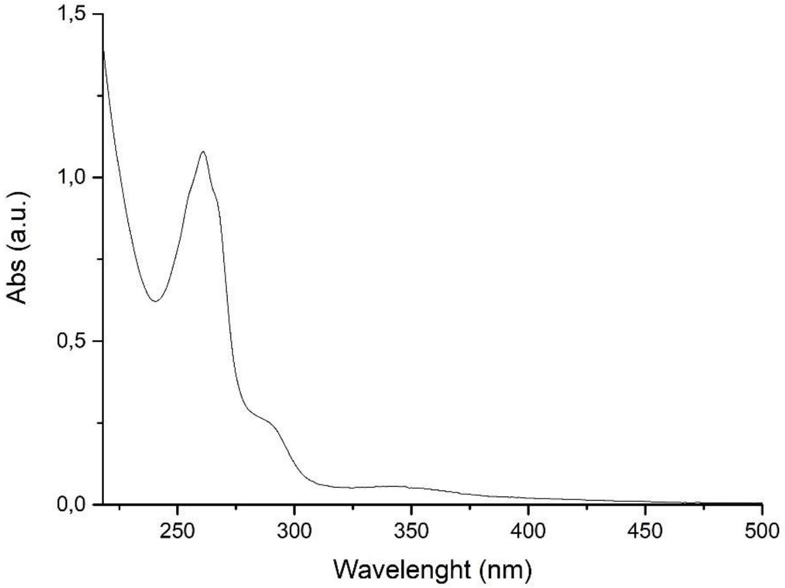

Figure 46*: UV-vis spectra of the ligand HBPMP MeOH(5%v/v)/H_2O, 0.1 mM*

Concerning the synthesis of the dinuclear complex $[Cu_2(BPMP)(H_2O)_2](ClO_4)_3$, the procedure of *Torelli et al.*[42] was adopted with some modification (*Figure 47*). The ligand HBPMP was dissolved in a solution of water and acetone, after, a double amount of copper perchlorate was added dropwise to obtain a brown solution. The dark green crystals were obtained with the interface and slow evaporation technique.

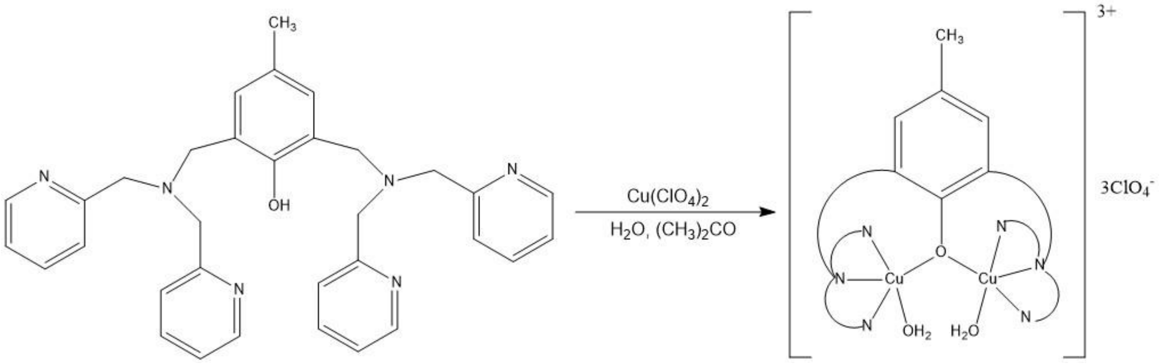

Figure 47: *Reaction of the $[Cu_2(BPMP)(H_2O)_2](ClO_4)_3$ synthesis*

The crystals were studied by:

- ESI-MS (+) in H_2O, that shows the peaks at 727.2 (calc: 727.12); and 745.2 (calc: 745.18) attributable to the species $[Cu(BPMP)(H_2O)_2(ClO_4)]^+$ and $[Cu(BPMP)(H_2O)_3(ClO_4)]^+$, respectively (*Appendix, chapter 1.5.7*);

- Elemental analysis differs slightly to the calculated values due to the presence of four molecule of water (*calc*: C, 37.28; H, 4.27; N, 7.90; *found:* C, 37.97; H, 4.11; N, 7.69, attributable to the species $[Cu_2(BPMP)(H_2O)_2(ClO_4)_3]\cdot 4H_2O$).
- FT-IR spectroscopy (ν< 1800 cm^{-1}, *Figure 48*), where it is possible to observe, beside the signals relative to the ligand, a broad band at 1096 cm^{-1} and a sharp one at 625 cm^{-1}, due to the stretching and the bending of the copper with the atoms bounded.

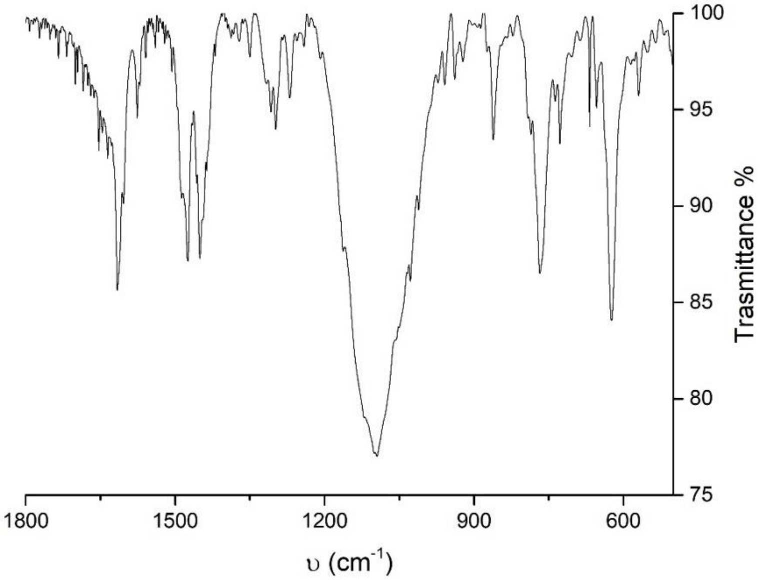

***Figure 48**: FT-IR spectrum of the complex $[Cu_2(BPMP)(H_2O)_2][(ClO_4)_3]$ from ν < 1800 cm^{-1} (KBr)*

- UV-vis spectrum (*Figure 49*) points out a band at 255 nm and a shoulder at 303 nm, due to the $\pi\rightarrow\pi^*$ transition of the ligand aromatic group, while at 460 nm it is possible to notice a band, most probably due to CT (L→M) transition and one at 700 nm of the d→d absorption.

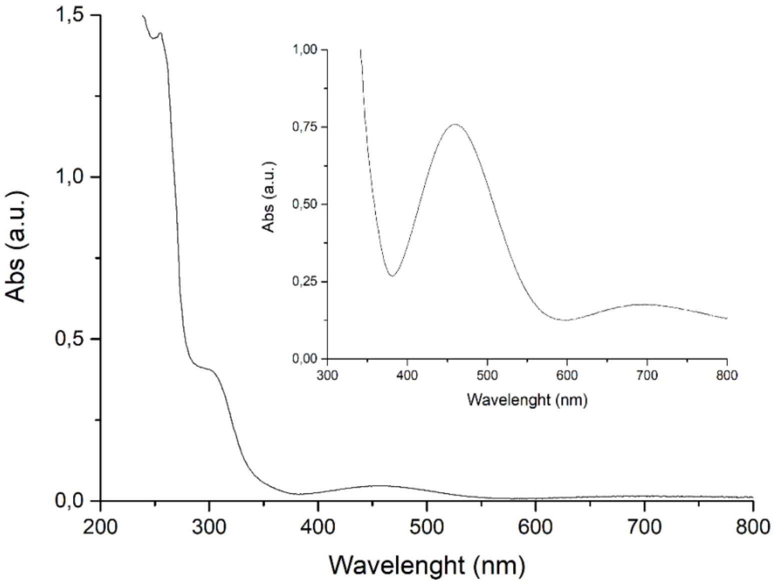

***Figure 49**: UV-vis spectra of the complex [Cu_2(BPMP)(H_2O)$_2$][(ClO_4)$_3$] in H_2O, 0.1 mM; zoom: band at 460 nm and 700 nm of the complex at 1.5 mM concentration.*

In the dinuclear complex studied, each copper atom is pentacoordinated, bound by three nitrogen atom: one from the tertiary amine and two from pyridines, and by two oxygen atoms from the phenoxo bridge and a terminal water molecule. The X-ray structure, reported in literature[42] points out a square pyramidal distorted geometry, whose apical position is occupied by the bridging phenoxo oxygen (*Figure 50*). The square plane is defined by the three nitrogen atoms of the ligand (N1,N2,N3) and by the oxygen of the water molecule (O_2). The copper atoms lies 0.21 Å out of the basal plane toward the apical oxygen of the phenoxo group (O1).The two copper atoms are on different sides of the phenolate plane. Due to the oxygen of the phenoxo group in the apical position of both the copper atoms, the intermetallic distance is 4.139Å. This distance is the longest one observed for a singly phenoxo-bridged dicopper (II) complex in which both copper are in tetragonal pyramidal environment. The distorted square pyramidal geometry is also confirmed by UV-vis spectra since five-coordinate square pyramidal Cu(II) complexes exhibit a single broad d→d absorption band at 700 nm with no absorption maximum beyond λ>800 nm[43].

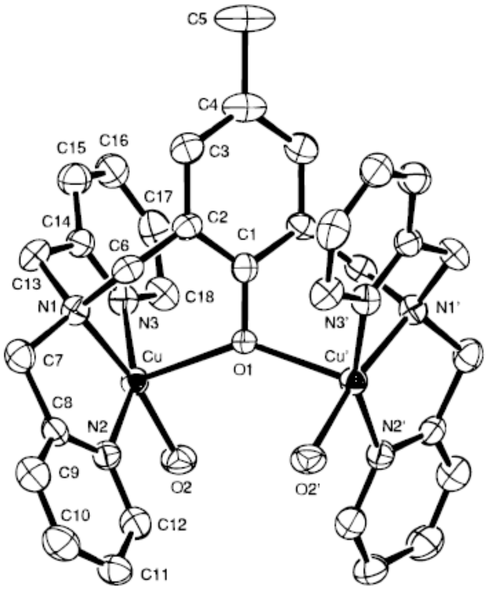

***Figure 50**: X-ray structure of the complex* $[Cu_2(BPMP)(H_2O)_2][(ClO_4)_3]$[43]

The principal interatomic distances are reported in the *Table 6*.

***Table 6:** principal interatomic distances for the complex* $[Cu_2(BPMP)(H_2O)_2][(ClO_4)_3]$

Atoms	**Distances (Å)**
Cu-Cu’	4.139
Cu-O1	2.189
Cu-O2	2.005
Cu-N1	2.027
Cu-N2	1.993
Cu-N3	2.000

The interesting feature of this complex is its high solubility in water.

2.3 Chelating ability of the ligands

The coordination ability was evaluated through a titration of the ligands with increasing amount of Cu(II) solution. As regarding the ligands HL1 and HL5, the experiments were carried out with two different concentration of the ligands, 0.1 mM and 1.5 mM, whereby the last concentration is suitable to observe the changes in the d-d bands. While, for HBPMP, due to the precipitation of the ligand at high concentration, the titration was recorded only at 0.1 mM . 0.1 eq of copper (II) were added in each aliquot (*Experimental section, chapter 4.6*). The formation of the complex is evaluated by UV-vis spectroscopy, observing the absorbance changes. For all the three ligands, the spectra show an increase in the absorbance of the UV-vis band due to the π→π* transition of the aromatic rings ("hyperchromic" effect) and a simultaneous change in the shape of the bands (*Figure 51*, *Figure 52*, *Figure 53*). In the spectra of HL1 and HBPMP it is possible to observe a shift to lower wavelength (blue shift). Moreover, the titration of HL1 highlights the presence of two isosbestic points (*Table 7*), that suggest an equilibrium between the ligand and the other species, formed during the addition of copper (II). The spectra of HL1 and HL5 at 1.5 mM points out an increase in the absorbance of the d→d band, due to formation of the complex.

***Table 7**: Maximum absorptions of π→π* and d→d bands, blue shift and isosbestic point, obtained from the titration of the ligands with Cu(II). Conditions for the π→π* bands [ligand]= 0.1mM; [copper(II)]=0.01M; for the d→d, only for HL1 and HL5, [ligand]= 1.5mM, [copper(II)]= 0.15M. 2.5μL of copper were added in each addition, till reach 75 μL (3 equivalent).*

Ligands	λ_{max} π→π*(nm)	λ_{max} d→d (nm)	Blue shift (nm)	Isosbestic points (nm)
HL1	261	665	5	266, 269
HL5	260	661	-	-
HBPMP	261	700	7	-

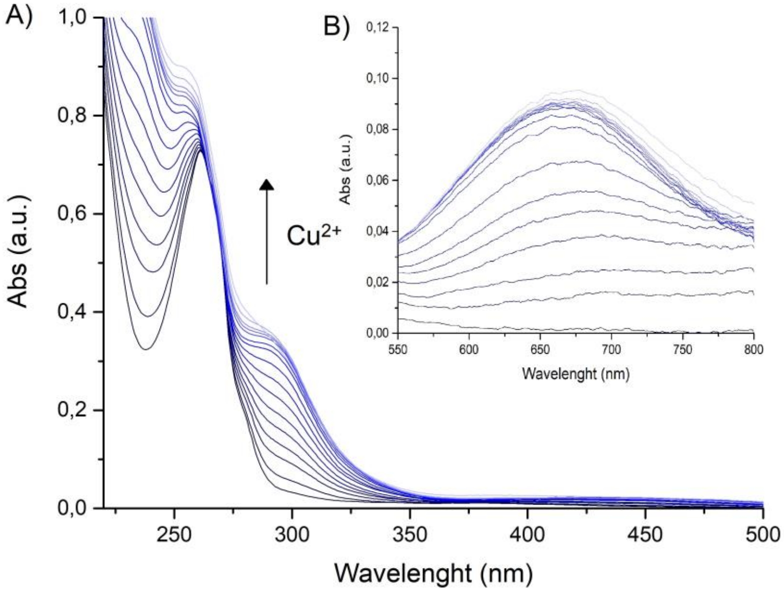

***Figure 51**: UV-vis spectra collected during HL1 titration: spectra A) shows* π→π* band*, B) d→d band. The titration was carried out using the following concentration: 0.01M Cu(II) in water and 0.1 mM of the ligand, for the* π→π* *band, and 0.15M Cu(II) in water and 1.5mM of the ligand. The solutions of the ligand were obtained from a stock solution in MeOH.*

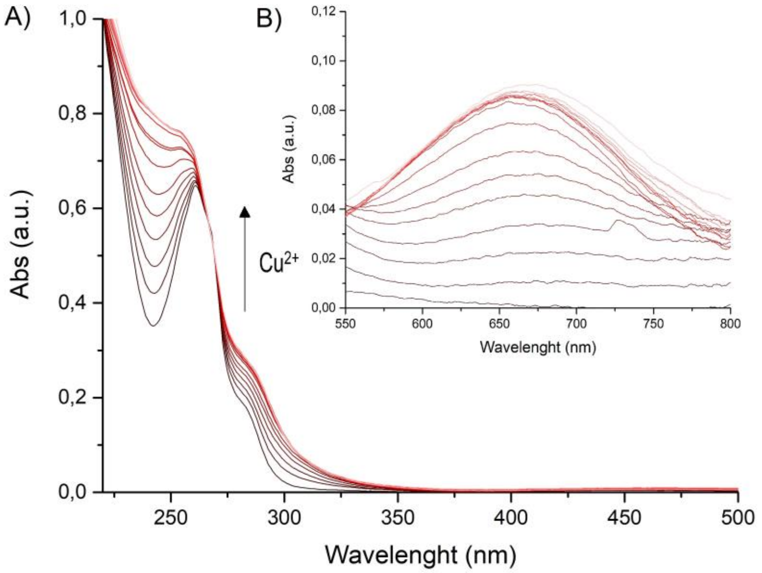

***Figure 52:** UV-vis spectra of HL5 titration: spectra A) shows* π→π* band*, B) d→d band. The titration was carried out using the following concentration: 0.01M Cu(II) in water and 0.1 mM of the ligand, for the* π→π* *band, and 0.15M Cu(II) in water and 1.5mM of the ligand. The solutions of the ligand were obtained from a stock solution in MeOH.*

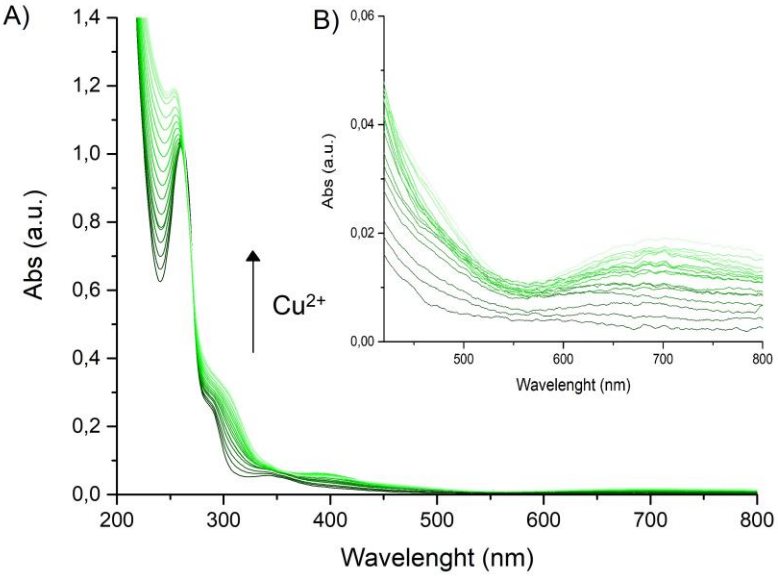

***Figure 53**: UV-vis spectra of HBPMP titration: spectra A) shows π→π* band, B) d→d band. The titration was carried out using the following concentration: 0.01M Cu(II) in water and 0.1 mM of the ligand. The solutions of the ligand were obtained from a stock solution in MeOH.*

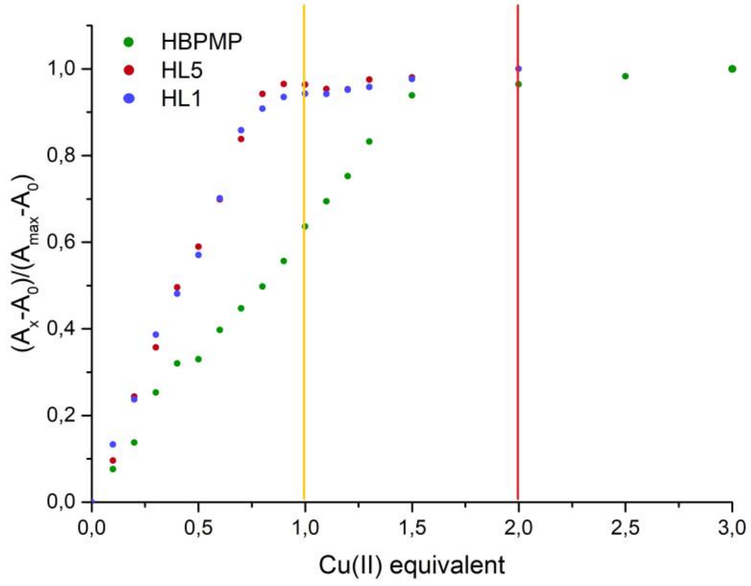

***Figure 54**: graph of the relative absorbance variation with number of Cu(II) equivalent, obtained from the titration of HL1 (blue), HL5 (red) and HBPMP (green). For HL5 and HL1 at λ_{max} of d→d band, HBPMP at 290 nm.*

The graph *“Abs at λ_{max} vs Cu(II) equivalent”* highlights the formation of 1:1 complex for the ligands HL1 and HL5, while for HBPMP the formation of dinuclear complex is observed. As to the mononuclear complexes, there is a progressive increase in the absorbance at the maximum absorption (d→d), until reaching the plateau, when the ratio between Cu(II) and the ligands is 0.9:1. On the other hand, for the dinuclear complex, the increase of absorbance has been evaluated at 290 nm, until reaching the plateau when the ratio between Cu(II) and the ligand is 1.5:1 (*Figure 54*). The differences with respect to the expected ratios, 1:1 and 2:1, are likely due to the occurrence of different protonation states for the ligands (see next paragraphs).

The Benesi-Hildebrand equation (19) was applied for the calculation of the binding constant, which can be obtained from the slope of the line of the graph "*1/(A-A$_0$) vs 1/[Cu(II)]".*

$$\frac{1}{\mathrm{A}-\mathrm{A}_0}=\frac{1}{\{\mathrm{K}(\mathrm{A}_{\mathrm{max}}-\mathrm{A}_0)[\mathrm{Cu}^{2+}]\}}+\frac{1}{(\mathrm{A}_{\mathrm{max}}-\mathrm{A}_0)} \quad (19)$$

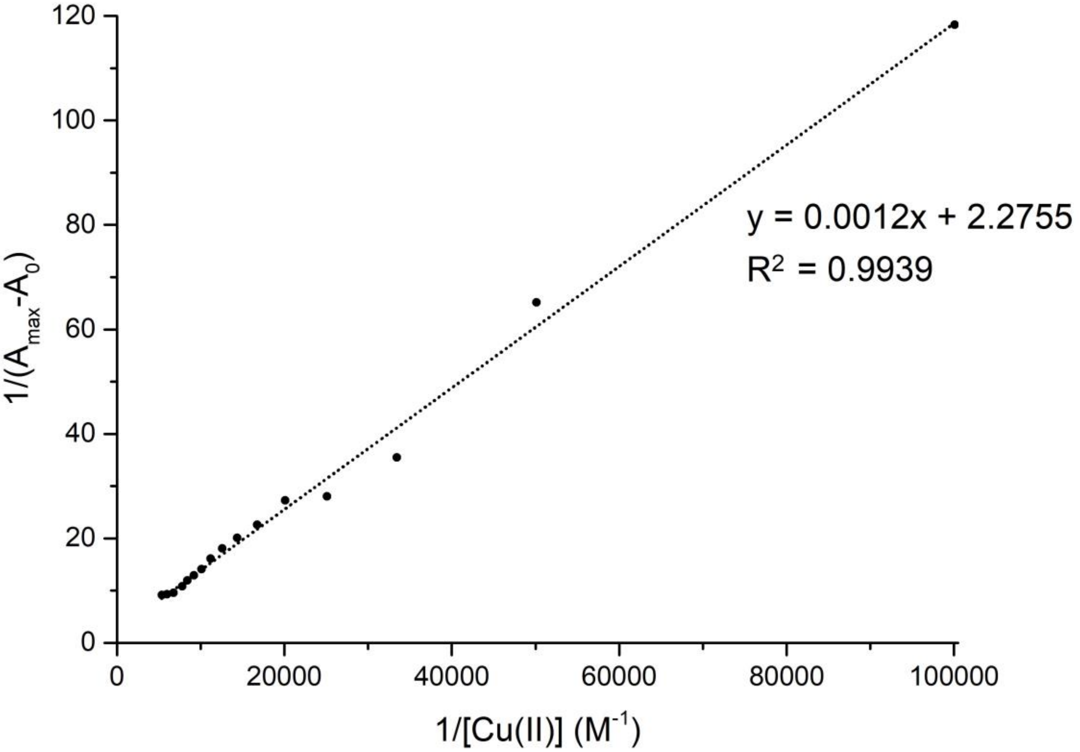

***Figure 55**: Graphic for the calculation of the binding constant of HBPMP with Cu(II)*

Figure 55 shows the trend achieved for the ligand HBPMP, the behaviour of the ligands HL1 and HL5 is the same, but with different slopes and intercepts. The values obtained from these calculation are in *Table 8*.

***Table 8**: Binding constants of HL1, HL5 and HBPMP derived through the Benesi-Hildebrand method*

Ligands	K_{bind} (M^{-1})
HL1	$6,3*10^3$
HL5	$4,4*10^3$
HBPMP	$7,8*10^3$

The highest binding constant value is the one of HBPMP, this ligand is the best chelating agent for the copper (II). HL1 and HL5 have values of the same order of magnitude, but the binding constant of HL1 is higher than the one of HL5. However, this values are lower than the ones observed for the free SOD with Cu (II), which range from 10^5 to 10^6 M^{-1} [44].

The stoichiometry of the complexes generated in situ was better evaluated through the Job's Plot (*Experimental section, chapter 4.6*). The Job's plot confirms the formation of the 1:1 complex for HL1 and HL5, since the maximum absorption value is obtained for equal molar fractions of ligand and Cu (II). On the other hand, for HBPMP the maximum is shifted to higher molar fractions of Cu(II). This is a typical behaviour expected for a dinuclear complex. For the HBPMP, a lower overall concentration was used, moreover the data were acquired when the Cu (II) equivalents were equal to 0.5, due to the precipitation of the free ligand at higher molar fractions (*Figure 56*).

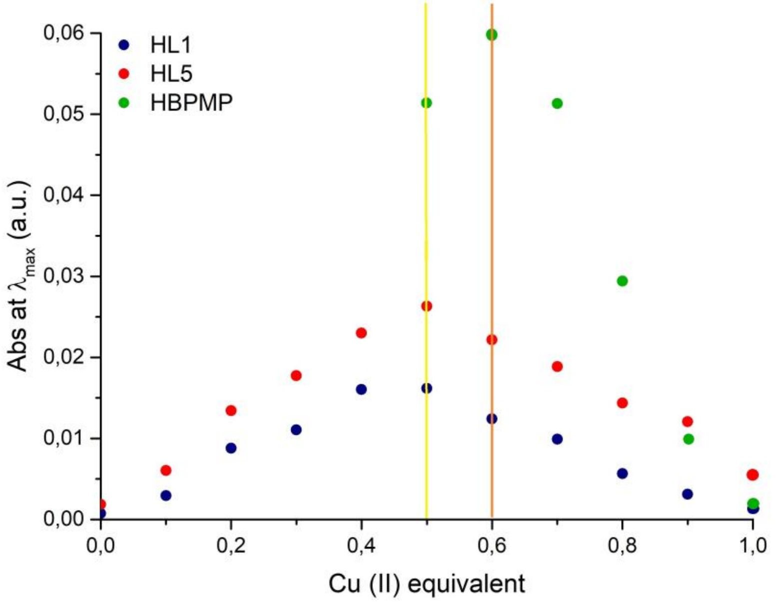

***Figure 56**: Job's plot at λ_{max} of d→d band generated from the formation of copper complex with HL1 (blue), HL5 (red), HBPMP (green). Solution concentration 0.75 mM of copper (II) and 0.75 mM of the ligands HL1 and HL5. For HBPMP the conditions were 0.35 mM of Cu (II) and 0.35 mM of ligand. The solution of copper was made in water, while the ligands solutions were obtained from a stock solution in methanol.*

The behaviour of the ligand and the corresponding in situ-formed complexes were studied as a function of pH by UV-Vis spectroscopy. As regards the spectrum of the ligand HL1, it is possible to observe a decrease of absorbance at 263 nm (*hypochromic effect*) and a shift of the π→π* band to lower wavelength (261 nm), increasing the pH. Moreover, when the pH is 9.72, a shoulder and a band appear at 299 nm and 379 nm, respectively. For the study of in situ-formed complex the ratio used is Cu (II): HL1 1:1.2, to avoid the copper precipitation. Increasing the pH till 7.72 the absorbance of the band at 261 nm decrease, then increases at basic pH. From pH 7.72 it is possible to observe the formation of a shoulder at 296 nm. At basic pH a band appears at 473 nm, and then disappears at pH 9.72, with the formation of a band at 391 nm (*Figure 57*).

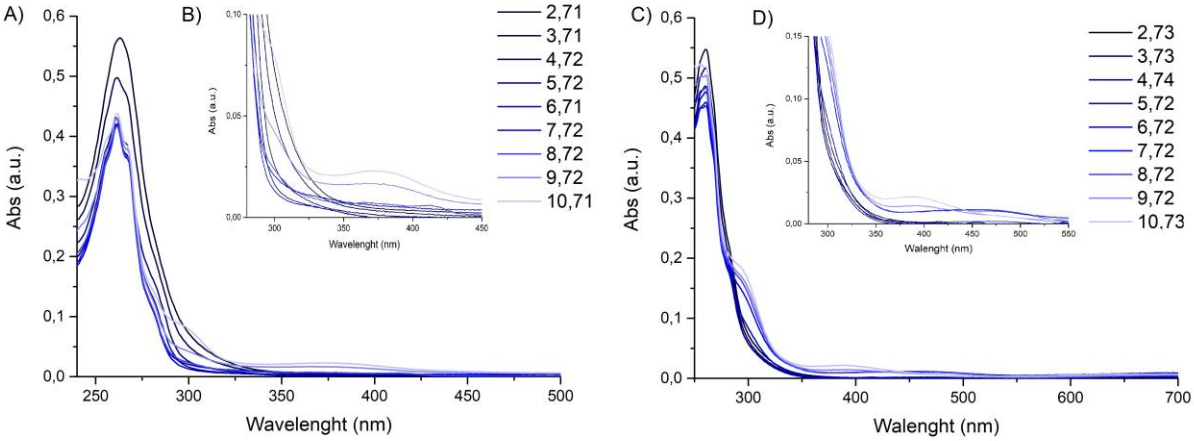

***Figure 57**: A) pH-metric titration of the ligand HL1, B) zoom to highlight the band at 379 nm; C) pH-metrical titration of in situ-formed complex Cu:HL1 1:1.2, D) zoom to highlight the bands at 473 nm and 391 nm. The titrations start from pH about 2.7 to pH 10.7, each colour variation represents the change in pH of one unit, using a solution of NaOH. The solutions were in DMSO (5% v/v)/H_2O(HCl/KCl), 0.76mM.*

The pH-metrical titration of the ligand HL5 points out a *hypochromic effect* till pH 5.67, then, at pH higher, the absorbance increases. When the pH is 5.67 a shoulder appears at 283 nm and at basic pH there is a band at 391 nm. As regards in situ-formed complex, the ratio adopted is Cu:HL5 1:1.2. The trend at 261 nm is the same as the one observed for the ligand. Moreover, it is possible to notice that the shoulder at 285 nm, present at low pH shifts to 300 nm at basic pH. At 464 nm there is a band from pH 6.68 to 9.69, that then moves to 418 nm when the pH is higher (*Figure 58*).

Concerning the ligand HBPMP, it is possible to observe a decrease of absorbance at 261 nm, increasing the pH. Furthermore, when the pH is about 5, a shoulder appears at 290 nm, while the band at 350 nm moves to higher wavelength. The spectra were collected till pH of about 9, because of the precipitation of the ligand. For the study of in situ-formed dinuclear complex the ratio used is HBPMP:Cu 1:2. Increasing the pH, a shoulder and a band appear respectively at 299 and 397 nm, while the band at 466 nm disappears above pH 5.68 (*Figure 59*).

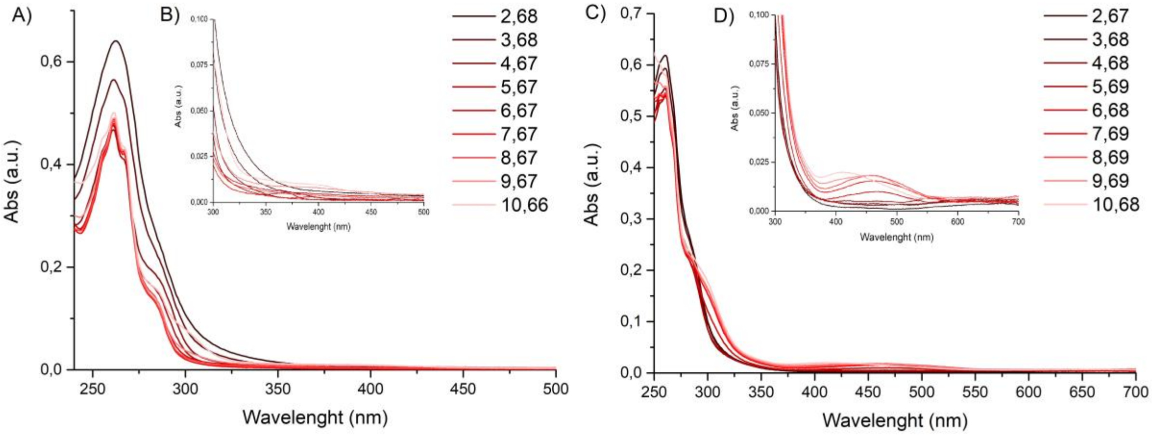

Figure 58: *A) pH-metric titration of the ligand HL5, B) zoom to highlight the band at 391 nm; C) pH-metrical titration of in situ-formed complex Cu:HL5 1:1.2, D) zoom to highlight the bands at 464 and 418 nm. The titrations start from pH about 2.7 to pH 10.7, each colour variation represents the change in pH of one unit. The solutions were in DMSO (5% v/v)/H_2O(HCl/KCl), 0.71mM.*

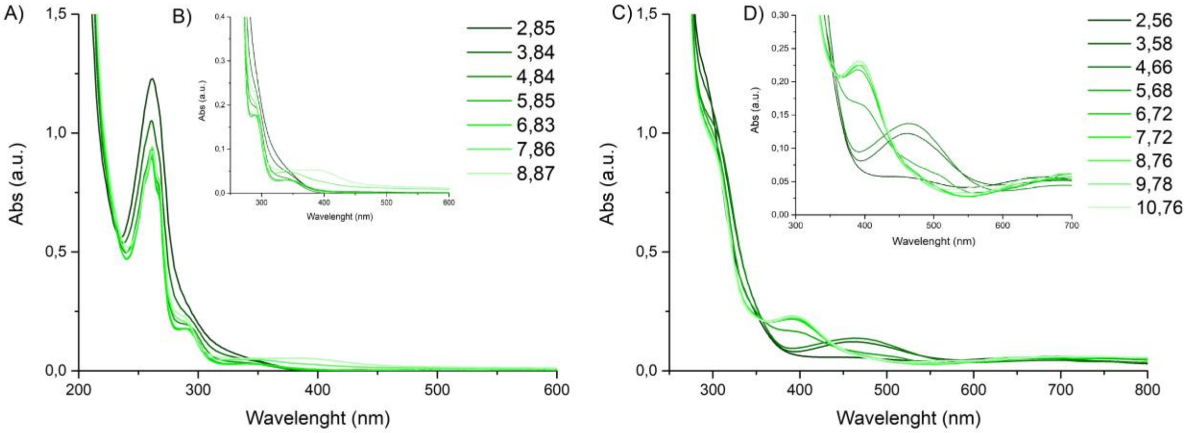

Figure 59: *A) pH-metric titration of the ligand HBPMP, B) zoom to highlight the band at 350 nm; C) pH-metrical titration of in situ-formed complex Cu:HBPMP 2:1, D) zoom to highlight the bands at 397 and 466 nm. The titrations start from pH about 2.7 to pH 10.7, each colour variation represents the change in pH of one unit. The solutions were in DMSO (5% v/v)/H_2O(HCl/KCl), 0.43mM.*

The ligands and complexes pH-metrical titration points out that the pH variation causes the formation of different species in solution. To better understand the species generated at different pH, potentiometric titrations were carried out. These experiments were performed in collaboration with the research group of the *Professor Justyna Brasun at the Medical University of Wroclaw (PL).* The titrations allowed the construction of speciation curves, that is, curves highlighting the formation of the species generated at different pH. As regards the ligands, the speciation curves were obtained from the titration of a ligand solution, changing the pH. Through the addition of 14 μL of NaOH 0.1M to a ligand solution (0.1mM in DMSO 5%(v/v)/H_2O (HCl/KCl), initial pH 2.7), the distribution curves (*Figure 60 and Figure 61*) and the acid associations constants were calculated (*Table 9 and Table 10*).

As regard the ligands HL1 and HL5, Lx^- is the ligand with the deprotonated phenol, HLx is the original ligand, $[H_2Lx]^+$ is the ligand with the tertiary amine protonate, while $[H_3Lx]^{2+}$ and $[H_4Lx]^{3+}$ represent the ligand with pyridine nitrogens protonated (*Table 9*). Concerning the ligand HBPMP, L^- is the ligand with the deprotonated phenol, HL is the original ligand, $[H_2L]^+$ and $[H_3L]^{2+}$ are the species with the tertiary ammine protonated, while H_5L represents the ligand with pyridine nitrogen protonated (*Table 10*). These attributions were made by comparing the data obtained experimentally with those present in the literature, for similar compounds[45,46].

Table 9*: Overall (log β_i) and stepwise (log K_i) protonation constants of the ligands HL1 (x=1) and HL5 (x=5), obtained from potentiometric titration.*

Equilibrium reaction	**log βi x=1**	**log βi x=5**	**Equilibrium reaction**	**log Ki x=1**	**log Ki x=5**
$Lx^- + H^+ \rightleftharpoons HLx$	10.01	10.52	$Lx^- + H^+ \rightleftharpoons HLx$	10.01	10.52
$Lx^- + 2H^+ \rightleftharpoons [H_2Lx]^+$	16.23	16.76	$HLx + H^+ \rightleftharpoons [H_2Lx]^+$	6.22	6.24
$Lx^- + 3H^+ \rightleftharpoons [H_3Lx]^{2+}$	21.09	21.74	$[H_2Lx]^+ + H^+ \rightleftharpoons [H_3Lx]^{2+}$	4.86	4.98
$Lx^- + 4H^+ \rightleftharpoons [H_4Lx]^{3+}$	24.52	25.41	$[H_3Lx]^{2+} + H^+ \rightleftharpoons [H_4Lx]^{3+}$	3.43	3.67

Table 10: *Overall (log β_i) and stepwise (log K_i) protonation constants of the ligand HBPMP, obtained from potentiometric titration.*

Equilibrium reaction	**log βi**	**Equilibrium reaction**	**log Ki**
$L^- + H^+ \rightleftharpoons HL$	7.01	$L + H^+ \rightleftharpoons HL$	7.01
$L^- + 2H^+ \rightleftharpoons [H_2L]^+$	12.89	$HL + H^+ \rightleftharpoons [H_2L]^+$	5.88
$L^- + 3H^+ \rightleftharpoons [H_3L]^{2+}$	17.40	$[H_2L]^+ + H^+ \rightleftharpoons [H_3L]^{2+}$	4.51
$L^- + 4H^+ \rightleftharpoons [H_4L]^{3+}$	20.95	$[H_3L]^{2+} + H^+ \rightleftharpoons [H_4L]^{3+}$	3.55
$L^- + 5H^+ \rightleftharpoons [H_5L]^{4+}$	24.08	$[H_4L]^{3+} + H^+ \rightleftharpoons [H_5L]^{4+}$	3.13

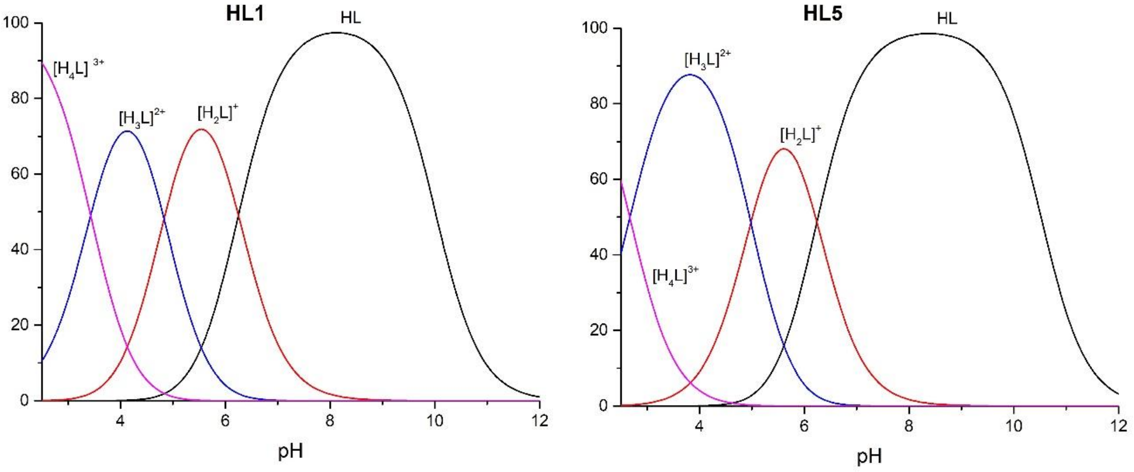

Figure 60*: Speciation curves for the ligands HL1 and HL5. Conditions: [ligands]= 0.07mM in DMSO (5%v/v)/(H_2O/HCl,KCl, starting pH=2.7).*

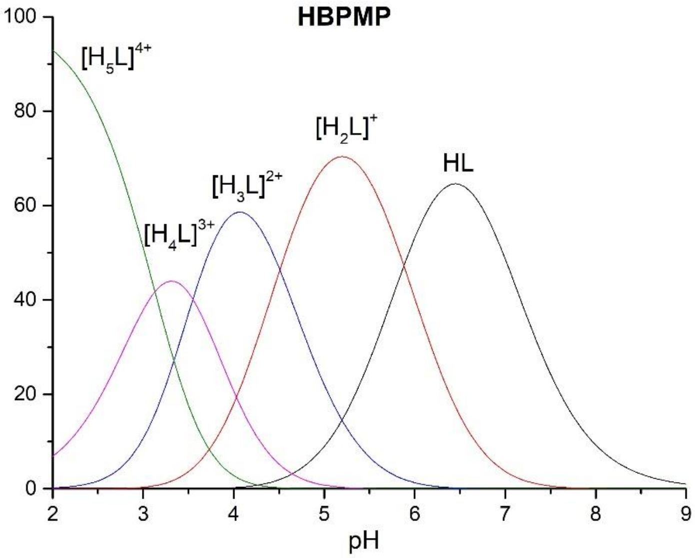

Figure 61: *Speciation curve for the ligand HBPMP. Contion: [ligands]= 0.043mM in DMSO (5%v/v)/(H_2O/HCl,KCl; starting pH=2.7).*

The trends highlight in the speciation curves is quite similar for both HL1 and for HL5 *(Figure 60*). Both ligands present high stability at pH 8, where the main species is the original ligand HL. While only a small amount is protonated at physiological pH. As regards HBPMP, the speciation curve shows that the main species at pH 7.4 is HL, while the prevailing form at pH at about 5.5 is the one with one tertiary amine protonate (*Figure 61*). In this case the potentiometric titration was carried out till pH 9, due to the precipitation of the ligand in basic environment. These data are in agreement with the pH-metrical titration describe above, in fact at about pH 8 it is possible to observe the formation of a shoulder at ~290 nm, attributable to the phenolic group (*Figure 57, Figure 58, Figure 59*).

From the potentiometric titration of solutions with the copper (II) and the ligands, with NaOH, the speciation curves of in situ-formed complexes were obtained and the acid association constants were calculated (*Table 11*, *Table 12*). For the ligands HL1 and HL5 the ratio used is 1.2:1 (ligand : copper), whereas for the HBPMP the 1:2 ratio (ligand:copper) was adopted.

Table 11*: Overall (log βi) and stepwise (log Ki) protonation constants of in situ- formed complexes with HL1 (x=1) and HL5 (x=5), obtained from potentiometric titration.*

Species	**log (β_i) x=1**	**log (β_i) x=5**	**log (K_i) x=1**	**log (K_i) x=5**
$[CuH_2Lx]^{3+}$	*23.54*	*23.16*	*5.09*	*5.42*
$[CuHLx]^{2+}$	*18.45*	*17.74*	*6.94*	*6.38*
$[CuLx]^{+}$	*11.51*	*11.36*	*9.47*	*9.12*
$[Cu(OH)Lx]$	*2.04*	*2.24*	*10.40*	*10.73*

Table 12: *Overall (log βi) and stepwise (log Ki) protonation constants of in situ-formed complex with HBPMP, obtained from potentiometric titration.*

Species	**log (β_i)**	**log (K_i)**
$[CuH_3L]^{4+}$	22.60	3.59
$[CuH_2L]^{3+}$	19.01	4.81
$[CuHL]^{2+}$	14.20	6.32
$[CuL]^{+}$	7.88	8.72
$[Cu(OH)L]$	-0.84	11.37
$[Cu(OH)_2L]^{-1}$	-12.21	0
$[Cu_2H_2L]^{5+}$	23.47	4.28
$[Cu_2HL]^{4+}$	19.19	5.44
$[Cu_2L]^{3+}$	13.75	8.38
$[Cu_2(OH)L]^{2+}$	5.37	11.07

The species considered in the final model were obtained by taking into account the total set of data resulting from the different titrations. In addition to the ligand deprotonation steps, two additional deprotonation had to be included, probably accounted for the deprotonation of water molecules bound to the copper ions.

The constants for the mononuclear complexes, presented in table *Table 11*, allow the construction of speciation curves (*Figure 62*). At pH 3.5 the predominant species is $[CuH_2L]^{3+}$ relative to the copper complex with a protonated ligand. Upon increasing the pH the formation of $[CuHL]^{2+}$ is favoured (copper complex with the original ligand). At pH 7.8, the mononuclear complexes are in the form $[CuL]^{+}$ while the species $[CuHL]^{2+}$ is 11% and 5% for HL1 and HL5, respectively. Above pH 9 the formation of the species $[Cu(OH)L]$ and $[Cu(OH)_2L]^{-}$, due to the loss of one and two protons by an external source, probably a water molecule, is observed[45].

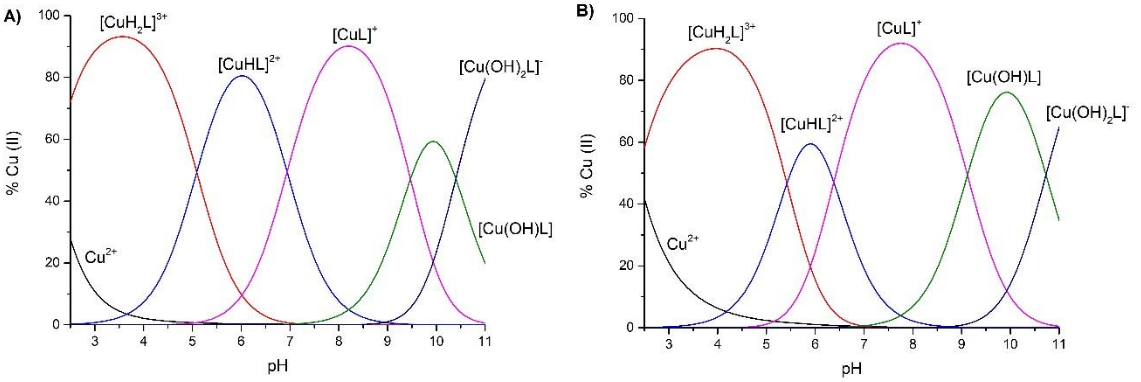

Figure 62: *Speciation curves for the situ-formed complexes ligand : copper (II) 1.2:1. A) with ligand HL1, B) with the ligand HL5. The solutions are 0.7mM in DMSO (5%v/v)/(H_2O/HCl,KCl; starting pH=2.7).*

Concerning the dinuclear complex, the speciation curve (*Figure 63*), obtained from the constants show in *Table 12* highlights a different behaviour. At pH 3.5, the prevalent species in the dinuclear one, with the protonated ligand ($[Cu_2H_2L]^{5+}$). Upon increasing the pH, the formation of $[Cu_2HL]^{4+}$ (copper complex with the original ligand) occurs. At pH 7.8 the more stable form at is $[Cu_2L]^{3+}$. Above pH 9 the formation of the species, due to the loss of one $[Cu_2(OH)L]^{2+}$ and two $[Cu_2(OH)_2L]^{+}$protons by a water molecule, is observed[45]. The mononuclear species are presented at low concentration.

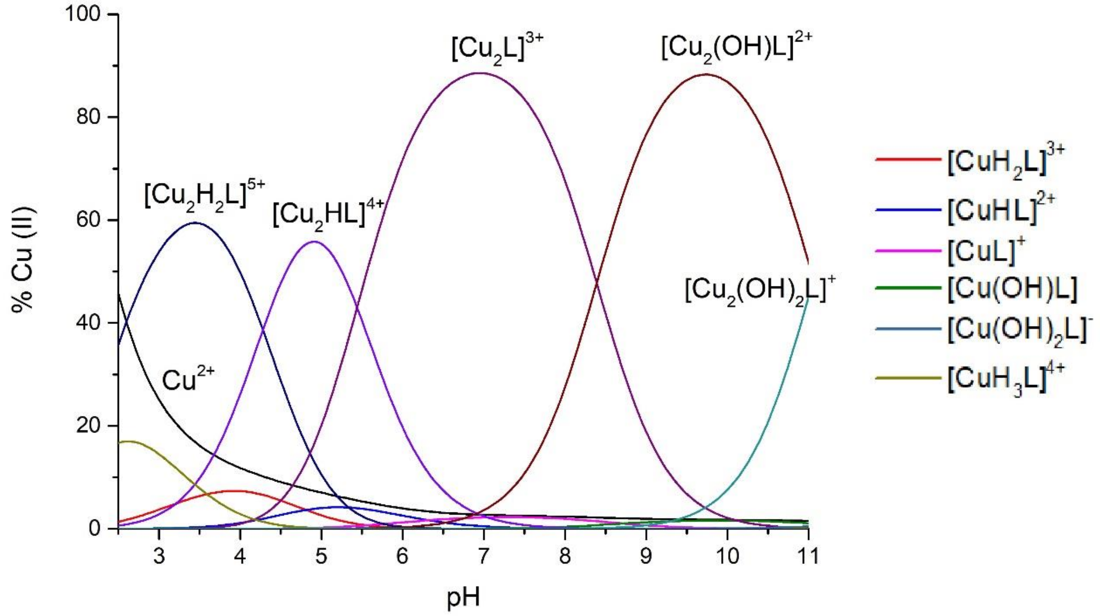

Figure 63: *Speciation curves for the situ-formed complexes ligand : copper (II) 1:2. The solution is 0.7mM in DMSO (5%v/v)/(H_2O/HCl,KCl; starting pH=2.7). In the legend the monuclear species are indicated.*

In all cases the data simulations, realized with the software Hyperquad 2008 is in agreement with the formation of mononuclear complexes for HL1 and HL5, and dinuclear complex for HBPMP.

2.4 Catalytic activity of the complexes

The antioxidant activity is the main catalytic activity of the complexes studied. In order to evaluate this propriety, their redox proprieties were initially examined. Then, the superoxide dismutase and catalase like-activities were studied, to verify their ability to work as ROS scavenging. Finally, the peroxidase activity was considered, using two models substrate.

2.4.1 Cyclic voltammetry

The challenge is to design stable metal complexes with low molecular weight, that display a suitable redox cycle for the metal ion. In fact, the copper centre has to catalyse the disproportionation of superoxide radical. At the beginning, the redox potentials of the species were evaluated through cyclic voltammetry. By means of this technique, it is possible to appraised the reduction potential of Cu^{2+}/Cu^{+}, which is an important factor in the SOD activity. The potential for the monoelectronic reduction of the superoxide anion to hydrogen peroxide is equal to 0.89 V, while the potential for the superoxide anion radical reduction is equal to - 0.16 V. Therefore, the metal ion redox potential has to lie between the potential for oxidation (-0.16 V vs. NHE) and reduction (0.89 V vs. NHE) of superoxide radicals (*Figure 64*). The copper ion must also be able to cycle between the Cu(II) and Cu(I) oxidation states faster than the rate of the spontaneous disproportionation of superoxide radical. As well the ligand has an important role, because it must have high affinity for both the reduced and oxidized state of the metal to obtain complexes that are stable under physiological conditions, in order to avoid the release of metal during the redox cycling. Finally, at least one coordination site must be available for binding of the superoxide radical, in the case of an inner-sphere SOD catalytic pathway[47].

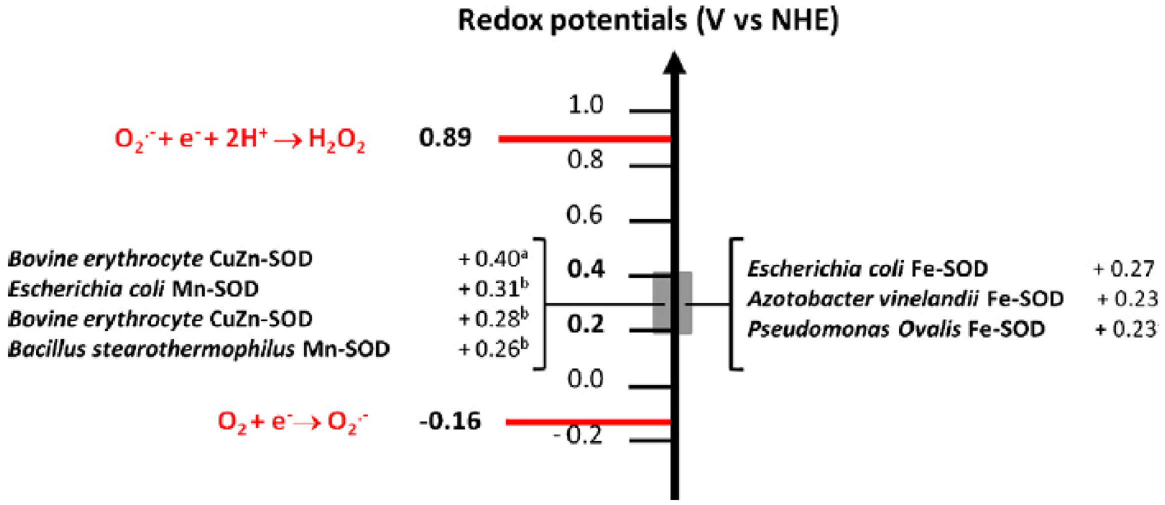

Figure 64: *Redox potentials for the reduction and oxidation of superoxide radical anion and for several natural SOD in aqueous solution at pH 7.0.The reduction potential of natural SODs is between 0.2 and 0.4V*[47]*.*

Cyclic voltammograms of the mononuclear complexes were collected at the concentration of 50 mM in a mixture of CH_3CN 5%(v/v)/H_2O (phosphate buffer 10 mM, 100 mM NaCl, pH 7.8). Concerning the dinuclear complex, the concentration of the catalyst was 0.25 mM, and the solution was made in PBS, because of the high solubility of the complex in aqueous media. The voltammogram were collected using a glassy carbon (GCE) electrode as a working electrode, a counter electrode (Pt) and a reference electrode Ag/AgCl (NaCl 3M). The measurements were carried out between 400 and -500 mV, with a scan rate equal to 50 mV/s. The voltammogram of the mononuclear complexes were also recorded at different scan rate: 100, 200, 400 and 800 mV/s. The characteristic values of the cyclic voltammogram were reported in

Table ***13****,* the potentials were referred to the NHE ($V_{NHE} = V_{Ag/AgCl} + 0.210$ V).

As regards the mononuclear complexes, it is possible to distinguish two peaks, the anodic one, relative to the oxidation (towards positive potential), and the cathodic peak of the reduction (towards negative potential). The curves shows the mono-electronic transfer with a quasi-reversible character (*Figure 65*, *Figure 66*). In fact, the values ΔE = E_{pc} - E_{pa} are all higher than 59 mV. For each complexes, the values of $E_{1/2} = \frac{E_{pc}+E_{pa}}{2}$ can be found within the limits suitable for superoxide dismutation.

Table 13: *E_{pc}, E_{pa}, $E_{1/2}$, ΔE, $|i_a/i_c|$ values obtained from the cyclic voltammograms of the complexes*

Complexes	**E_{pc} (V)**	**E_{pa} (V)**	**$E_{1/2}$ (V)**	**ΔE (V)**	**$\|i_a/i_c\|$**
$Cu(HL1)(ClO_4)_2$	-0.177	-0.092	-0.135	-0.085	0.61
$Cu(HL5)(ClO_4)_2$	-0.202	-0.096	-0.149	-0.106	0.52
$Cu_2(BPMP)(H_2O)_2(ClO_4)_3$	-	-0.127	-	-	-

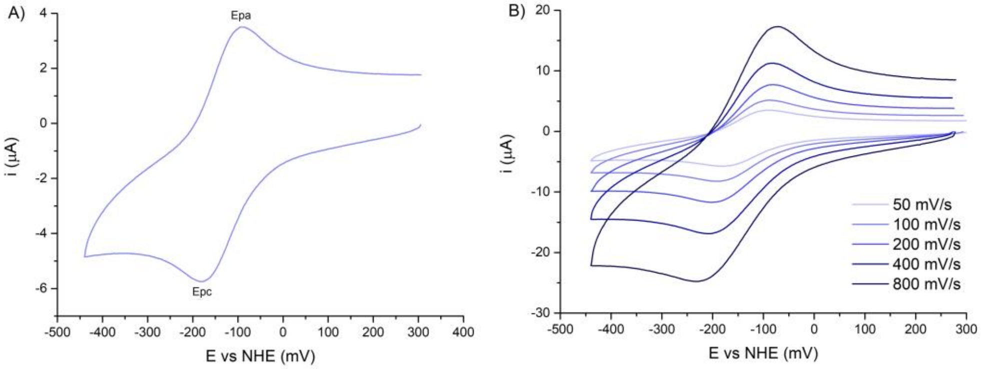

Figure 65*: Cyclic voltammograms of the complex $Cu(HL1)(ClO_4)_2$ A) recorded at scan rate 50 mV/s; B) recorded at scan rates: 50 mV/s, 100 mV/s, 200 mV/s, 400 mV/s, 800mV/s. $[Cu(HL1)(ClO_4)_2]$ = 0.50 mM, in CH_3CN 5%(v/v)/H_2O (PBS 10 mM, 100 mM NaCl, pH 7.8).*

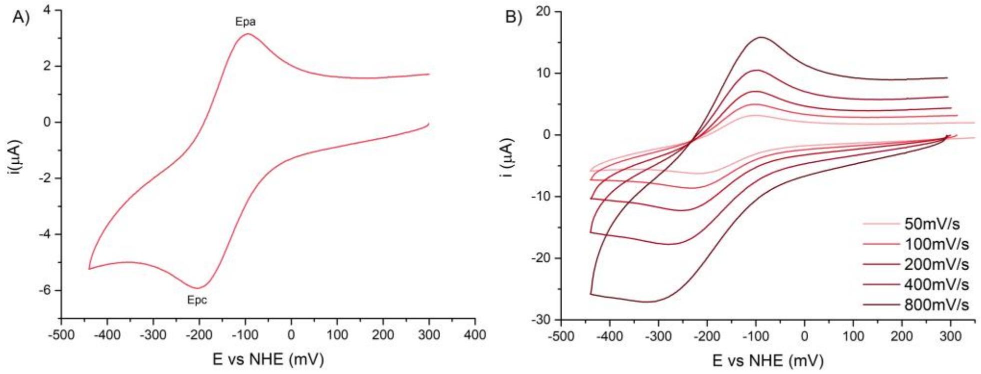

Figure 66: *Cyclic voltammograms of the complex $Cu(HL5)(ClO_4)_2$ A) recorded at scan rate 50 mV/s; B) recorded at scan rates: 50 mV/s, 100 mV/s, 200 mV/s, 400 mV/s, 800mV/s. $[Cu(HL1)(ClO_4)_2]$ = 0.50 mM, in CH_3CN 5%(v/v)/H_2O (PBS 10 mM, 100 mM NaCl, pH 7.8).*

The graph *"i_p (µA) vs* $\sqrt{v_{scan}}\,(mV/s)$" for the mononuclear complexes underlines a linear trend, as expected for a monoelectronic transfer (*Figure 67*). This is in agreement with the Randles-Sevcik law for reversible process, where the transport phenomena occur with diffusion regime. On the other hand, the ratio between the peaks currents(i_{pa}/i_{pc}) is less than one, probably due to the change in the coordination sphere of the metal centre during the electronic transfer process.

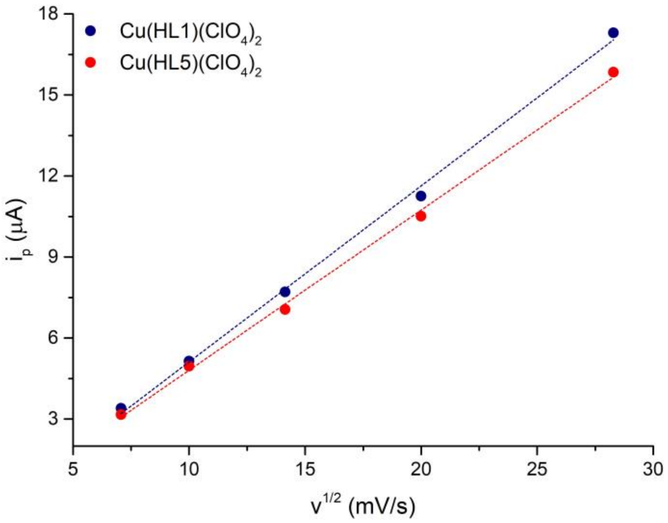

Figure 67: *graph "i_p vs $\sqrt{v_{scan}}$" obtained from the cyclic voltammograms of the complexes with HL1 (blue) and HL5 (red), recorded at the scan rates: 50,100,200,400 and 800 mV/s.*

Regarding the dinuclear complexes, the curve highlights an irreversible process. In fact, it is possible to distinguish only the anodic peak at -0.127V (Figure 68).

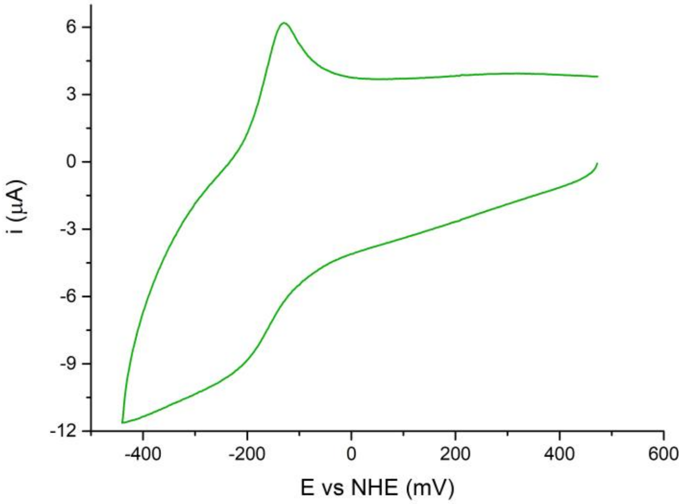

Figure 68*: Cyclic voltammogram of the complex $Cu_2(BPMP)(H_2O)_2(ClO_4)_3$ recorded at 50 mV/s. [$Cu_2(BPMP)(H_2O)_2(ClO_4)_3$] = 0.25 mM, in H_2O (PBS 10 mM, 100 mM NaCl, pH 7.8).*

The anodic and cathodic curves are attributable to the redox couple Cu(II)/Cu(I), whose reduction potential are well defined only for the mononuclear complexes with HL1 and HL5. These values are within the limit, described in *Figure 64*, hence the complexes should be able to act as antioxidant compound. However, the redox potential is not the only factor to take in account in the study of antioxidant activity, because the SOD activity depends strongly on the geometry around the copper ion[48].

To verify the absence of metallic copper on the electrode surface, due to the decomposition or release of Cu(II) during the redox process, the unpolished tests were carried out. The tests confirm the stability of the species in solution, since no residual band was observed.

2.4.2 Superoxide dismutation-like activity

In order to have good copper(II) complexes that possess SOD-like activity, the arrangements of the ligand around the copper (II) should allow the reduction to copper(I). Moreover, there should be an accessible site for the $O_2^{\bullet-}$ and hydrogen bonding sites close to the metal centre. In fact, it has been demonstrated that the hydrogen bond may promote the SOD activity[48,49].

The complexes studied seem to fulfil these requirements. First, the N_3O donor set provided by the pyridines and the tertiary amine can be considered a structural model of the His residues, while the phenol group as hydrogen bonds donor/acceptors. Furthermore, the ligands are flexible, hence they are able to accommodate the geometrical change from Cu^{2+} (square planar arrangement) to Cu^{+} (distorted tetrahedral arrangement), while the $O_2^{\bullet-}$ can easily access to the metal centre.

The superoxide dismutation activity was evaluated through the indirect method with Cytochrome C, described by McCord and Fridovich[50]. This experiment provided the catalytic constant for the dismutation of superoxide radical anion ($O_2^{\bullet-}$).

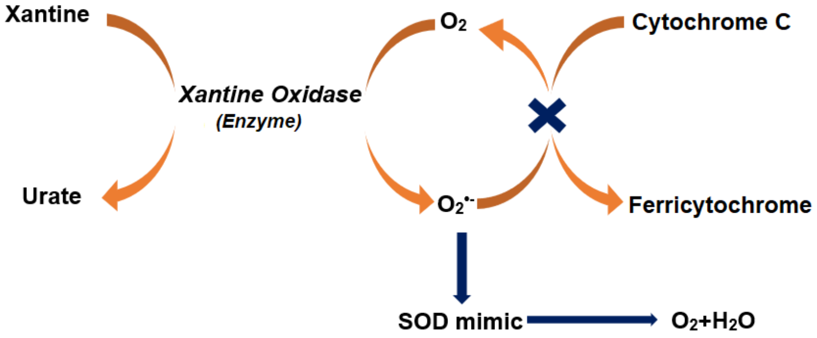

***Figure 69**: Scheme of Cytochrome C reduction to Ferricytochrome through superoxide radical anion, generated by xanthine/xantine oxidase system.*

In this specific method, superoxide radical anion is generated in a buffered solution (PBS, pH=7.8) by a xanthine/xanthine oxidase system, in the presence of cytochrome C (CytC). The xanthine is oxidized to urate by oxygen, producing the $O_2^{\bullet -}$ species, which reduces Cytochrome C to Ferricytochrome to yield molecular oxygen (*Figure 69*). A catalyst with SOD activity competes with the Cytochrome C in the scavenging of superoxide radical anion, thus inhibiting its reduction to Ferricytochrome. Since Ferricytochrome absorbs at 550 nm, the kinetics can be followed over time by UV-vis spectroscopy. What is measured with this assay is the IC_{50} value, the concentration of SOD mimic that causes 50 % of inhibition CytC reduction by superoxide radical and the catalytic constant, k_{cat}, which can be calculated from the equation 20, note the reaction constant between CytC and $O_2^{\bullet -}$ (k_{CytC} = 2.6 x10^5 $M^{-1}s^{-1}$) and IC_{50}.

$$k_{cat}\ (O_2^{\bullet -}) = \frac{k_{CytC}\ [CytC]}{IC_{50}} \quad (20)$$

Since the kinetic of the superoxide radical anion is very fast, when the xanthine oxidase is added in the system, to evaluate the SOD activity, only the first, linear part of the curve was taken into account (< 0.3 min). The curve reaches the plateau when all the Cytochrome C is converted to Ferricytochrome. The conversion is total when in the sample there is no catalyst, while it is inhibited increasing the concentration of the catalyst (*Figure 70*).

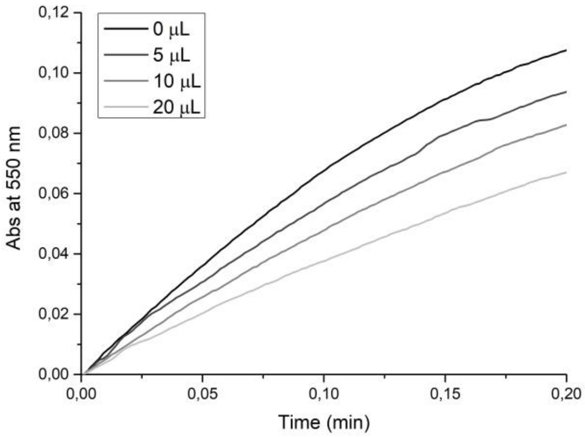

Figure 70*: Trend of the absorbance over time at 550 nm, depending on the catalyst concentration. The black line corresponds to the total conversion of Cytochrome C to Ferricytochrome. The shades of grey from the dark one to the light one are relative to increasing amount of the catalyst in the sample, with these concentration: 0.16μM, 0.32 μM, 0.65 μM.*

The range between 0 and 0.2 minutes was considered and the trend lines were calculated, from which the slope and the intercept were obtained. Each experiment was repeated as a duplicate, hence the average of the slope was calculated. From these values, the % inhibition, depending on the copper (II) concentration is obtained (***Figure 71***).

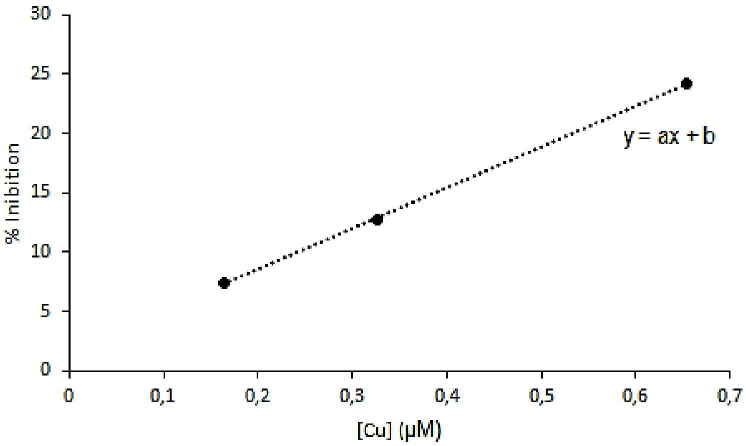

Figure 71*: graph "concentration Cu (II) vs % inhibition"*

From the slope and the intercept in the plot *"[Cu] vs % inhibition"*, through the equation 21, the IC_{50} values is calculated.

$$IC_{50} = \frac{(50-b)}{a} \quad (21)$$

The k_{cat} is obtained from the following equation, where k_{Cytc} value is known in literature:

$$k_{cat}\,(O_2^{\bullet -}) = \frac{k_{CytC}\,[CytC]}{IC_{50}} \quad (22)$$

The values obtained from the different complexes are reported in *Table 14*.

Table 14: *IC_{50} values, catalytic constant for the superoxide radical anion dismutation e its logarithmic value, obtained with the indirect method. Condition adopted: [CytC] = 10μM, [catalase] = 15μg/mL, [xantine] = 40 μM , [xanthine oxidase] = 0.0053 U/mL, phosphate buffer 50 mM pH = 7.8*

Complexes	**IC_{50} (μM)**	**k_{cat} (s^{-1})**	**log (k_{cat})**
$Cu(HL1)(ClO_4)_2$	1.41	1.83 x10^6	6.27
$Cu(HL5)(ClO_4)_2$	1.04	2.62 x10^6	6.41
$Cu_2(BPMP)(H_2O)_2(ClO_4)_3$	1.21	2.18 x10^6	6.32

The comparison with the literature values is complicated, because the IC_{50} values depends from the technique used for the analysis, while k_{cat} is independent from the sample concentration and allows a better comparison. Moreover, various drawbacks have been highlighted on the use of NBT (nitro blue tetrazolium) instead of CytC as probe of $O_2^{\bullet -}$ scavenging. However, this assay have some problems because the NBT itself can mediate the formation of superoxide radicals. It also gives rise to a less stable signals, producing less reproducible kinetics and a overestimation of the kinetic constant[47].

Comparing the data of the complexes studied with the ones presented in literature (*Table 15*), it is possible to notice that in some case the characteristic values for the SOD activity are quite similar, like for $[Cu(BPMPA)]^+$, while in other cases the data differs a lot, probably due to the different assay used in the analysis. Even if the complexes studied are less active than native Cu/Zn-SOD and other copper (II) complexes reported in literature, the dismutation of $O_2^{\bullet -}$ occurs with rate constant higher than two orders of magnitude respect to the self-dismutation constant (8 x 10^4 $M^{-1}s^{-1}$ [51]).

Interesting is to compare the dinuclear complexes, previously obtained in this laboratory, with the same ligands HL1 and HL5[44]. The dinuclear complexes with HL1 and HL5 presents higher IC_{50} values with respect to the mononuclear complexes. Hence, the mononuclear complexes have a best SOD-like activity (*Table 15*), on the other hand, this suggests that the less stable dinuclear complexes do not fully convert to the corresponding mononuclear species in aqueous mixture.

Among the complexes studied in this work, the one that presents the best SOD-like activity is $Cu(HL5)(ClO_4)_2$. Indeed, it presents the higher value for k_{cat} and the lower for IC_{50}, pointing out its highest inhibitory ability against the degradation of CytC to Ferricytochrome, therefore a greater tendency to eliminate the superoxide radical anion.

Table 15*: Summary of SOD activity express as IC_{50} and log (k_{cat}) for the native Cu-ZnSOD and copper (II) mononuclear and dinuclear complexes; the values were obtained with a) NBT assay, b) CytC assay;c) dib=[2-(4,5-dihydro-1H-imidazol-2-yl)-1Hbenzimidazole-N,N,O],d)HBPMPA=N-propanoate-N,N-bis-(2-pyridylmethyl)amine, e) TAAP = obtained by self-condensation of 5-amino-3-methyl-l-phenylpyrazole-4-carbaldehyde (AMPC) in the presence of copper(II)f) tppen= derivative of tris(2-pyridilmethyl)amine.*

Complexes	**IC_{50} (μM)**	**log (k_{cat})**	**Ref.**
Native Cu-ZnSOD	0.04^a	9.30	52,53
$Cu(SO)_4$	72.2^b	-	54
$Cu(HL1)(ClO_4)_2$	1.41^b	6.27	This work
$Cu_2(L1)_2(ClO_4)_2$	1.99^b	6.13	44
$Cu(HL5)(ClO_4)_2$	1.04^b	6.41	This work
$Cu_2(L5)_2(ClO_4)_2$	1.28^b	6.31	44
$Cu(dib)Cl_2\ ^c$	0.09^a	-	55
$[Cu(BPMPA)]^{+d}$	1.04^b	7.09	35
$Cu(TAAP)(NO_3)_2^e$	0.55^a	7.26	49
$Cu_2(BPMP)(H_2O)_2(ClO_4)_3$	1.21^b	6.32	This work
$Cu_2(tppen)Cl_4\ ^f$	0.54^b	-	56

2.4.3 Hydrogen peroxide dismutation: catalase-like activity

Catalases efficiently disproportionate H_2O_2 to water and O_2 , with k_{cat}/K_M 10^6–$10^7 M^{-1}s^{-1}$, without consuming additional electron-donor substrates[57]. Among synthetic analogues, complexes based on manganese show high activity. However, in the literature copper complexes with catalase activity are also presented.

The mechanism proposed for the disproportionation of H_2O_2 for mononuclear copper complexes is proposed by *Ramadan et al*[49]. The reactions involve redox cycling of metal ion as follows:

$$M^{n+} + H_2O_2 \longrightarrow M^{(n-1)} + HOO\bullet + H^+ \quad (23)$$

$$M^{(n-1)} + HOO\bullet + H^+ + H_2O_2 \longrightarrow M^{n+} + 2H_2O + O_2 \quad (24)$$

As regards the dinuclear copper complexes the mechanism, proposed by *Gao et al*[58] is shown in *Figure 72*.

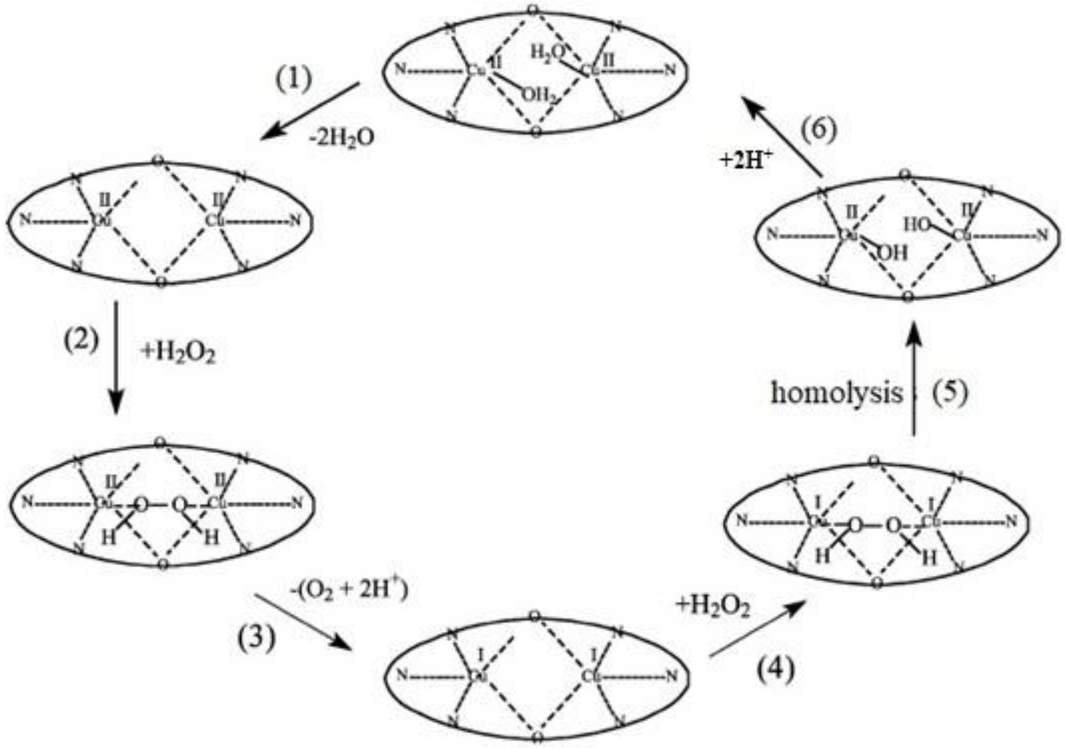

***Figure 72**: Mechanism of hydrogen peroxide dismutation, proposed by Gao et al[58].*

The first step allows to the two Cu (II) to bind to a molecule of hydrogen peroxide(stage 2). The hydrogen peroxide molecule promotes the reduction of metal centres from Cu (II) to Cu (I), with the release of an oxygen molecule (stage 3). A second molecule of hydrogen peroxide is bridged between the metal centres (stage 4) and after the homolysis of the peroxo bond (stage 5), two protons are added (stage 6) and two molecules of water are realised, obtaining the starting complex (stage 1). The presence of two metal ions allows the coordination of H_2O_2 and facilitate the bi-electronic oxidation and reduction processes.

The studied complexes catalase-like ability was evaluated by monitoring the pressure developed by the oxygen resulting from the dismutation of the hydrogen peroxide over a period of about 22 hours. For the analysis, a borate-based buffer was used (BBS 50 mM pH 7.8), in order to avoid competitive coordination by phosphates.

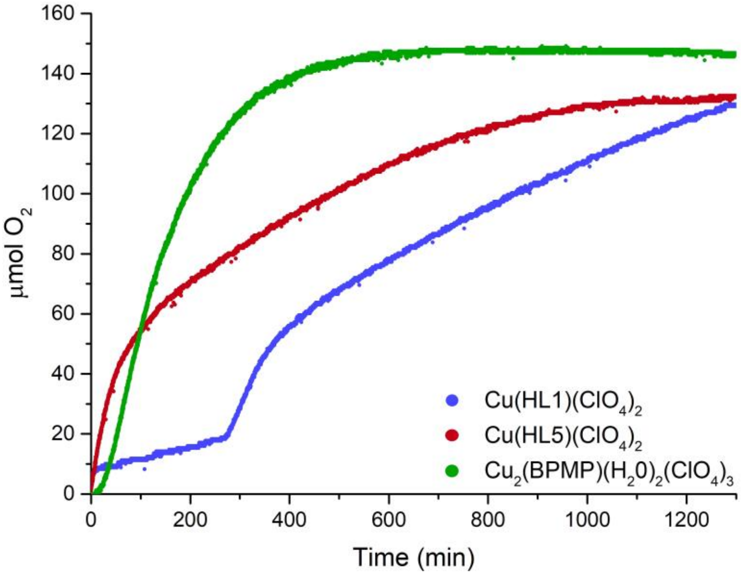

***Figure 73**: O_2 production over time, generated from the hydrogen peroxide dismutation. The trends obtained fort the preformed complexes with HL1 (blue), HL5 (red), HBPMP (green) are the result of the average of three measurements.*

Examining the graph *"μmol O_2 vs Time" (Figure 73)*, in which the μmol were obtained through the application of the law of *"Perfect Gases"* (equation 25), it is possible to note very different behaviour for the various catalysts.

$$\mu mol\ (O_2) = \frac{(\Delta p \cdot V)}{(R \cdot T)} \cdot 1000000\ (25)$$

where Δp = pressure variation

V= gas volume = head volume= 0.0146 L

R = 0.0831 (atm·L)/(mol·K)

T = 298 K

In particular, the mononuclear complex with the ligand HL1 presents an induction time before it starts its activity, probably due to the reorganization around the copper centre before it starts an efficient conversion of hydrogen peroxide. Also the dinuclear complexes with HBPMP exhibits a short induction time. Instead, the complex with HL5 immediately induces the dismutation of hydrogen peroxide.

The maximum rate conversion (R_0), the number of turnover (TON) and the frequency of turnover (TOF) are the characteristic parameters of catalysts classification and are reported in *Table 16*.

Table 16: *Average values, obtained from triplicate experiments, of R_0, TON, TOF, %O_2 and umol of O_2 generated after about 22 hours. Condition: [catalyst]= 200 μM,[H_2O_2]=30 mM in BBS 50 mM pH=7.8. a) data obtained from previous study in the same condition described in this work[44].*

Complexes	Induction time (min)	R_0 (μmol/min)	TOF (min^{-1}-h^{-1})	Time (min)	TON	O_2 (μmol)
$Cu(HL1)(ClO_4)_2$	300	0.34	0.14-8.49	1750	59	141.3
$Cu(HL5)(ClO_4)_2$	-	0.52	0.21-13.07	1400	55	131.6
$Cu_2(BPMP)(H_2O)_2(ClO_4)_3$	70	0.67	0.28-16.71	600	62	147.7
$Cu_2(L1)(ClO_4)_2$ [a]	200	0.74	0.31-18.55	800	58	-
$Cu_2(L5)(ClO_4)_2$ [a]	-	0.35	0.15-8.72	800	46	-

The value of R_0 corresponds to the maximum slope of the curve, below a conversion percentage of 30%, where an approximately linear trend is followed, and it is expressed in μmol / min. The value of TON is the ratio between the moles of oxygen developed and those of catalyst, while the TOF is the ratio between R_0 and the moles of catalyst, and it is expressed in min^{-1}. The best activity is showed by the dinuclear complex with HBPMP: in fact, it exhibits a relative high value for R_0, and the highest value for TON and umol of O_2. Comparing the mononuclear compounds studied with the dinuclear ones, analysed in a previous work[44], some differences are presented. As regard the ligand HL1 the values of TON are quite similar, while R_0 differs a lot. With regard to the ligand HL5, however, both the TON and R_0 values are higher than the dinuclear complex. The important factor to take in account is that the catalase studies for the dinuclear complexes with HL1 and HL5 were carried out over a period of about 12 h[44]. While the mononuclear complexes reach the maximum O_2 production over a double period (about 22h). This is in agreement with the hypothesis that the dinuclear complexes in solution act as the mononuclear ones, so that the amount of active species is twice than the mononuclear ones.

To clarify the nature of the mechanism, and to exclude the presence of Fenton type reactions in the dismutation of the hydrogen peroxide effected by the complex, the catalase experiments were carried out in presence of KBr, a radical scavenger of HO•. The studied was led for the mononuclear complexes with HL1 and HL5 and pointed out that in the presence of KBr, the micromoles of oxygen production increases (*Figure 74*). In particular, the KBr addition, in the case of the mononuclear complex with HL1 removes the induction time and this allows to reach the plateau in O_2 production in a shorter time (400 min). Concerning the $Cu(HL5)(ClO_4)_2$ complex, the presence of KBr increases the production of O_2, which reaches its maximum in about 300 minutes. Therefore, the addition of KBr, as a radical scavenger makes the reaction even more efficient (*Table 17*).

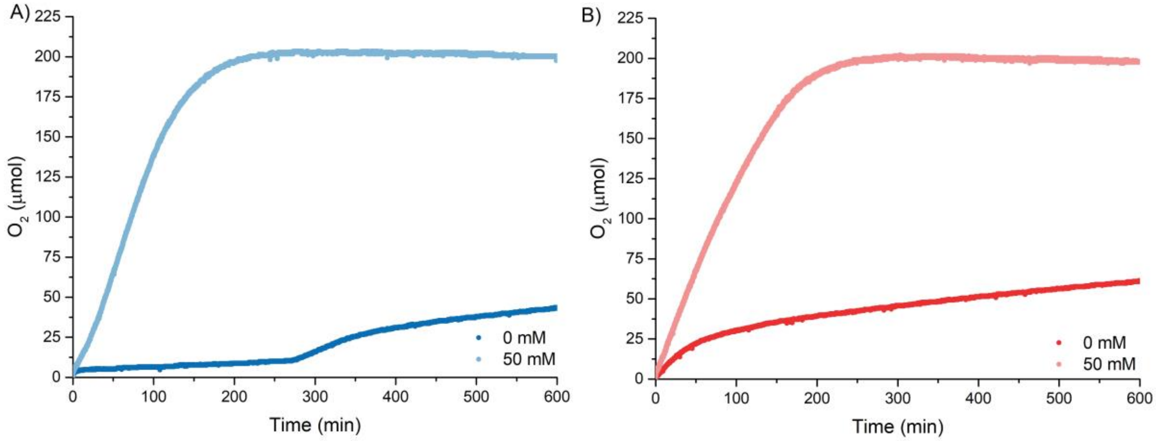

***Figure 74*:** *O_2 production over time, generated from the hydrogen peroxide dismutation. A) trend obtained for preformed complexes with HL1 (blue) and in presence of 50mM KBr (light blue); B) trend obtained for the preformed complex with HL5 (red) an in presence of 50mM KBr (light red).*

***Table 17*:** *Comparison between the data obtained without and in presence of KBr. Conditions: [catalyst]= 200 µM,[H_2O_2]=30 mM in BBS 50 mM pH=7.8.*

Complexes	**[KBr] (mM)**	**R_0 (µmol/min)**	**TON**	**O_2 (µmol)**
Cu(HL1)(ClO_4)$_2$	0	0.34	59	141.3
Cu(HL5)(ClO_4)$_2$	0	0.52	55	131.6
Cu(HL1)(ClO_4)$_2$	50	1.47	85	203.4
Cu(HL5)(ClO_4)$_2$	50	1.26	84	201.6

The catalytic process was also followed by UV-Vis spectroscopy, in order to obtain information about the molecular events that take place during the dismutation of hydrogen peroxide. The UV-Vis spectra were recorded at regular time intervals, according to the kinetic observed with the previous experiments. The spectra collected point out a variation in the shape of the absorption bands, with loss of some spectral characteristics. This indicates that the complex undergo degradation during the dismutation of the hydrogen peroxide, with major changes occurring after the induction time.

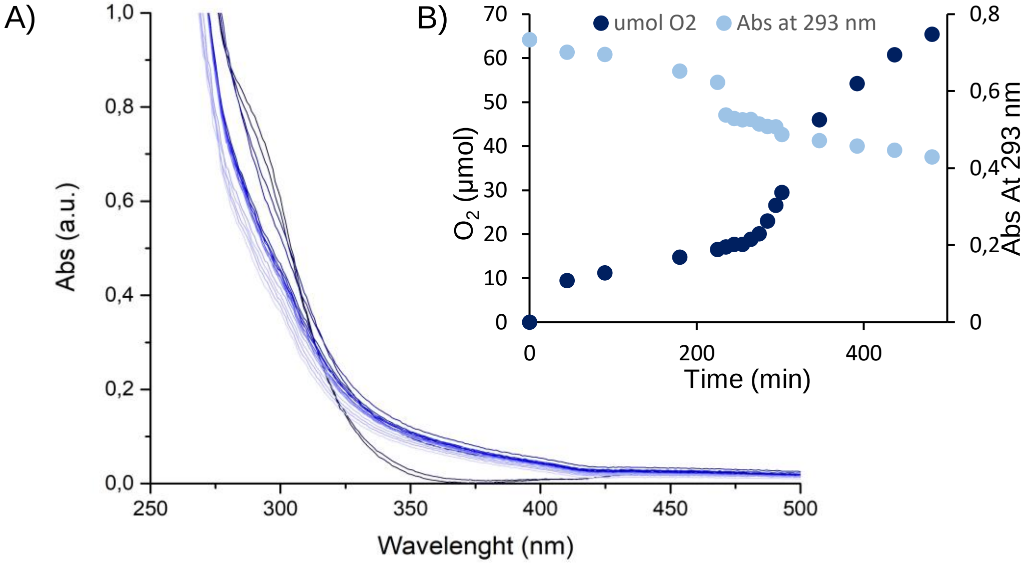

***Figure 75**: A) Cu(HL1)(ClO_4)$_2$ UV-vis spectra at t=0 (blue) and after 8 h (light blue). The colours variation represents an increment of 45 min from t=0 to t=225 min, of 10 min from t=225 to t= 305 min and 45 min from t= 305 to t=485 min. B) Conditions: [Cu(HL1)(ClO_4)$_2$]= 200 µM, [H_2O_2]=10mM in BBS 50 mM pH=7.8. B) O_2 (blue) and Abs (light blue) trend at 293 nm over time.*

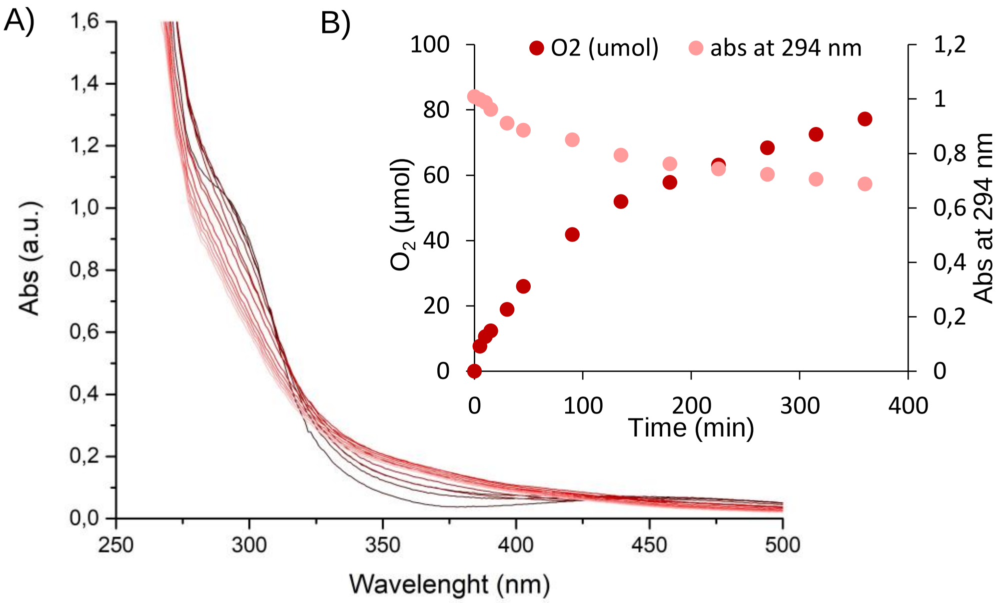

***Figure 76:** A) Cu(HL5)(ClO_4)$_2$ UV-vis spectra at t=0 (red) and after 7 h (light red). The colours variation represents an increment of 5 min from t=0 to t=15 min, of 15 min from t=15 to t= 45 min and 45 min from t= 45 to t=360 min. Conditions: [Cu(HL5)(ClO_4)$_2$]= 200 uM, [H_2O_2]=10mM in BBS 50mM pH=7.8. B) O_2 (red) and Abs (light red) trend at 294 nm over time.*

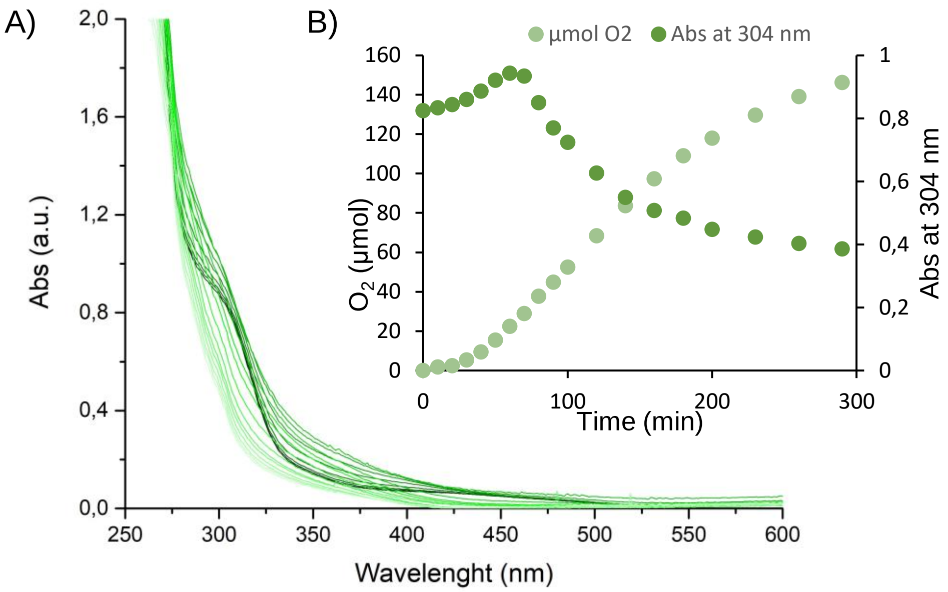

Figure 77: : *A) $Cu_2(BPMP)(H_2O)_2(ClO_4)_3$ UV-vis spectra at t=0 (green) and after 6 h (light green). The colours variation represents an increment of 10 min. Condition: $[Cu_2(BPMP)(H_2O)_2(ClO_4)_3]$= 200 uM, $[H_2O_2]$=10mM in BBS 50mM pH=7.8. B) O_2 (green) and Abs (light green) trend at 304 nm over time.*

For the complex with HL1 the mutation of the band occurs in a longer time, due to the induction time previously observed (*Figure 75*). The absorbance relative to the π→π* transition gradually decreases, and simultaneously the production of molecular oxygen increases. This behaviour suggests a reorganization in the coordination sphere of the complex, required to start the reaction. The characteristic band disappears after 4 hours. On the other hand, the spectra of the complexes, $Cu(HL5)(ClO_4)_2$ and $Cu_2(BPMP)(H_2O)_2(ClO_4)_3$ undergo a faster modification (*Figure 76 and Figure 77*). The band π→π* disappears after about 60 minutes, therefore the stability of these complexes is lower than that of the mononuclear one with HL1. As a matter of fact, the R_0 values for these complexes are higher than the one obtained for $Cu(HL1)(ClO_4)_2$. After 7 hours the active species degrade and the O_2 production increase. Interesting is the behaviour of the $Cu_2(BPMP)(H_2O)_2(ClO_4)_3$, where the Abs at 304 nm increases till 100 min, then decrease and at the same time the production of O_2 increases (*Figure 77*). The trend could be attributed to the formation of a different active specie that catalyse the dismutation of hydrogen peroxide.

The evolution of mononuclear complexes during the catalase activity was also evaluated by ESI-MS (+), monitoring the relative intensity of the molecular peak.

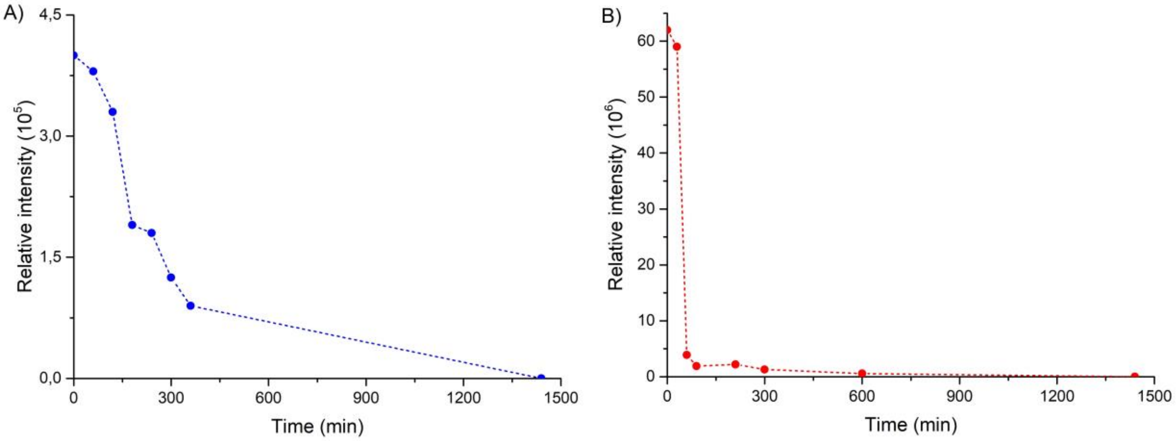

Figure 78: *A) trend for the ion [CuL1]$^+$ (m/z 367.1) relative to the complex Cu(HL1)(ClO_4)$_2$, the data were collected from t=0 to t=24h, each 60 minutes; B) trend for the ion [CuL5]$^+$ (m/z 397.1) of the complex Cu(HL5)(ClO_4)$_2$, the data were collected from t=0 to t=24h, each 30 minutes. Conditions: [complex]= 50μM, [H_2O_2]= 7.5mM in BBS 25 mM pH = 7.8.*

The graphs in *Figure 78* confirm what is observed in the catalase experiments and in the UV-vis studies. The induction time, characteristic of the mononuclear complex with HL1 is related to a slow decomposition of the initial species, before completely disappearing after 24 hours. On the other hand, the complex with HL5 is converted almost completely after 60 minutes, disappearing at 24 hours.

In the active species degradation, it is also important to take into account a mechanism, where the hydrogen peroxide could cause the oxidative degradation of the ligands, as discussed below. On the other hand, as highlighted by the experiments with KBr, radicalic species can contribute to ligand degradation in the observed time.

2.4.4 Peroxidase-like activity

After measuring the antioxidant activity of the complexes, the pro-oxidant capabilities should also be checked. In fact, the antioxidant studies were carried out in the absence of oxidizable substrates. Therefore, it becomes important to verify the oxidation of organic substrates, including different biological targets. The peroxidase activity involves the activation of H_2O_2 in order to convert it in strongly oxidizing peroxidic or radical species. The pro-oxidant activity of the obtained metal complexes can also occur through different mechanisms, including the activation of

Fenton type radical reactions. The peroxidase activity was evaluated by UV-Vis spectroscopy, monitoring over time the absorbance variation of different substrates undergoing the oxidation. We used two different types of substrate: the morin and the o-phenylenediamine (OPD).

The oxidative degradation of the morin takes place with a radical mechanism (*Figure 79*). Observing the UV-Vis spectra, it is possible to notice a decrease in the absorbance of the characteristic band of morin, at 390 nm and the contemporaneous increment at 330 nm, relative to the products formation (*Figure 81*, A).

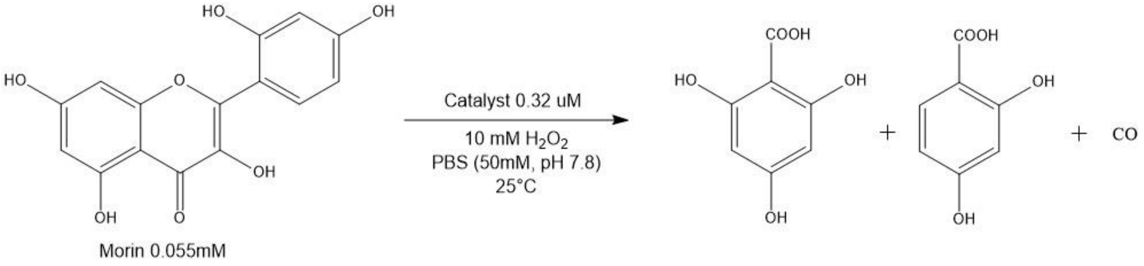

Figure 79: *Oxidative degradation of morin and the conditions used in the experiment.*

As well as the oxidation of OPD, colourless and non-fluorescent, takes place with a radical mechanism to produce 2,3 diaminophenazine (DAP), a fluorescent chromophore (*Figure 80*). In this case, the variation of the absorption due to the formation of the product is monitored. The spectrum shows an increase in the DAP band at 418 nm and a decrease in the one relating to the OPD at 220 nm (*Figure 81*, B).

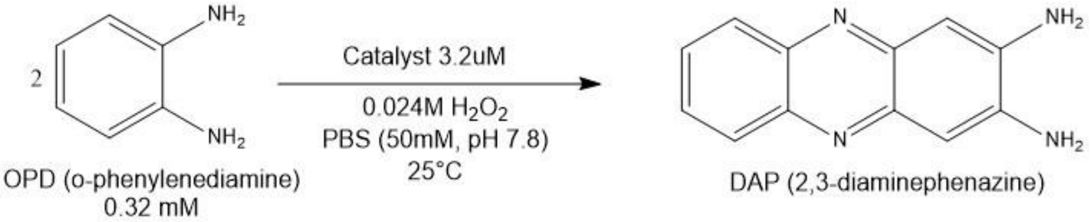

Figure 80: *Oxidative degradation of OPD and the conditions used in the experiment.*

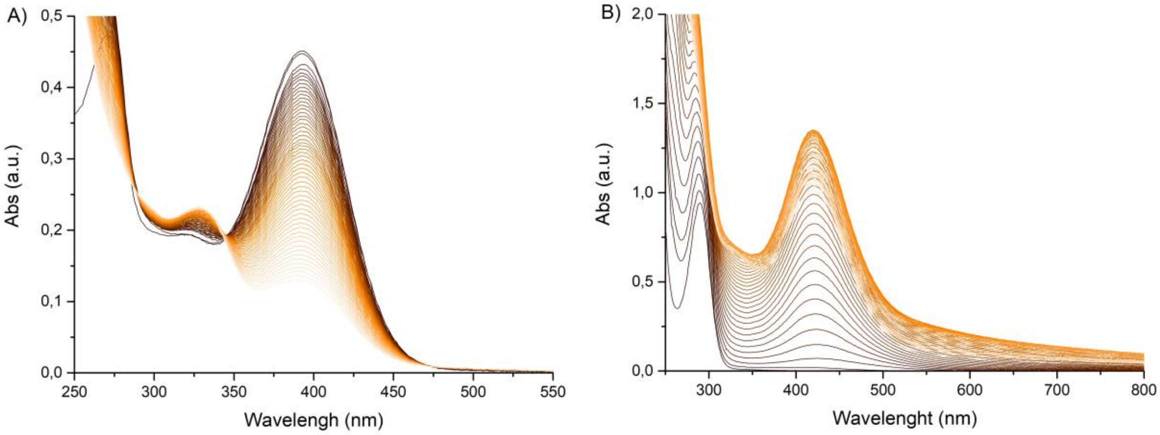

Figure 81: *Absorbance trend over time (18h) in the test with morin (A) and OPD (B), in the presence of the preformed complex Cu(HL1)(ClO_4)$_2$. The trend for the other complexes are reported in Figure 82 and 83.*

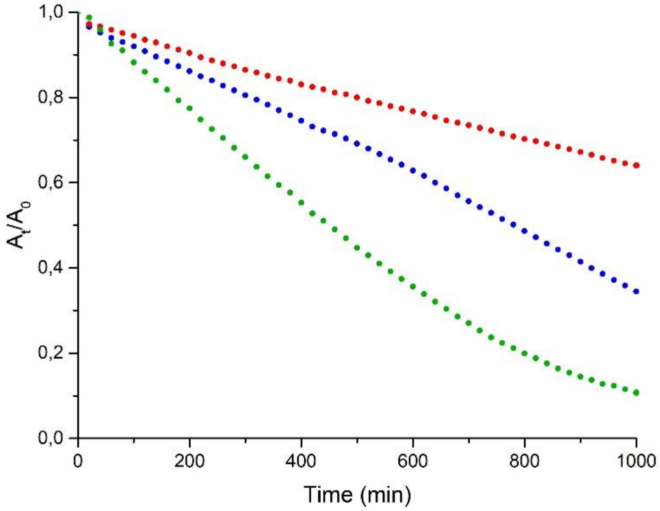

Figure 82: *Trend over time of the relative absorbance at maximum absorption of morin at 390 nm , with Cu(HL1)(ClO_4)$_2$ (blue), Cu(HL5)(ClO_4)$_2$ (red) and Cu_2(BPMP)(H_2O)$_2$(ClO_4)$_3$ (green).*

The graphs *"Abs vs time"* highlight that the complex with the highest peroxidase-like activity is the dinuclear one (*Figure 82*, *Figure 83*). Indeed, it presents the highest pro-oxidant capability with both substrates. In the *Figure 83*, it is possible to notice that for all the three complexes analysed, the absorbance, relative to the formation of the product DAP decreases, starting from about 7 hours, likely due to the overoxidation of OPD oxidation product.

In conclusion, all complexes studied present both antioxidant and oxidizing activity. This behaviour is particular evident for the dinuclear complex, which shows the best

CAT-like activity, but also the higher pro-oxidant capability. Due to the poor stability of the complexes under oxidising conditions, ascribed to the involvement of radicalic species, this behaviour is still difficult to rationalize in terms of mechanistic events.

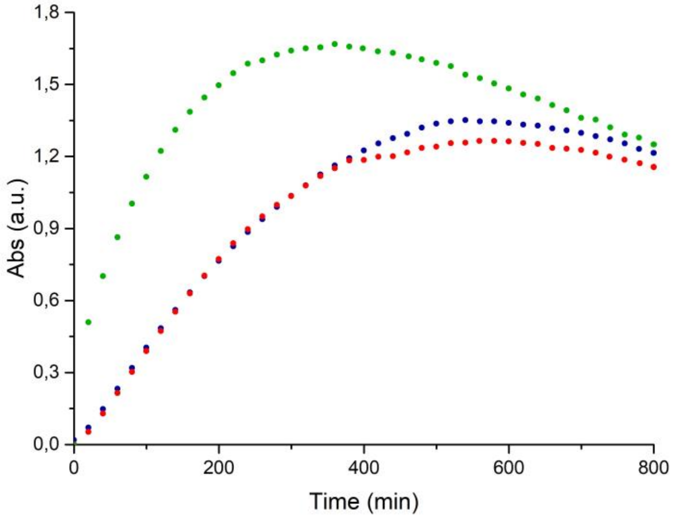

Figure 83: *Trend over time at maximum absorption of DAP at 418 nm , with Cu(HL1)(ClO_4)$_2$ (blue), Cu(HL5)(ClO_4)$_2$ (red) and Cu_2(BPMP)(H_2O)$_2$(ClO_4)$_3$ (green).*

2.5 Antiaggregation proprieties

The neurodegenerative disorders are associated to a dysfunction in the metabolism of metal ions. In fact, the metal ions are involved in Alzheimer's disease (AD), due to their ability to induce the aggregation of amyloidogenic peptide and to the production of Reactive Oxygen Species (ROS). The amyloid plaques are a hallmark in the brain of Alzheimer's disease victims. These plaques consists mainly of an aggregated peptide dubbed amyloid-β (Aβ), which in healthy brains is present in soluble form. The formation of amyloid plaques is a peculiar phenomenon in AD patients, hence the processes that cause the transformation of the soluble Aβ into plaques are key events[59]. Another important characteristic of AD is the presence of oxidative damage on neuronal lipids and proteins. This is a clearly evidence of a link between oxidative stress and the development of disease. The copper ions are accumulated in amyloid plaques, where they bind to Aβ. These complexes are able to catalyse the production of the ROS[60].

The amyloid peptides in buffer, at physiological condition are in a random coil organization, while in membrane mimicking media the structure is mainly in α-helical. The aggregation process involves the transformation in the cross β-sheet structure. In order to inhibit the aggregation promoted by the metal ions, the challenge is to design molecules that mimic the coordination site of Aβ peptides for metal ions, as in the case of metal chelators. Whereas the hydrophobic interactions can be inhibited by the *β-sheet breaker*, which have high affinity for the central hydrophobic sequence, KLVFF, of the peptide.

In N-terminal moiety of Aβ is located the high affinity binding sites for Cu(II). At physiological condition, the coordination sphere for Cu(II) is characterized by four equatorial ligands: NH_2 of Asp1, the C=O of the peptide bond between Asp1 and Ala2, N atoms of the imidazole ring of His6 and His13/14 (in equilibrium in a 1:1 ratio) (*Figure 84*)[60].

Human Aβ42: DAEFRHDSGY^{10}EVHHQKLVFF^{20}AEDVGSNKGA^{30}IIGLMVGGVV^{40}IA

Human Aβ40: DAEFRHDSGY^{10}EVHHQKLVFF^{20}AEDVGSNKGA^{30}IIGLMVGGVV^{40}

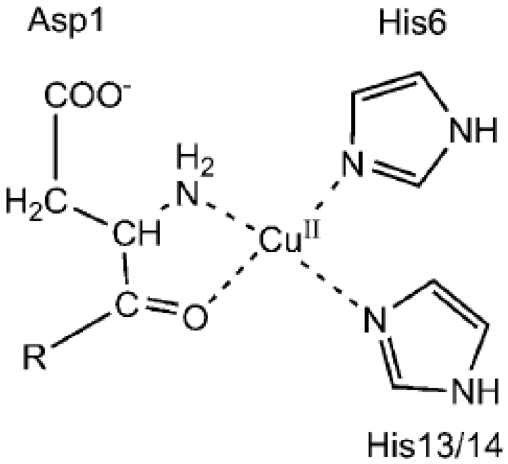

***Figure 84**: Aminoacid sequence for amyloid peptides 1-40 and 1-42 (top) and coordination site of amyloid peptides for Cu (II) ion (bottom).*

The Aβ40 peptides are used for the aggregation tests, because of their higher solubility and slower aggregation. Even if they are less toxic than Aβ42, these proprieties allow a deeper studied with different techniques. The aggregation experiments were carried out through the Tht fluorescence assay (Thioflavin T). Tht aggregates to the generated structures, inducing an increase in fluorescence. First, the amyloid peptides were dissolved in 1,1,1,3,3,3-Hexafluoro-2-propanol, a solvent that can promote the unfolding. After, the peptide solution 0.2 mM in PBS 10 mM (NaCl 100 mM, pH=7.4) was prepared. To the solution, Tht 0.2 mM, prepared in the same buffer was added and the solutions 0.2 mM of copper, ligands and preformed complexes were prepared in methanol (*Experimental section, chapter 4.6*). When the inhibition process relative to the aggregation of peptides occurs, the fluorescence increase less that the reference (Tht+P).

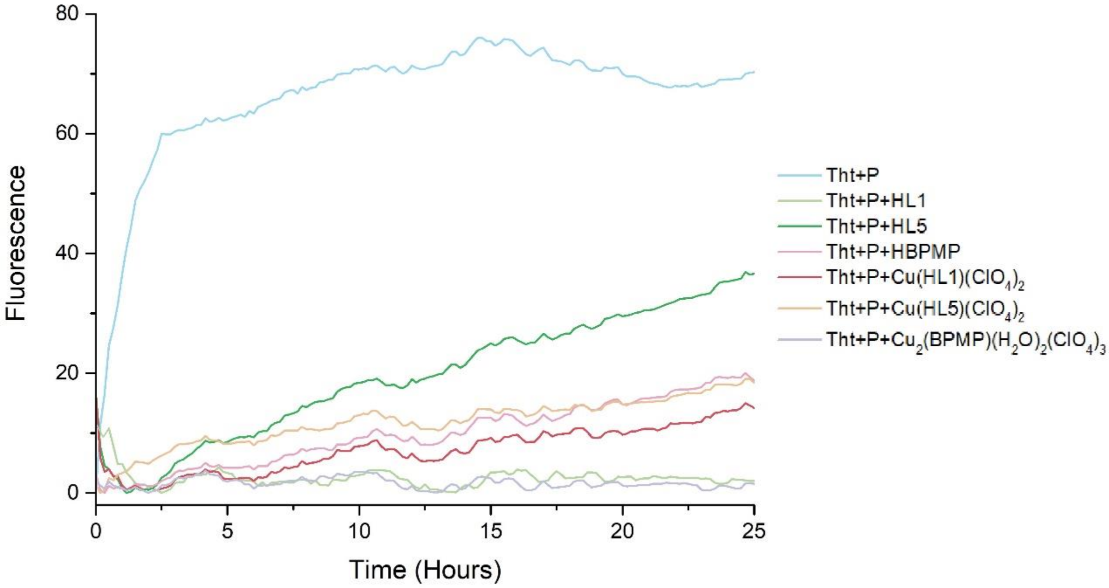

***Figure 85**: Tht fluorescence in the sample solutions listed in the legend, where P = amyloid peptide. [ThT] = 10 μM; [P] = 10 μM; solutions of complexes, binders at concentration 10 μM.*

The test showed that the presence of Cu (II) ions creates a strong interference in the measurement, therefore it was not possible to include the relative data. As regards the behaviour of the free ligands, they inhibit the aggregation in this order HL1>HBPMP>HL5. Probably, the simple and more hydrophobic structure of the ligand HL1 could interact better with the peptides, preventing the aggregation. The respective preformed complexes show a different behaviour. The preformed dinuclear complex presents the best antiaggregating activity, followed by the mononuclear complex with HL1 and HL5. In the case of HBPMP, the preformed complex inhibits better the aggregation with respect to the free ligand. Concerning the preformed mononuclear complexes, HL1 exhibits a lower fluorescence than HL5, hence a better activity. However, the ligand HL1 presents the best antiaggregating activity with respect to the preformed complex. For HL5 the behaviour is the opposite, in fact, the complex exhibits the best antiaggregating activity with respect to the ligand (*Figure 85*).

However, other techniques, like the transmission electron microscopy (TEM) should be taken into account, in order to confirm these studies also at longer incubation time.

3. Conclusions

The purpose of this work is to synthesize and characterize, from both the solution and the solid state point of view, mononuclear and dinuclear copper(II) complexes, stabilized by an N_3O-donor ligand set, in order to verify their combined superoxide dismutase and catalase-like activity in aqueous media, under physiological-like condition. The challenge is to evaluate the possible use of these complexes, within an innovative multivalent approach for AD treatment. In order to establish the multivalence of these complexes, different experiments were carried out (*Table 18*):

1. The titration of the ligands with Cu(II) solution, monitored by UV-vis spectroscopy, allowed to assess their potential as copper chelators, by determining the stoichiometry and binding constants of *in situ*-formed complexes.
2. To better understand the solution equilibria of *in situ*-formed complexes, the pH-metrical titrations were performed and monitored by UV-vis spectroscopy.
3. Potentiometric titrations of ligands and complexes were collected to obtain the protonation constants and the speciation curves, as pH function, of the different species. At physiological-like conditions (pH=7.8), as regard the ligand HL1 and HL5 the formation of mononuclear complex $[CuHL]^{2+}$ is confirmed, while for HBPMP the dinuclear complex $[Cu_2L]^{3+}$ is formed.
4. Redox potential and proprieties of the Cu(II)/Cu(I) couple for the preformed complexes, was evaluated through cyclic voltammetry. The cyclic voltammograms for $Cu(HL1)(ClO_4)_2$ and $Cu(HL5)(ClO_4)_2$ are characterized by a quasi-reversible trend and the redox potential for Cu^{2+}/Cu^{+} is situated within the range suitable for the superoxide radical anion dismutation. On the other hand the dinuclear complexes with HBPMP presents an irreversible redox behaviour, but the SOD activity is not precluded. Likely due to a favourable geometry around the copper ions.
5. SOD-like activity was evaluated through the indirect method of CytC, monitoring by UV-vis spectroscopy the kinetic of CytC reduction to Ferricytochrome. The IC_{50} [μM] and k_{cat} [s^{-1}] for the preformed complexes

were obtained. The best activity is shown by Cu(HL5)$(ClO_4)_2$, which is characterized by the lower value of IC_{50} (1.04 μM) and the highest one for k_{cat} (2.62 $x10^6$ s^{-1}).

6. The CAT-like activity was verified by monitoring the pressure generated by the molecular oxygen, during the dismutation of hydrogen peroxide. In this case, the dinuclear complex with HBPMP presents the best activity among the complexes studied. To better understand the events that occur during the catalytic process, the catalase experiment was also monitored by UV-vis for all the three complexes, and by ESI-MS (+) for the mononuclear complexes.
7. Peroxidase-like activity, evaluated by UV-Vis spectroscopy, monitoring over time the absorbance variation of the bands relative to the substrate (morin test) or the oxidation product (OP test). In a timeframe comparable to the one used for the catalase-like experiments, all the complexes studied, present a pro-oxidant activity, which is particularly high for the dinuclear complex.
8. Aggregation test, in presence of 1-40 Aβ amyloids, monitoring the fluorescence of ThT over a period of about 25 hours. From this test emerged that, concerning the ligands, the best activity is presented by HL1, while for the preformed complex Cu_2(BPMP)$(H_2O)_2(ClO_4)_3$ acts as the best antiaggregation agent.

In summary, the results obtained highlight that the complexes studied act as antioxidant and antiaggregation agents. Concerning the antioxidant activity of the mononuclear compounds, the complex Cu(HL5)$(ClO_4)_2$ displays the highest reactivity, both as SOD and as CAT mimetic system, with higher reactivity and no induction time. Despite its unfavourable negative redox potential, due to the presence of the electron donor group, the higher reactivity is likely ascribed to a more favourable geometry as well as to an easier rearrangement of the pre-catalyst to the active species. On the other hand, the more negative redox also affects the peroxidase-like activity, indeed Cu(HL5)$(ClO_4)_2$ presents the lowest tendency to act as oxidant.

As regards Cu_2(BPMP)$(H_2O)_2(ClO_4)_3$, this complex exhibits the highest CAT-like activity. However, its peroxidase-like activity is also more pronounced. In fact, in a period of time compared with the catalase activity, all the complexes exhibits also a pro-oxidant capability, resulting from parallel activation mechanisms including radicalic pathways.

Concerning the antiaggregation proprieties, these are promising in all cases, being more evident for the ligand HL1 and the complex $Cu_2(BPMP)(H_2O)_2(ClO_4)_3$. Test *in vitro* are thus advisable, so to establish how all these observations may impart an overall cytoprotective effects.

Future experiments will focus on the improvement of ligands design, in order (i) to increase the solubility of the complexes in physiological-like condition, (ii) to tune the redox proprieties of copper sites and (iii) to improve the stability under oxidative conditions. These goals could be achieved, for example, through the introduction of solubilizing tails, further hydrogen bond donors to assist substrate binding and activation, further substituents that could modulate the redox proprieties of copper centres.

Table 18: *Summary of the results obtained for each ligands*

	HL1	***HL5***	***HBPMP***
Ligand structure	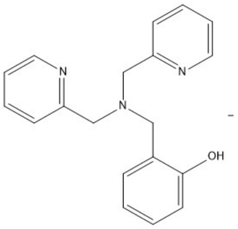	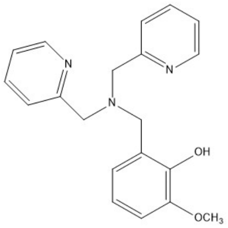	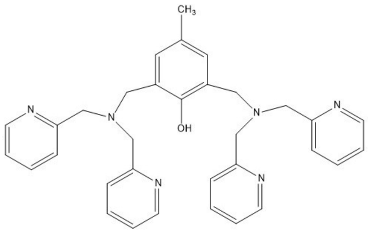
Complex Structure	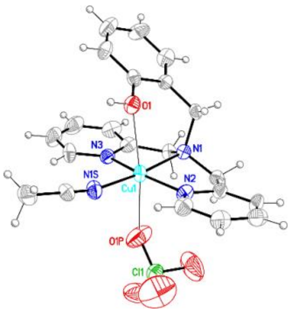	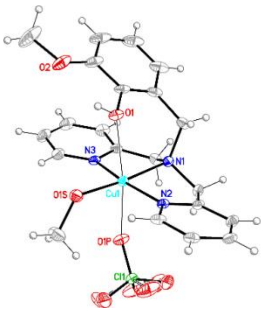	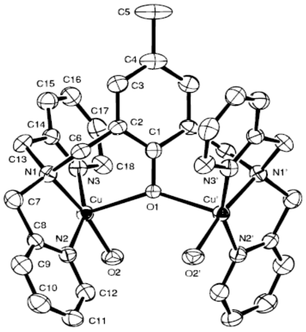
Metals centres	*1*	*1*	*2*
K_{bind} [M^{-1}]	*$6.3 \cdot 10^3$*	*$4.4 \cdot 10^3$*	*$7.8 \cdot 10^3$*
SOD: IC50 [µM]	*1.41*	*1.04*	*1.21*
CAT: R_0 [µmol/min]	*0.34*	*0.52*	*0.67*
Peroxidase activity [Morin oxidation in 1000 min]	*65%*	*36%*	*90%*
β-sheet inhibition: ligand, complex	*97%, 80%*	*51%,74%*	*74%,98%*

4. Experimental section

4.1 Materials

All commercially available reagents and solvents, provided by Sigma-Aldrich, Carlo Erba, Fluka and Genscript were used without further purification. MilliQ-deionized water (Millipore), with a Jetpore virgin ion-exchange resin was used for the buffer preparation and for spectrometric measurements.

4.2 Instrumentation

- **pH-meter:** pH was measured by using a Metrohm 827 pH lab instrument.
- **^{1}H-NMR spectra** were recoded with a Bruker 200 spectrometer operating at 200 MHz. The chemical shifts were assigned using $Si(CH_3)_4$ as reference (δ ^{1}H-NMR= 0 ppm). For the peaks multiplicity, the following symbols were used: s: singlet, d: doublet, t: triplet, q: quartet, m: multiplet.
- **FT-IR spectra** were recorded with a Nicolet 5700-Thermo Electron Corporation instrument. Throughout the vibrational bands assignment, the following symbols were used: w: weak signal, m: medium signal, s: strong signal, b: broad signal.
- **UV-vis spectra** were recorded with a spectrometer Varian Cary 50, using quartz cuvette with 1 cm optical path.
- **Fluorescence spectra** were recorded with a plate reader, using a Tecan Infinite instrument.
- **ESI-MS (+) spectra** were collected with an Agilent LC/MSD Trap SL spectrometer, by using a capillary potential of 1500V. The solvents used were CH_3CN and H_2O.
- **Catalytic measurements:** superoxide dismutase test (SOD) were carried out with Varian Cary 50 instrument, using quartz cuvette with 1 cm optical path; hydrogen peroxide dismutation test (CAT) were performed using a reactor, equipped with a pressure transducer and a septum for the injection.
- **Electrochemistry:** cyclic voltammetry experiments were executed using a Cell C3 BAS EC-epsilon potentiostat. A three-electrode electrochemical cell was used:

glassy carbon electrode (3 mm diameter, geometric surface area = 7 mm^2) as the working electrode, Pt wire as the auxiliary electrode and Ag/AgCl (3M NaCl) electrode as the reference electrode.

- **Protonation constants of ligands and complexes** were calculated using the software Hyperquad 2008 (Peter Gans, "Protonic Software").
- **Potentiometry:** the potentiometric titrations were carried out with a Titrando 905 by Metrohm system equipped with combined pH electrode (Biotrode by Metrohm), which is dedicated for the measurement of very small volumes. The ligands and the complexes were dissolved in DMSO (5% v/v/H_2O(HCl/KCl) in order to obtain a concentration of 1 mM. Except for $Cu_2(BPMP)(H_2O)_2(ClO_4)_3$, dissolved in H_2O (HCl/KCl), because it is soluble in aqueous media. The titrant (NaOH 0.1M) was added with a micrometric syringe, at 298 K in the pH range of 2.5-11.5, in an argon atmosphere.
- **X-ray measurements: t**he measurements were carried out with an Oxford Diffraction Gemini E diffractometer, equipped with a 2 K × 2 K EOS CCD area detector and sealed-tube Enhance (Mo) and (Cu) X-ray sources. Mo-Ka (λ = 0.71073 4 Å) radiation was used in all cases. Data collection, reduction and finalisation were carried out through the CrysAlisPro software. The structures was solved by direct methods and subsequently completed by Fourier recycling using the SHELXTL-2013 software package[61] and refined by the full-matrix least-squares refinements based on F^2 with all observed reflections, using established methods[62,63].

4.3 Ligands synthesis

Synthesis of the intermediate BPMA: bis-(2-pyridylmethyl) amine

The BPMA synthesis was carried out following the procedure described in the literature, by Hamman et al[39].

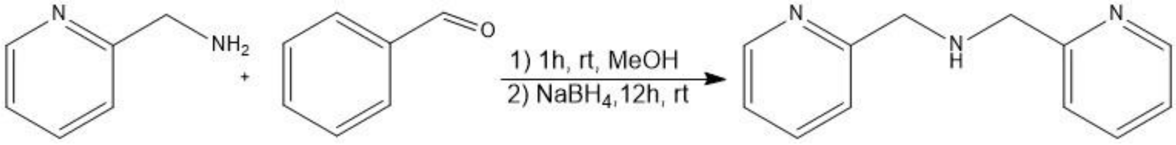

3.02 g (28.2 mmol) of pyridine-2-carboxaldehyde in 10 mL of methanol, at 0°C were slowly added to 3.02 g (27.9 mmol) of 2-(aminomethyl)pyridine in 10 mL of methanol. The dark yellow solution obtained was stirred for 1 hour at room temperature. Afterwards, 0.391 g (10.3 mmol) of $NaBH_4$ were added at 0°C. During the addition, it is possible to observe the formation of a yellow foam, and the solution turned to dark orange. When the addition was completed, the reaction mixture was stirred for 12 h at room temperature. The day after, the solution changed its colour to dark yellow and was poured over ice. HCl 2M was added until pH 4 was reached, at this point the solution turned to dark orange. The mixture was dried in vacuo and the oil obtained was dissolved in 14 mL of water. The brown solution was washed with 5 x 10 mL aliquots of CH_2Cl_2, until the organic phase became colourless. To the aqueous layer was added saturated Na_2CO_3, to reach pH 10. The solution was extracted with CH_2Cl_2 (8 x 10 mL) and the organic phase was dried with Na_2SO_4. The mixture was filtered and the solvent was removed under vacuum to obtain a dark brown oil (19.6 mmol, 70%).

ESI-MS(+) (m/z): 200.1 $[C_{12}H_{14}N_3]^+$; (calc: 200.12)

^{1}H-NMR (200MHz, CD_2Cl_2): δ: 8.65 (d, J= 4.3 Hz, 2H), 7.76 (td, J=11.0,5.5 Hz 2H), 7.60-7.37 (m, 2H), 7.36-7.18 (m, 2H), 5.45 (m,1H), 4.05 (s, 4H), 2.67 (s, 1H, -NH) ppm.

Synthesis of HBBPMA (HL1): N-(2-hydroxylbenzyl)-N,N-bis(2-pyridylmethyl)amine

This ligand was synthetized following the procedure described by *Connor et al*[40].

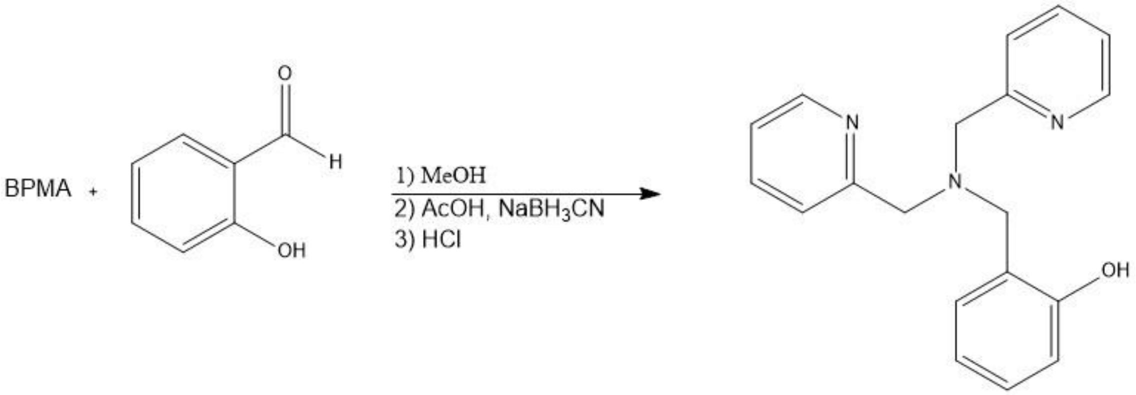

0.710g (5.82 mmol) of slicylaldehyde were dissolved in 17 mL of MeOH. After that, a solution of 1.1490 g (5.77 mmol) in 13 mL of MeOH was added. The colour of the solution was dark yellow. Then, three drops of glacial acetic acid were added, followed by the dropwise addition of solution containing 0.195 g (9.10 mmol) of sodium cyanoborohydride in 2.6 mL of MeOH. After the addition, no change in the solution colour was observed. The resulting solution was refluxed for 1 hour and stirred at 60°C. After this operation, the reflux was removed and the solution was stirred overnight at room temperature. HCl 2M was added till pH 4.1 (verify by pH-meter). This addition caused a change in the colour from orange to light red. The solution was dried in vacuo, dissolved in 12.5 mL of saturated Na_2CO_3 and then extracted with $CHCl_3$ (3 x 30 mL). The organic phase was dehydrated with Na_2SO_4. The mixture was filtered and the liquid was evaporated to dryness to obtain a dark red oil. The oil was purified with a chromatographic column (silica, DCM : MeOH 8:2, with NH_4Cl-saturated eluent, to optimize the elution of the amine product, which otherwise interact with silica, slowing down the run). After the purification, the product was dissolved in dichloromethane and extracted with water (4 x 10 mL), in order to remove the NH_4Cl. The organic phase was dried with Na_2SO_4 and filtered. The solvent was removed under vacuum to yield a red oil.

Yield: 0.951 g (3.11 mmol); 54%

ESI-MS(+) (m/z): 306.2 [$C_{19}H_{20}N_3O$]$^+$; (calc: 306.16)

FT-IT (ν, cm^{-1}): 3239(b), 3050 (w), 3014 (w), 2922 (w), 2801 (w), 2701 (w), 2602 (w), 2388 (b), 2289 (b), 1375 (w), 1657 (w), 1600 (s),1586 (s), 1486 (s), 1435 (s), 1374 (s), 1369 (s), 1287 (s), 1242 (s), 1159 (m), 1123 (m), 1088 (m), 1038 (s), 1010 (s), 974 (s), 903 (m), 867 (m), 825 (w), 761 (s), 633 (w), 597 (w).

^{1}H-NMR (200MHz, $CDCl_3$): δ 8.62-8.52 (m, 2H), 7.63 (td, J= 7.7, 1.8 Hz, 2H), 7.34 (d, J=7.8 Hz, 2H), 7.22-7.13 (m, 3H), 7.06 (dd, J=7.5, 1.5 Hz, 1H), 6.91 (dd, J= 8.0, 0.9 Hz, 1H), 6.77 (td, J= 7.3, 1.1 Hz, 1H), 3.87 (s, 4H), 3.79 (s, 2H) ppm.
Anal. Elem. Calc. for $C_{19}H_{19}N_3O$ (%): C, 74.73; H, 6.27; N, 13.76; **found:** C, 74.13; H, 6.50; N, 14.13.

Synthesis of BPMAMMP (HL5): 2-{[Bis(pyridin-2-ylmethyl)amino]methyl}-6-methoxyphenol

The procedure for the synthesis of this ligand is the same as the previous one[40].

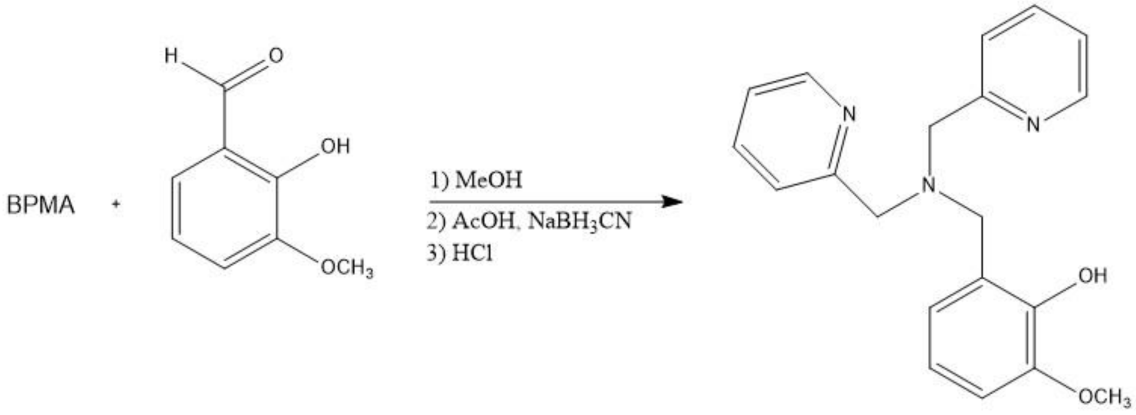

For the reaction 0.886 g (4.5 mmol) of BPMA, 0.658 g (4.3 mmol) of o-vanillin, were used in 25 mL of MeOH, 0.197g (3.13 mmol) of $NaBH_3CN$ in 2.5 mL of MeOH. The product was purified with a chromatographic column, using as eluent DCM : MeOH 8:2, saturated with NH_4Cl.

Yield: 0.644 g (1.92 mmol), 44%

ESI-MS(+) (m/z): 336.2 $[C_{20}H_{22}N_3O_2]^+$; (calc: 336.17)

FT-IT (ν, cm^{-1}): 3058 (b), 3006 (b), 2912 (b), 2834 (b), 2802 (w), 2615 (w), 2358 (m), 2333 (m), 1585 (s), 1479 (s), 1433 (s), 1387 (s), 1373 (s), 1299 (s), 1249 (s), 1130 (m), 1070 (s), 1001 (m), 975 (m), 900 (w), 839 (w), 762 (s), 627 (w), 464 (w).

^{1}H-NMR (200MHz, $CDCl_3$): δ 8.65 – 8.52 (m, 2H), 7.61 (td, J =7.7, 1.8 Hz, 2H), 7.37 (d, *J* = 7.8 Hz, 2H), 7.22 – 7.05 (m, 2H), 6.86-6.81 (m,1H), 6.76 – 6.66 (m, 2H), 3.90 (s, 3H), 3.87 (s, 4H), 3.80 (s, 2H) ppm.

Anal. Elem. Calc. for $C_{19}H_{21}N_3O_2$ (%): C, 71.62; H, 6.31; N, 12.53; **found:** C, 70.55; H, 6.45; N, 12.47.

Synthesis of HBPMP: 2,6-bis[(bis(2-pyridylmethyl)amino)methyl]-4-methylphenol

The ligand HBPMP was synthesized according to the procedure described by *Torelli et al*[42], with some modification.

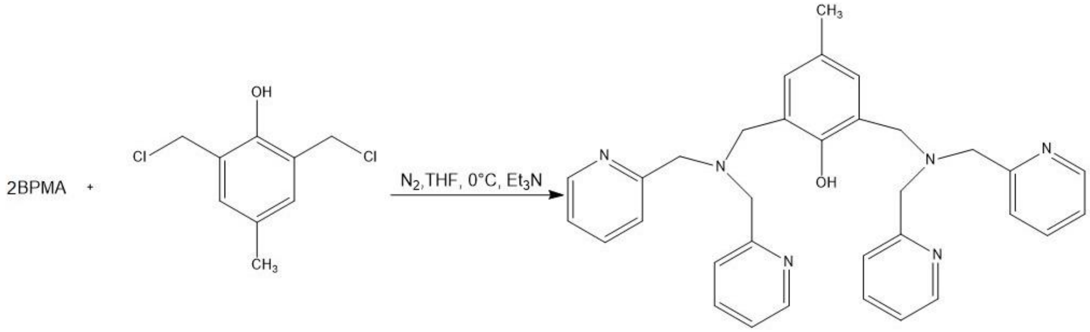

Under a dinitrogen atmosphere, a mixture of bis(2-pyridylmethyl)amine (0.975 g, 4.9 mmol) and triethylamine (1.01 g, 10 mmol) in 2,6 mL of dry THF were added dropwise to a stirred solution of 2,6-bis(chloromethyl)-4-methylphenol (0.525 g, 2.5 mmol) in 5 mL of dry THF at 0°C. The addition caused the formation of a dark yellow precipitate. When the addition was completed, the resulting mixture was stirred at room temperature. After 2.5 days, the mixture was filtered, and the filtrate was concentrated under reduced pressure. The residue was dissolved in 30 mL of methylene chloride, washed with brine, and dried over anhydrous Na_2SO_4. After the filtration, the solvent was removed under vacuum and a brown oil was obtained. The product was purified with a chromatographic column, using a mixture of acetone :

MeOH 8:2, as eluent. The solution was evaporated to dryness at reduced pressure to yield a yellow oil.

Yield: 0.256 g (0.48 mmol); 20%

ESI-MS(+) (m/z): 531.2 $[C_{33}H_{35}N_6O]^+$ (calc: 531.29)

FT-IT (v, cm^{-1}): 2920 (w), 2814 (w), 1712 (w), 1677 (w),1586 (s), 1570 (s),1474 (s), 1430 (s), 1374 (m),1362 (s), 1298 (m), 1232 (m), 1126 (m), 1049 (m), 1001 (m), 978 (m), 942 (w), 907 (w), 871 (w), 788 (m), 756 (s), 605 (b).

^{1}H-NMR (200MHz, CDCl$_3$): δ 8.68 (d, *J* = 4.9 Hz, 4H), 7.77-7.75 (m, 8H), 7.17-7.30 (t, 4H, partially overlapped with the peak at 7.27 ppm due to the residue solvent $CHCl_3$), 7.19 (s, 2H), 4.45-4.31 (m, 8H), 4.06 (m, 4H), 2.32 (s, 3H) ppm ; peaks of residue solvent: δ 2.18 (s) ppm of $(CH_3)_2CO$, 3.50 (s) ppm of MeOH,3.76 (s) and 1.75 (s) pp of THF, 7.27 (s) ppm of $CDCl_3$.

Anal. Elem. Calc. for $C_{19}H_{21}N_3O_2$ (%): C, 74.69; H, 6.46; N, 15.84; **found:** C, 72.84; H, 6.51; N, 14.80.

4.4 Complexes synthesis

Synthesis of Cu(HL1)(ClO$_4$)$_2$ and Cu(HL5)(ClO$_4$)$_2$

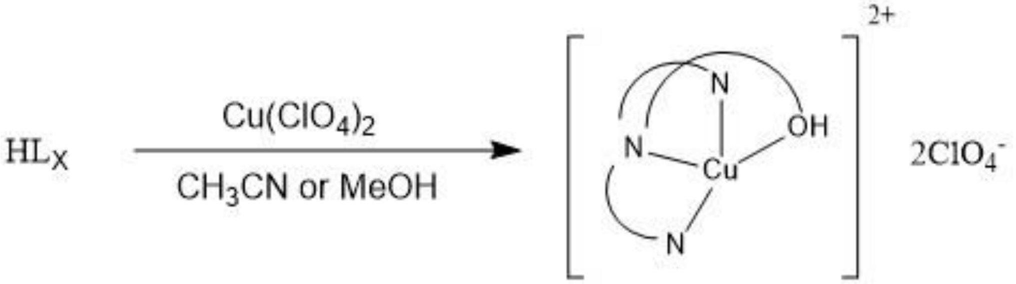

The synthesis of the complexes was carried out mixing equimolar solution of the ligands and $Cu(ClO_4)_2$ in MeOH or CH_3CN. Slow evaporation and liquid / vapor diffusion technique were used to obtain the crystals. For the synthesis of the mononuclear copper complex 0.0905 g (0.30 mmol) of the ligand and 0.107 g (0.29 mmol) of copper perchlorate for Cu(HL1)(ClO$_4$)$_2$, and 0.0908 g (0.27 mmol) and 0.105 g (0.28 mmol) of copper perchlorate for Cu(HL5)(ClO$_4$)$_2$ were used.

Blue crystals, whose structure was studied by X-ray, were recovered.

$Cu(HL1)(ClO_4)_2$ (MW=567.82 g/mol)

ESI-MS(+) (m/z): 367.1 $[C_{19}H_{18}CuN_3O]^+$ (calc: 367.07); 403.0 $[C_{19}H_{19}ClCuN_3O]^+$ (calc:403.05).

FT-IT (ν, cm^{-1}): 2358 (s), 2334 (s), 2251 (w), 1458 (s), 1375 (m), 1292 (m), 1262 (w), 1101 (s), 877 (m), 818 (w), 758 (s), 670 (s), 622 (s).

Anal. Elem. Calc. for $C_{19}H_{21}N_3O_2$ (%): C, 37.79; H, 3.84, N, 6.96; **found:** C, 37.25; H, 3.78; N, 7.18.

$Cu(HL5)(ClO_4)_2$ (MW=597,85 g/mol)

ESI-MS(+) (m/z): 397.1 $[C_{20}H_{20}CuN_3O_2]^+$ (calc: 397.08); 497.0 $[C_{20}H_{21}ClCuN_3O_6]^+$(calc: 497.04)

FT-IT (v, cm^{-1}): 3382 (b), 2356 (s), 2339 (s), 2011 (b), 1616 (m), 1490 (m), 1448 (m), 1373 (w), 1355 (w), 1288 (m), 1238 (w), 1101(b), 917 (w), 782 (w), 665 (m), 625 (m).

Anal. Elem. Calc. for $C_{19}H_{21}N_3O_2$ (%):C, 39.01; H, 3.76; N, 6.82; **found:** C, 39.06; H, 4.00; N, 6.86.

Single-crystal X-ray diffraction (XRD) study

Single-crystal XRD experiments were carried out by Dr. Nadia Marino at the Dipartimento di Scienze Chimiche of Padova. Crystals suitable for the diffraction analysis were carefully chosen under the microscope, mounted on a nylon loop with the aid of either Paratone oil or Loctite glue, positioned over a goniometer head and transferred in the diffractometer collection chamber. The samples were collected at room temperature (R.T.), except in one case. Concerning the monomeric Cu(II) complex with the HL_1 ligand, the crystals grown from CH_3CN/Et_2O could be successfully analyzed at R.T. by using some tricks to slow down the lattice solvent loss. Crystals grown from $MeOH/Et_2O$, instead, decomposed too quickly out of the mother solution, even at low temperature, and every attempt to collect data at either R.T. or low temperature was unsuccessful.

Concerning the monomeric Cu(II) complex with the HL_5 ligand, the crystals grown from CH_3CN/Et_2O appeared very stable and could be analyzed easily at R.T. with no special precautions at all. In this case, also the crystals grown from $MeOH/Et_2O$ could be successfully analyzed, as by collecting them at about 150 K, crystal decomposition was delayed enough to get a significant amount of data.

Synthesis of $[Cu_2(BPMP)(H_2O)_2](ClO_4)_3$

The dinuclear complex was synthetized according to the procedure described by *Torelli et al*[42], with some modification.

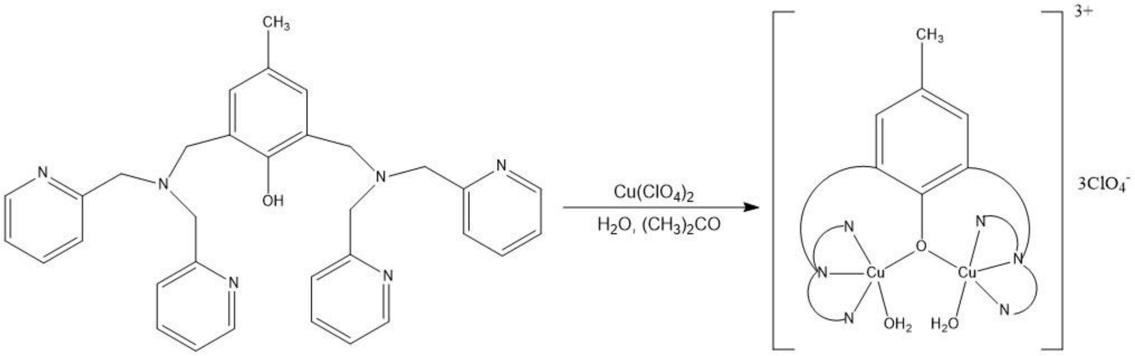

0.0578 g (0.11mmol) of HBPMP were dissolved in a solution of water: acetone 1:1. After the complete solubilization, the solution appeared yellow and 0.0822 g (0.22 mmol) of $Cu(ClO_4)_2$ in 2,5 mL of water was added dropwise. The solution turned to brown instantaneously and was stirred at room temperature for three hours. The crystallization of the product was obtained through the slow evaporation technique and with the interface method. In this last case, 2mL of diethyl ether were added, and the solution was allowed to stand at 4°C for 12h. 0.0342 g (0.0345 mmol, 32%) of brown crystals ware recovered.

ESI-MS(+) (m/z): 727.2 $[C_{33}H_{37}ClCuN_6O_7]^+$ (calc: 727.12); 745.2 $[C_{33}H_{39}ClCuN_6O_8]^+$ (calc: 745.18)

FT-IT (ν, cm^{-1}): 3535 (b), 3399 (b), 2927 (w), 2860 (w), 23362 (m), 2338 (w), 2023 (b), 1616 (s), 1474 (s), 1450 (s), 1294 (m), 1096 (b), 862 (m), 767 (s), 625 (s).

Anal. Elem. Calc. for $C_{19}H_{21}N_3O_2$ (%): C, 37.28; H, 4.27; N, 7.90; **found:** C, 37.97; H, 4.11; N, 7.69.

4.5 Measurement of the catalytic activity

Cyclic voltammetry

The cyclic voltammogram of the complexes were carried out with a three-electrode setup system: a working electrode (GCE, glassy carbon), a counter electrode (Pt) and a reference electrode Ag/AgCl (NaCl 3M). A phosphate buffer (PBS) 10 mM with NaCl 0.1 M, as a supporting electrolyte was prepared. For each mononuclear complex, 3 mL of solution CH_3CN (5% v/v)/ PBS, with 0.50 mM of the catalyst, were prepared. Concerning the dinuclear complex, the concentration of the catalyst was 0.25 mM, and the solution was made in PBS, because this complex is soluble in water. Prior to each experiment, the electrode was cleaned with alumina, washed with water and wiped with a paper tissue. Nitrogen was used to as a purging gas to remove dioxygen, upon bubbling for 15 min before each measurement. Before the acquisition of the sample solutions, the behaviour of the solutions with CH_3CN (5% v/v)/ PBS, and only PBS were checked. The measurement was carried out between 400 and -500 mV, with a scan rate equal to 50 mV/s. The voltammogram of the mononuclear complexes were also recorded at different scan rate: 100, 200, 400 and 800 mV/s.

Superoxide radical anion dismutation: SOD test

The SOD-like activity was studied, using an indirect method with Cytochrome C (Cytc C), primarily described by McCord and Fridovich, with some modifications[50]. Using UV-vis spectroscopy, it was possible to evaluate the screening of the inhibition of Cytochrome C reduction to Ferricytochrome, due to the superoxide radical anion, oxidized to hydrogen peroxide. The radical anion was produced by xanthine/xanthine oxidase system, *in situ*. Since Ferricytochrome absorbs at 550 nm, the trend of absorbance at this wavelength was monitored over time.

For this assay the following solution were prepared:

- Phosphate buffer solution 50 mM pH = 7.8, in deionized water;
- Xanthine solution, in deionized water;
- Cytc C stock solution: 15.4 mg of Cyc C in 120 mL of phosphate buffer and 5 mL of Xanthine;
- Catalase (Cat) stock solution 15 µg/mL, in deionized water, in order to scavenge hydrogen peroxide produce by dismutation of superoxide radical;
- Catalyst solution 100 µM in CH_3CN, in the case of mononuclear complexes, in deionized water for the dinuclear complex.

The sample solutions were prepared in a quartz cuvette, with 1 cm optical path, respecting the addition order, shown in *Table 19*.

Table 19*: Samples composition for the SOD activity determination.*

Addition order	**1° measure**	**2° measure**	**3° measure**	**4°measure**
1. *Stock sol. Cytc C*	3 mL	3 mL	3 mL	3 mL
2. *Stock sol. Cat*	10 µL	10 µL	10 µL	10 µL
3. *Phosphate buffer*	30 µL	25 µL	20 µL	10 µL
4. *Catalyst*	0 µL	5 µL	10 µL	20 µL
5. *Xanthine oxidase*	20 µL	20 µL	20 µL	20 µL

The last addition is the one relative to xanthine oxidase, since the production of superoxide radical anion was instantaneous, the acquisition must start immediately after the addition.

From the linear plot of *"% inhibition of Cytc C reduction vs effective catalyst concentration"*, the IC_{50} values of the complexes was extrapolated. The catalyst kinetic constant k_{cat}, relative to superoxide radical anion scavengeing was calculated from the equation:

$$k_{cat}\ (O_2^{\bullet -}) = k_{CytcC}\ * [CytcC]/\ IC_{50}$$

where k_{CytcC} is equal to $2.6 \times 10^5\ M^{-1}s^{-1}$, according to McCord and Fridovich[50].

The measurement was duplicated and the experiment was carried out three times, for every complexes.

Hydrogen peroxide dismutation

The catalase activity was evaluated by monitoring the pressure developed by the oxygen, resulting from the dismutation of the hydrogen peroxide over a period of about 22 hours.

The analysis was carried out by the use of a borate buffer (BBS). 12 mL of a solution with 30 mM of H_2O_2 (41 μL from [H_2O_2] = 8.8 M), and 200 μM of the catalyst (600 μL from the stock solution 4mM in CH_3CN, in the case of the mononuclear complexes, and in deionized water in the case of the dinuclear one) were prepared in BBS 50 mM pH = 7.8.

The reactor, equipped with a septum, was closed and maintained at 25°C by a circulating thermostat. The measuring cell was connected to a transducer, in order to measure the variation of pressure in the head-space, due to the production of molecular oxygen, generated from hydrogen peroxide dismutation. The head-space volume of the reactor was equal to 14.6 mL.

First, it was monitored the pressure of the solution without the catalyst. In fact the buffer solution with hydrogen peroxide did not generate molecular oxygen. After few minutes, required for signal stabilization, the catalyst was added through the septum.

The law of perfect gas was used to evaluate the molecular oxygen micromole, developed in the head-space, at 25°C. The initial rates were calculated by linear regression of data at < 30% H_2O_2 conversion.

Measurement of peroxidase like-activity

The peroxidase activity can be evaluated by UV-Vis spectroscopy, monitoring over time the absorbance variation of the UV-Vis bands of different substrates, which were oxidized by H_2O_2, activated by the copper complexes studied. Two different substrates were used for this analysis: morine and o-phenylenediamine (OPD).

The first substrate evaluated was the morin. The presence of hydrogen peroxide and a catalyst, with a peroxidase like-activity induced the oxidative degradation of the morine. This process was highlighted by the decrease in the absorbance over time, at the maximum absorption of morin, at 390 nm. The measurements were carried out in a phosphate buffer (PBS) 50mM (0.1 M NaCl, pH=7.8) at 25°C, using a quartz cuvette, with 1 cm optical path. The concentration used were: 3.2 µM of the catalyst, 10 mM of H_2O_2 and 0.055 mM of morine. The kinetic were followed over a period of 18 hours, acquiring the absorbance at intervals of 20 minutes.

The second substrate was the o-phenylenediamine (OPD), that oxidizes to 2,3-diaminephenazine (DAP), a colour and fluorescent compound. The kinetic was carried out following the increase in absorbance at 420 nm, due to the formation of DAP. For this analysis a phosphate buffer (PBS) 50mM (0.1 M NaCl, pH=7.8) at 25°C, a quartz cuvette, with 1 cm optical path and the following concentration were used: 3.2 µM of the catalyst, 0.024 M of H_2O_2 and 0.32 mM of OPD. The kinetic were followed over a period of 18 hours, acquiring at intervals of 20 minutes.

4.6 spectroscopic measurements

Ligands and complexes scanning

UV-vis scanning for ligands and complexes were carried out in quartz cuvette, with 1 cm optical path. Concerning the ligands, the solution used were in MeOH (5% v/v)/H_2O at concentration of 0.1 mM. For $Cu(HL1)(ClO_4)_2$ and $Cu(HL5)(ClO_4)_2$ the solution were in MeOH (5% v/v)/H_2O at 0.1mM and 1.5mM, in order to highlight, respectively, $\pi \rightarrow \pi$ and $d \rightarrow d$ bands. $[Cu_2(BPMP)(H_2O)_2](ClO_4)_3$ was analysed in water, at 0.1mM and 1.5mM.

Studying of the chelating ability trough titration by UV-vis spectroscopy

Two solution of the ligands at 0.1 mM and 1.5 mM in MQ water were prepared, from the stock solution 4 mM in MeOH. These solutions were titrated with $CuCl_2$ solution, respectively at 0.01 M and 0.15 M in MQ water.

A quartz cuvette, with 1 cm optical path was filled with 2.5 mL of the ligand solution, then aliquots of 2.5 μL of copper (II) solution were added (0.1 eq of Cu^{2+}, for each addition). After each addition, the absorbance variation, by UV-vis scans was followed from 200 nm to 800 nm. The graph *"Abs at* λ_{max} *vs Cu(II) equivalent"* was created, in order to highlight the amount of Cu^{2+}, that was bound to the ligand. The Benesi-Hildebrand equation was applied for the calculation of the binding constant:

$$\frac{1}{\mathrm{A}-\mathrm{A}_0}=\frac{1}{\{\mathrm{K}(\mathrm{A}_{\max}-\mathrm{A}_0)[\mathrm{Cu}^{2+}]\}}+\frac{1}{(\mathrm{A}_{\max}-\mathrm{A}_0)}$$

Where A_0 is the ligand absorbance without the metal; A is the ligand absorbance for an addition of the metal; A_{max} is the absorbance recorded from the maximum concentration of the metal; K is the binding constant. The binding constant K is obtained from the slope in the plot *"1/(A-*A_0*) vs 1/[*Cu^{2+}*]"*.

Stechiometry detemination by Job's Plot

The method of continuous variations, or Job's plot is a method that allows the stoichiometry determination of a binding event. Particularly, it highlights the formation of the complexes with 1:1 stoichiometry. The experiment is based on the Uv-vis spectra acquisition of in situ generated complex, from 200 to 800 nm. In each scan, the molar ration of the metal and the ligand were changed, but the total mole number of the system remains constant. Concerning the study of the monuclear complexes, two solutions of 0.75 mM, one of the ligand and one of $CuCl_2$ were prepared, in MQ water. For the dinuclear complex, a lower concentration was used (0.375mM), due to the precipitation of the ligand in aqueous media. In a quartz cuvette, with 1 cm optical path, different ratios of ligand an metal were added , according to *Table 20* and *Table 21*:

Table 20: *Samples composition for the determination of stechiometry by Job's Plot, for HL1 and HL5.*

N° scans	µmol Cu	µmol HL_X	µmol tot	V (µL) Cu	V (µL) HL_X	V (µL) tot
1	0	2.25	2.25	0	3000	3000
2	0.225	2.025	2.25	300	2700	3000
3	0.450	1.800	2.25	600	2400	3000
4	0.675	1.575	2.25	900	2100	3000
5	0.900	1.350	2.25	1200	1800	3000
6	1.125	1.125	2.25	1500	1500	3000
7	1.350	0.900	2.25	1800	1200	3000
8	1.575	0.675	2.25	2100	900	3000
9	1.800	0.450	2.25	2400	600	3000
10	2.025	0.225	2.25	2700	300	3000
11	2.25	0	2.25	3000	0	3000

Table 21: *Samples composition for the determination of stechiometry by Job's Plot, for HBPMP.*

N° scans	µmol Cu	µmol HBPMP	µmol tot	V (µL) Cu	V (µL) HBPMP	V (µL) tot
1	0	1.1250	1.125	0	3000	3000
2	0.1125	1.0125	1.125	300	2700	3000
3	0.225	0.900	1.125	600	2400	3000
4	0.3375	0.7875	1.125	900	2100	3000
5	0.450	0.675	1.125	1200	1800	3000
6	0.5625	0.5625	1.125	1500	1500	3000
7	0.675	0.450	1.125	1800	1200	3000
8	0.7875	0.3375	1.125	2100	900	3000
9	0.900	0.225	1.125	2400	600	3000
10	1.0125	0.1125	1.125	2700	300	3000
11	1.125	0	1.125	3000	0	3000

With these data, the graph “*A_{max} vs Cu(II) equivalent*” was obtained. The curve is characterized by a maximum at equal ratio of copper and ligand (maximum concentration of the complex in solution), when the stoichiometry is 1:1. On the other hand, in the case of the dinuclear complex, where the ratio between ligand and copper is 1:2, the curve presents a maximum at higher ratio of copper with respect to that of ligand.

Aggregation test: ThT method

Amyloid peptides Aβ1-40 were used for this analysis. 1 mg of the amyloid peptide was dissolved in 1 mL of 1,1,1,3,3,3-Hexafluoro-2-propanol and stirred for about 12 hours at 4°C. Solvent was evaporated with a soft stream of N_2 and re-dissolved in 10mM phosphate buffer (NaCl 100mM, pH=7.4), to obtain a concentration of 77 μM (3 mL, MW = 4329.82 g/mol).

A ThT fresh solution 0.04mM was prepared in 10 mM PBS buffer (NaCl 100mM, pH= 7.4), from a mother solution 5mM in water. The concentration was checked by Uv-vis spectroscopy, from the molar extinction coefficient (ε) of the band at 412 nm, equal to 36000 $M^{-1}cm^{-1}$.

The solutions 0.2 mM of copper, ligands and preformed complexes were prepared in methanol.

For the measurement a plate reader was used: in each cockpit (300 μL), the solutions were organized as follows:

1. ThT 10 μM;
2. ThT 10 μM, Aβ 10 μM;
3. ThT 10 μM, Aβ 10 μM, HL1 10 μM;
4. ThT 10 μM, Aβ 10 μM, HL5 10 μM;
5. ThT 10 μM, Aβ 10 μM, HBPMP 10 μM;
6. ThT 10 μM, Aβ 10 μM, $Cu(HL1)(ClO_4)_2$ 10 μM;
7. ThT 10 μM, Aβ 10 μM, $Cu(HL5)(ClO_4)_2$ 10 μM;
8. ThT 10 μM, Aβ 10 μM, $Cu_2(BPMP)(H_2O)(ClO_4)_3$ 10 μM;

Every solution was brought up to volume with PBS buffer 10 mM (NaCl 100mM, pH = 7.4).

The fluorescence of sample solutions was monitored at 37° C over a period of about 30 hours, acquiring values every 20 minutes. The fluorescence variation of ThT was compared in the presence/ absence of amyloid/ ligands/ complexes.

5. Appendix

5.1 ^{1}H-NMR, ESI-MS, FT-IR, UV-vis spectra

5.1.1 Bis-(2-pyridylmethyl) amine (BPMA)

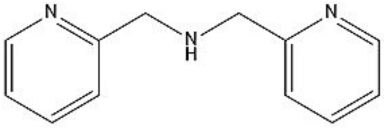

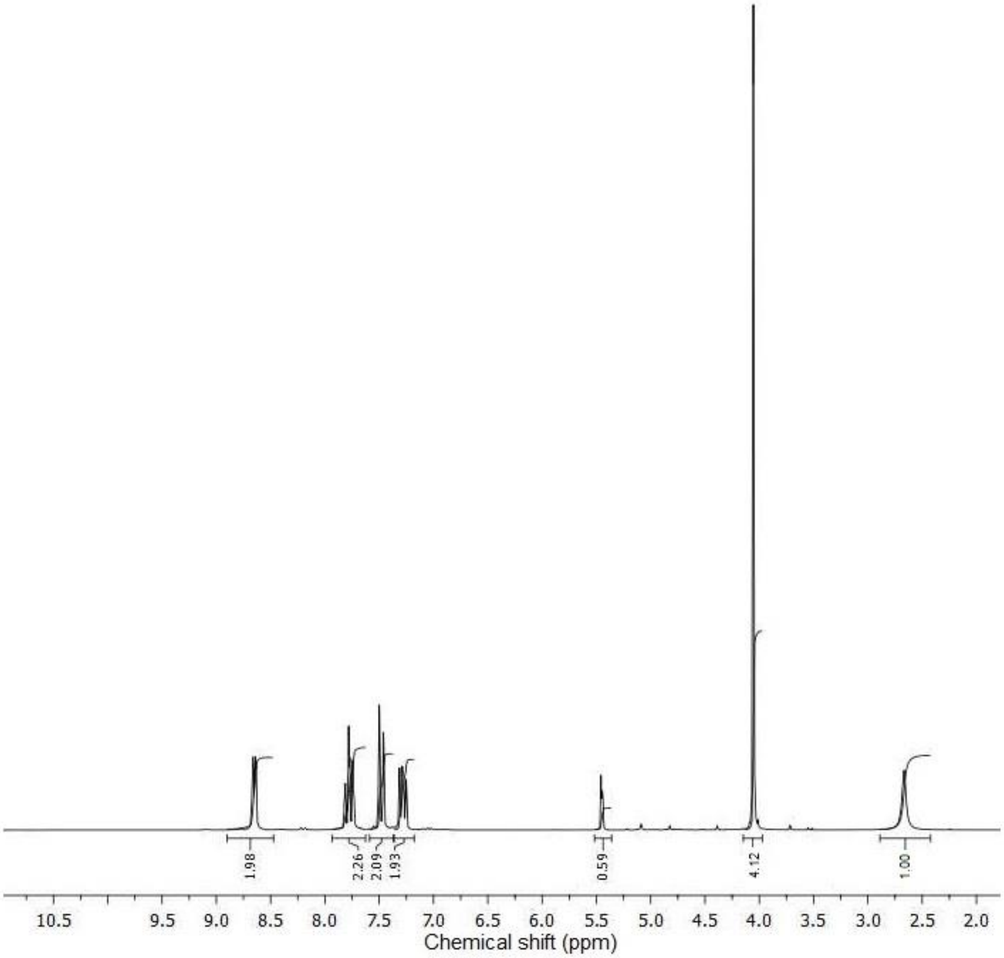

^{1}H-NMR spectrum (200 MHz, CD_2Cl_2) of the intermediate BPMA

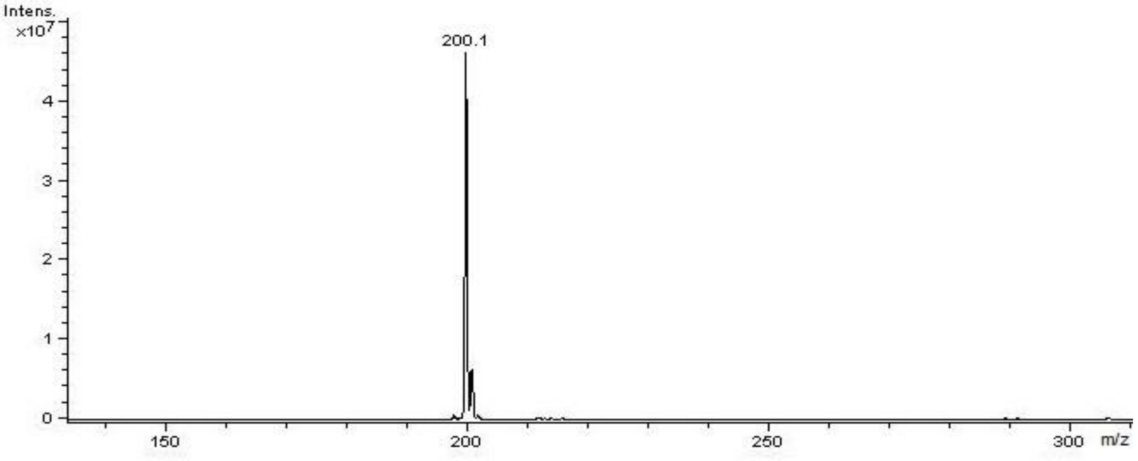

ESI-MS (+) spectrum (CH_3CN, m/z) of BPMA

5.1.2 N-(2-hydroxylbenzyl)-N,N-bis(2-pyridylmethyl)amine (HL1)

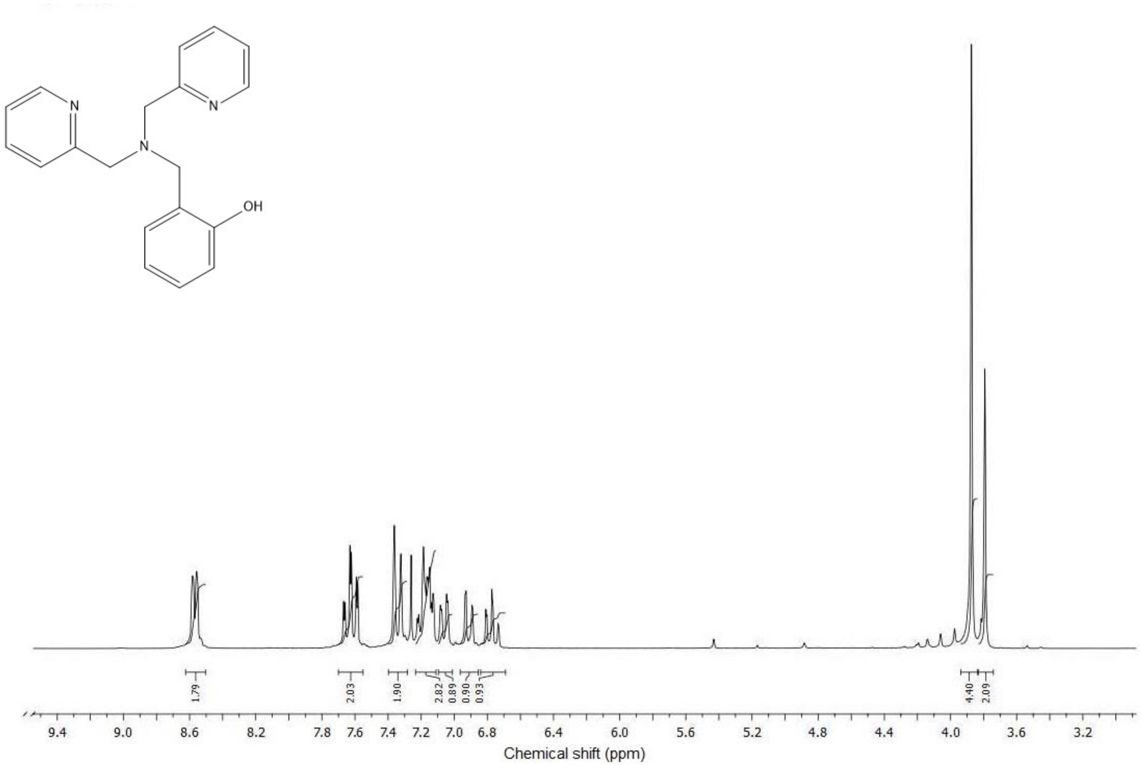

^{1}H-NMR spectrum (200 MHz, $CDCl_3$) of the ligand HL1

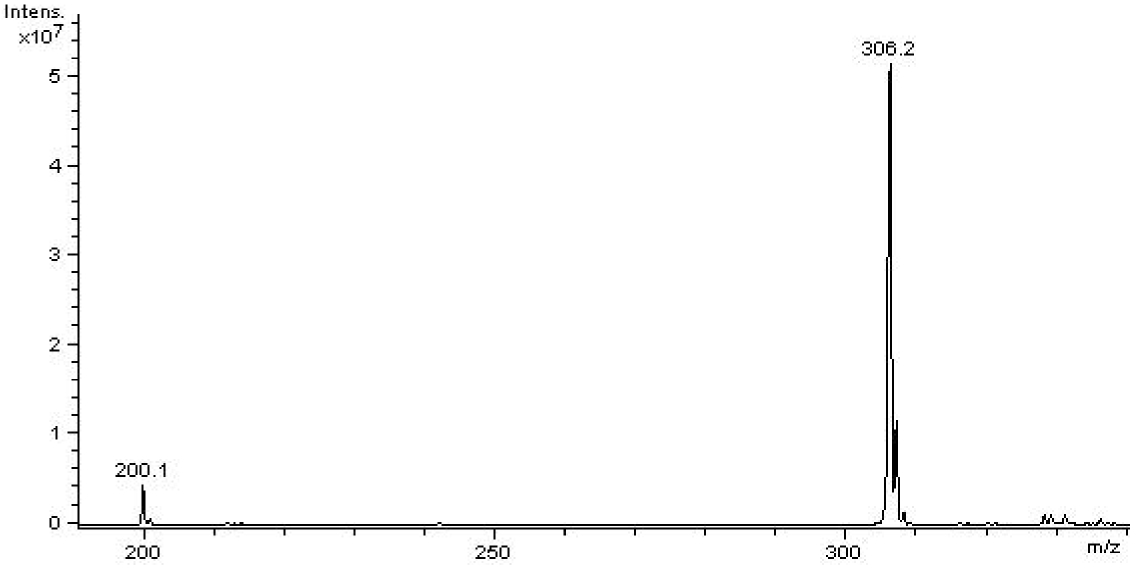

ESI-MS (+) spectrum (CH3CN, m/z) of the ligand HL1

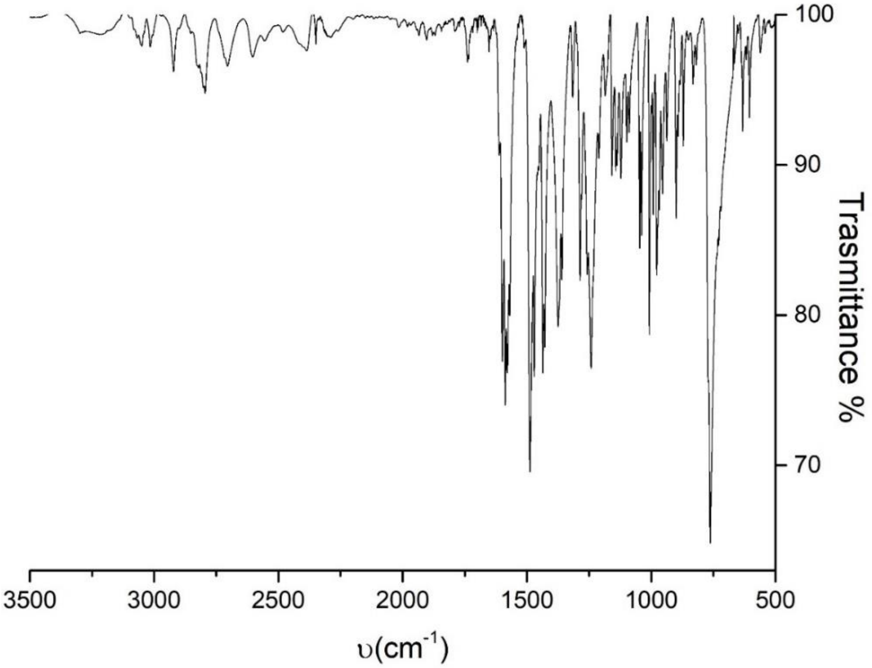

IR spectrum of the ligand HL1 (KBr)

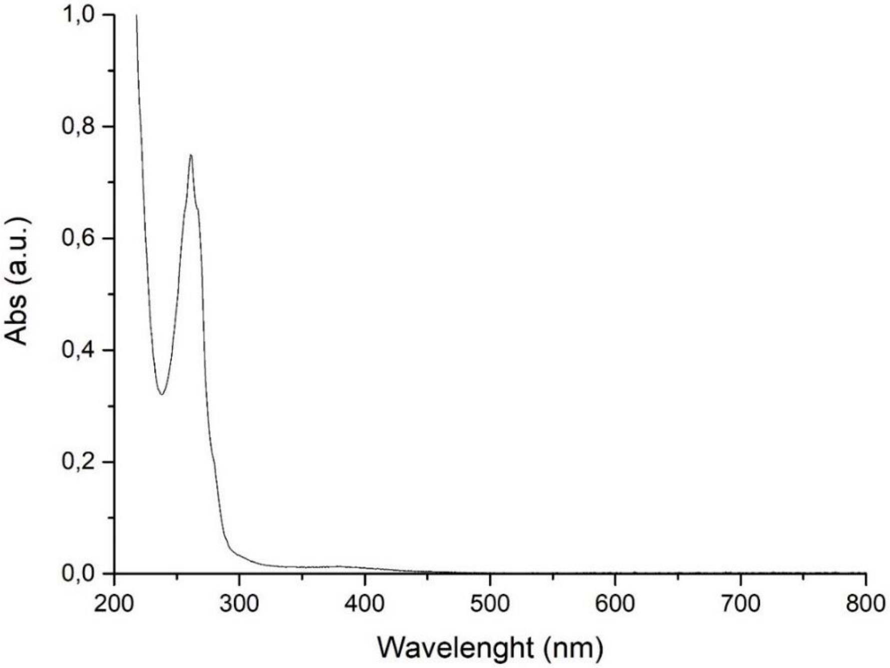

UV-vis spectrum of the ligand HL1 (MeOH 5% v/v/H_2O, 0.1 mM, optical path= 1 cm)

5.1.3 Complex Cu(HL1)(ClO_4)$_2$

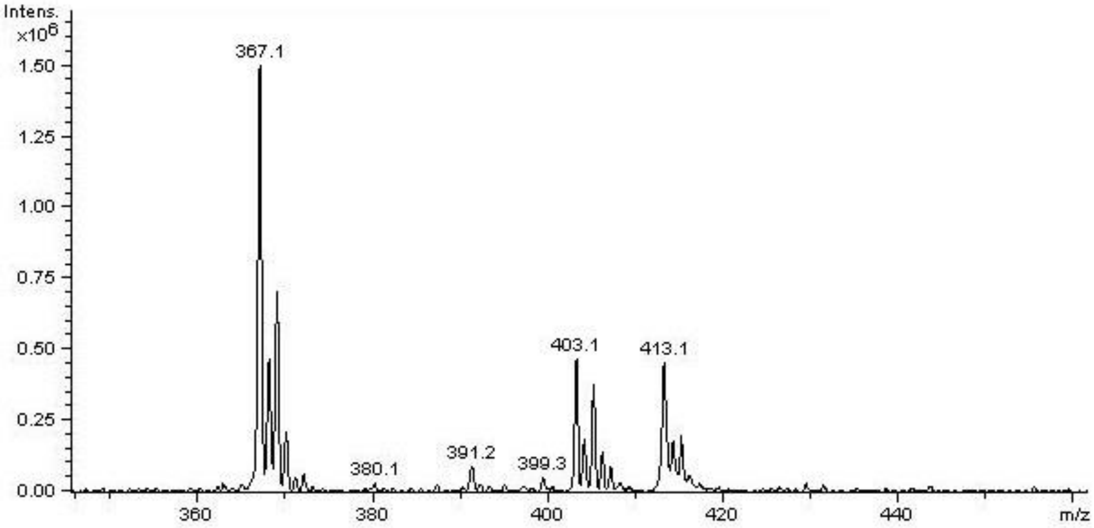

ESI-MS (+) spectrum of the complex Cu(HL1)(ClO_4)$_2$ ($4x10^{-6}$M, CH_3CN, m/z)

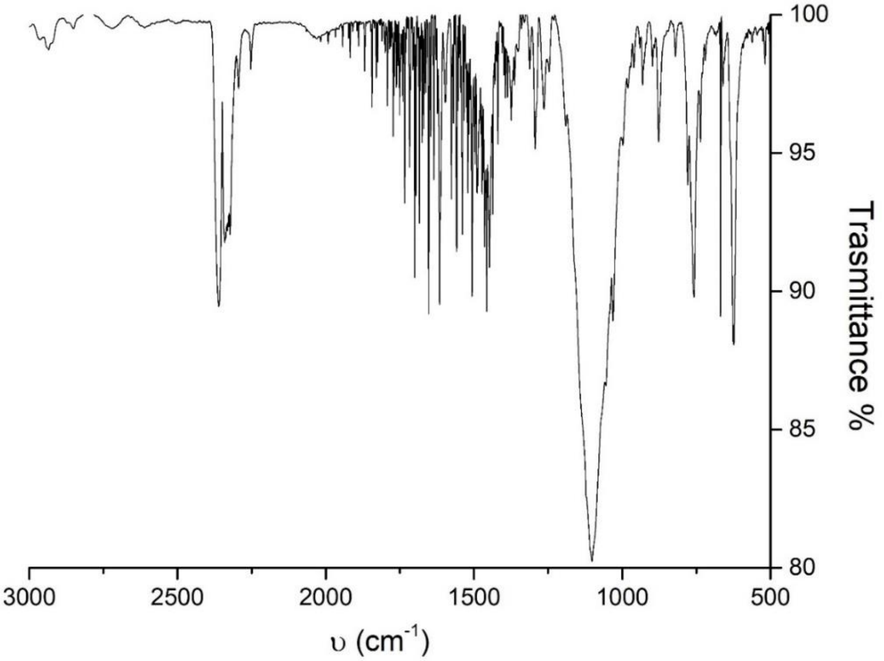

IR spectrum of the complex Cu(HL1)(ClO_4)$_2$ (KBr)

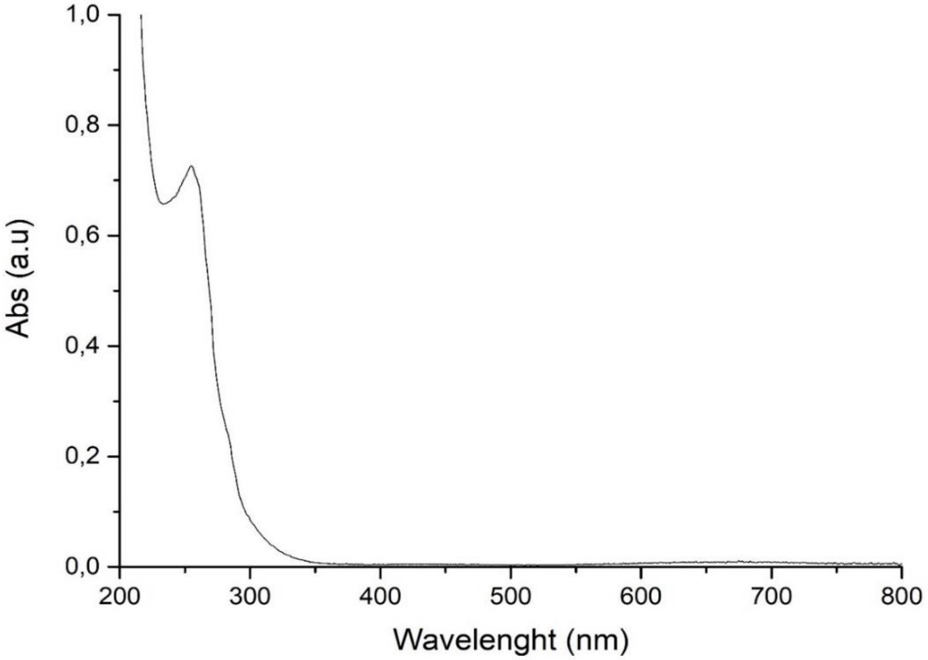

UV-vis spectrum of the complex Cu(HL1)(ClO_4)$_2$ (MeOH 5% v/v/H_2O, 0.1 mM, optical path= 1 cm)

5.1.4 2-{[Bis(pyridin-2-ylmethyl)amino]methyl}-6-methoxyphenol (HL5)

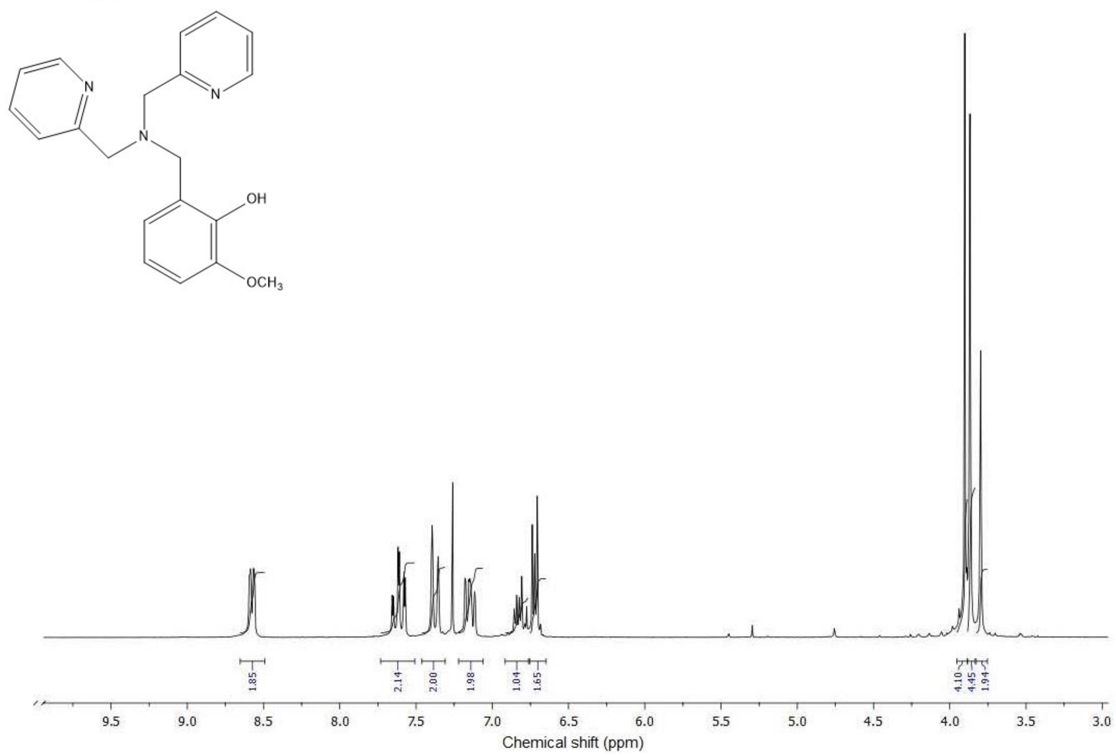

^{1}H-NMR spectrum (200 MHz, CDCl$_3$) of the ligand HL5

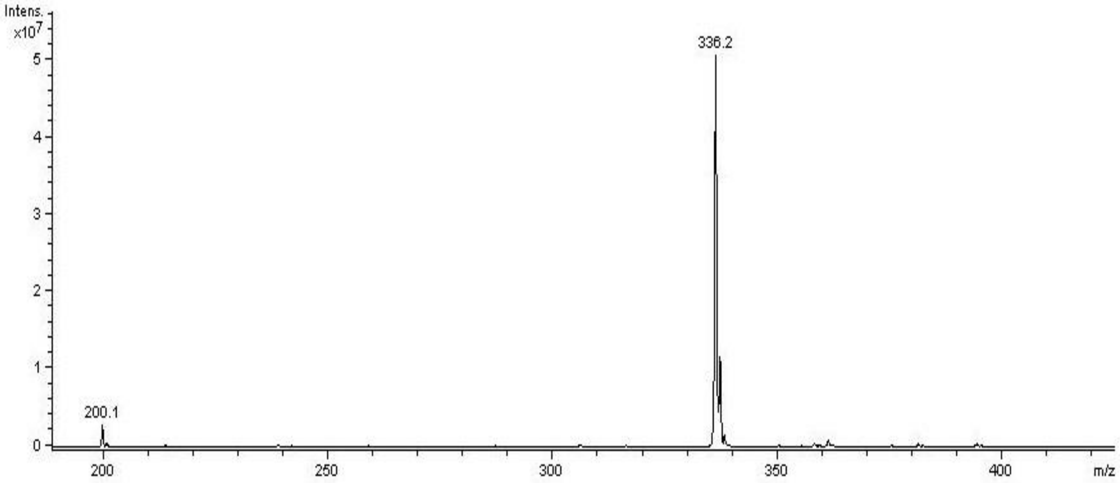

ESI-MS (+) spectrum (CH$_3$CN, m/z) of the ligand HL5

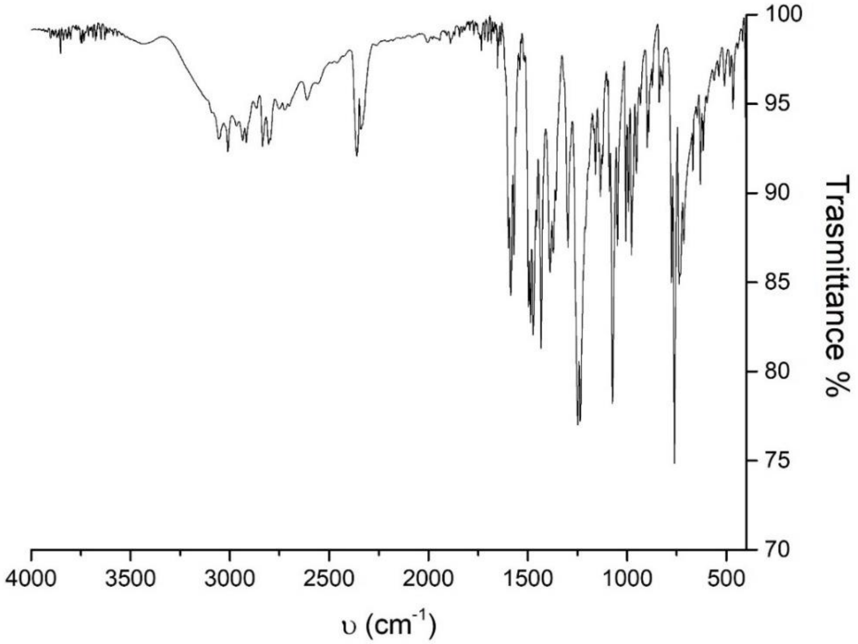

IR spectrum of the ligand HL5 (KBr)

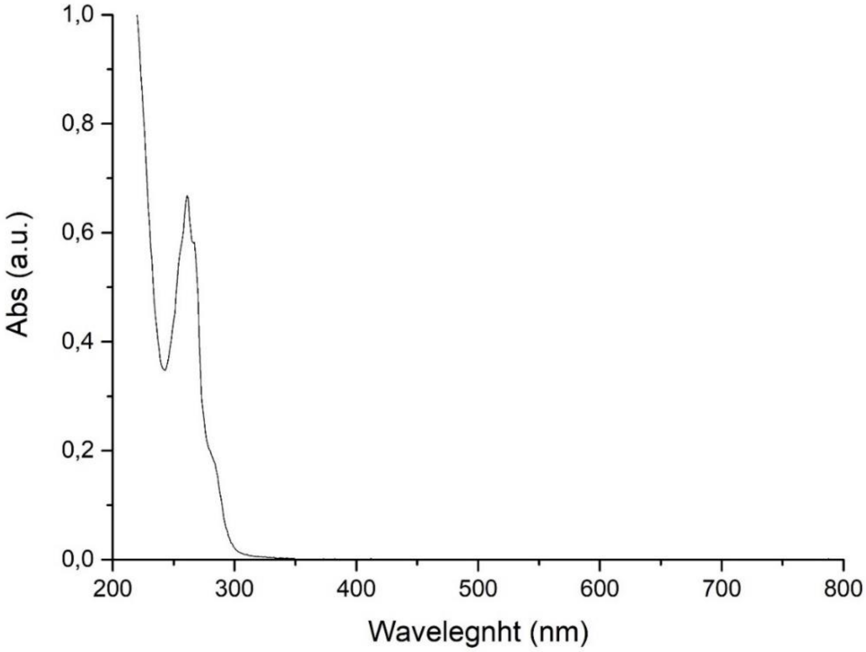

UV-vis spectrum of the ligand HL5 (MeOH 5% v/v/H_2O, 0.1 mM, optical path= 1 cm)

5.1.5 Complex $Cu(HL5)(ClO_4)_2$

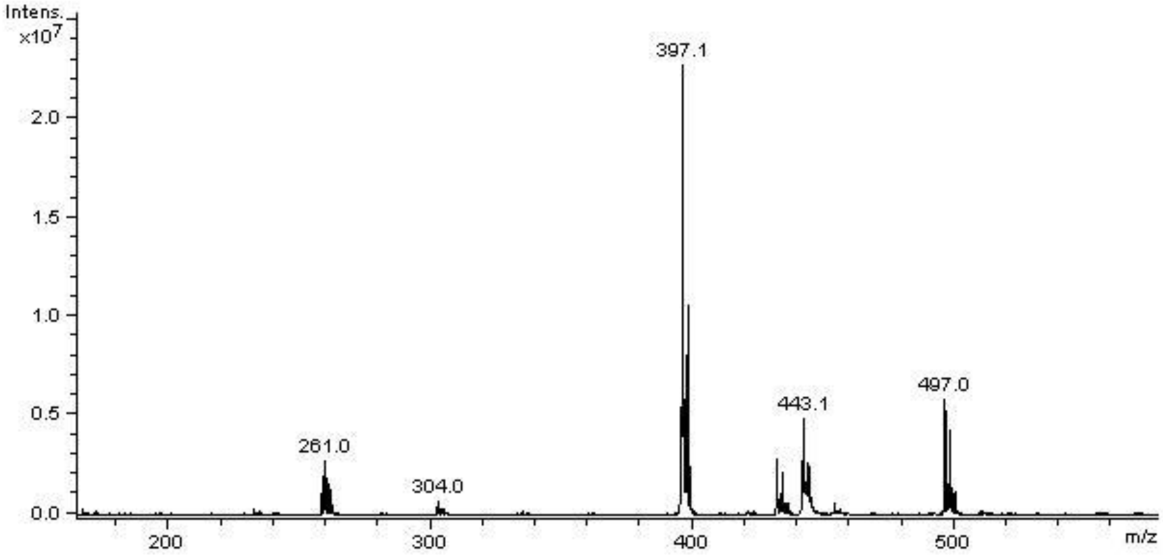

ESI-MS (+) spectrum of the complex $Cu(HL5)(ClO_4)_2$ *(*$4x10^{-5}$*M,* CH_3CN*, m/z)*

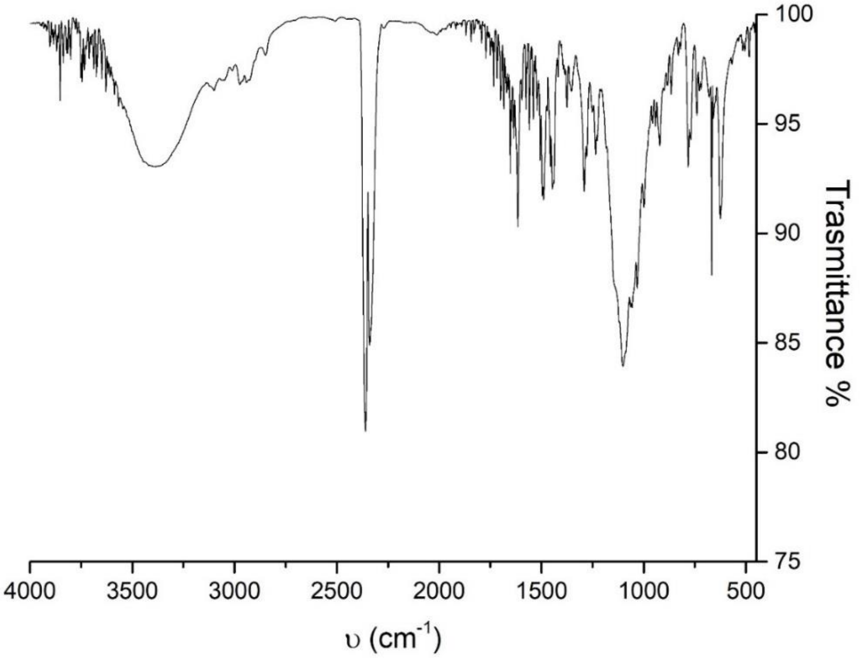

IR spectrum of the complex $Cu(HL5)(ClO_4)_2$ *(KBr)*

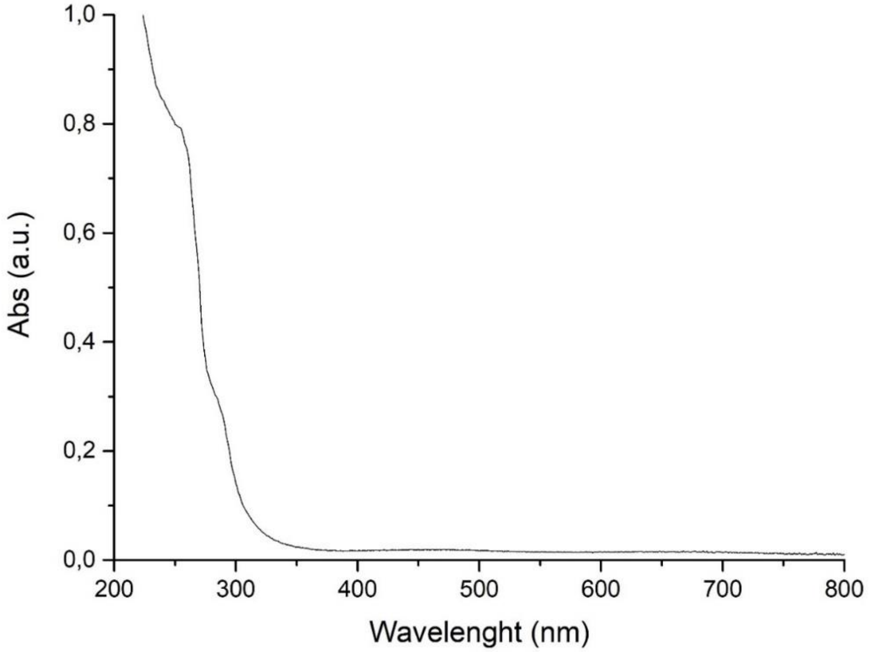

UV-vis spectrum of the complex Cu(HL5)(ClO_4)$_2$ (MeOH 5% v/v/H_2O, 0.1 mM, optical path= 1 cm)

5.1.6 2,6-bis[(bis(2-pyridylmethyl)amino)methyl]-4-methylphenol (HBPMP)

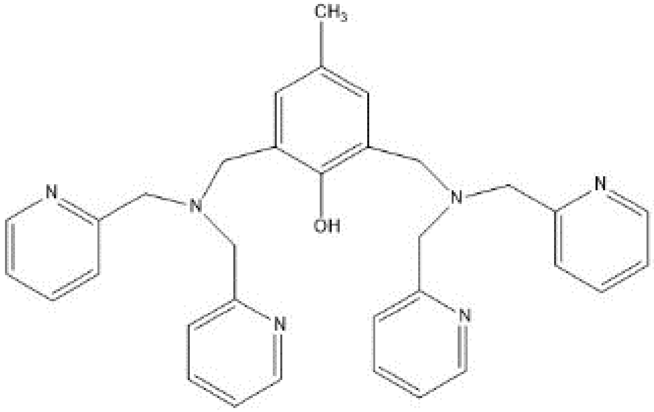

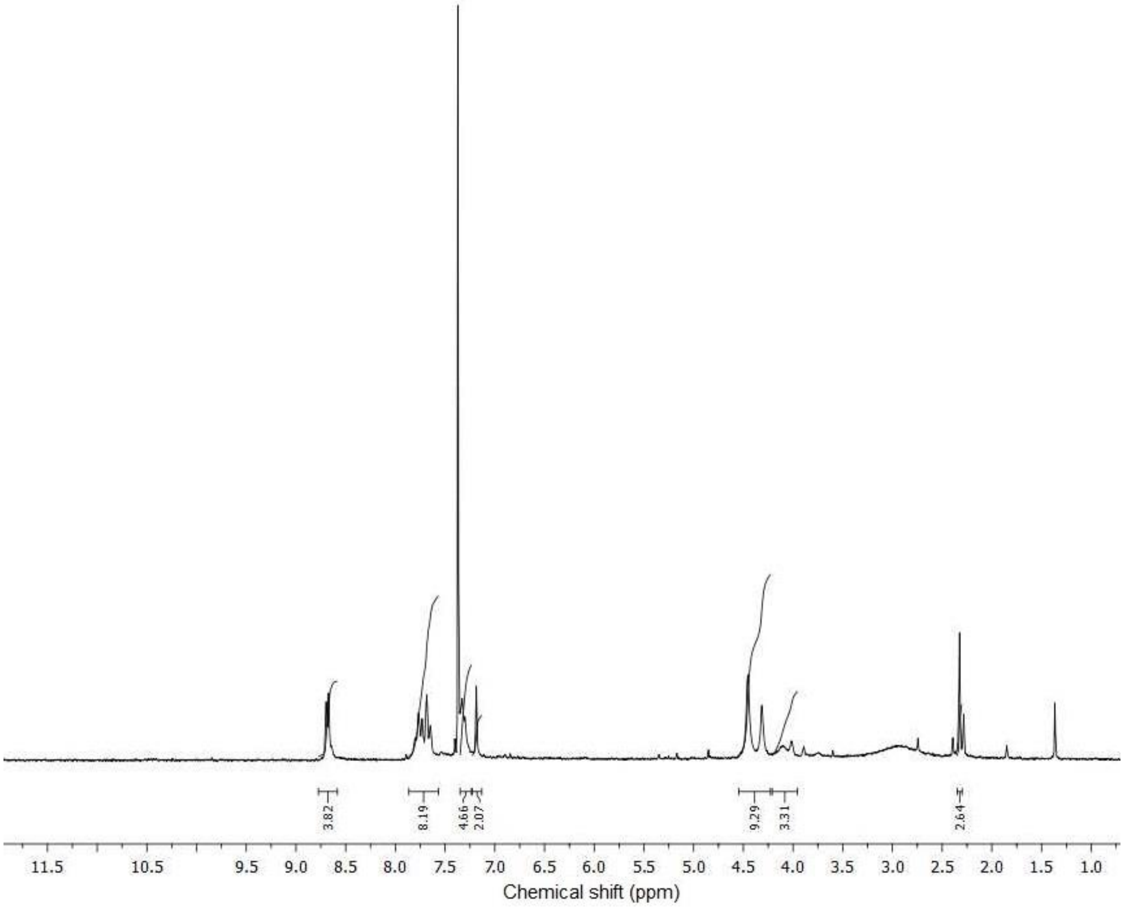

^{1}H-NMR spectrum (200 MHz, $CDCl_3$) of the ligand HBPMP

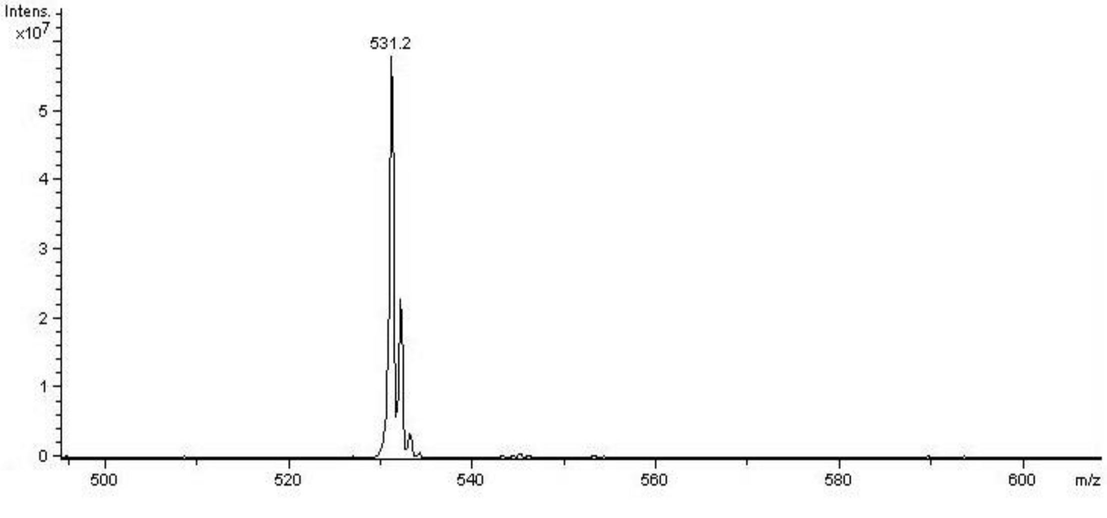

ESI-MS (+) spectrum (CH_3CN, m/z) of the ligand HBPMP

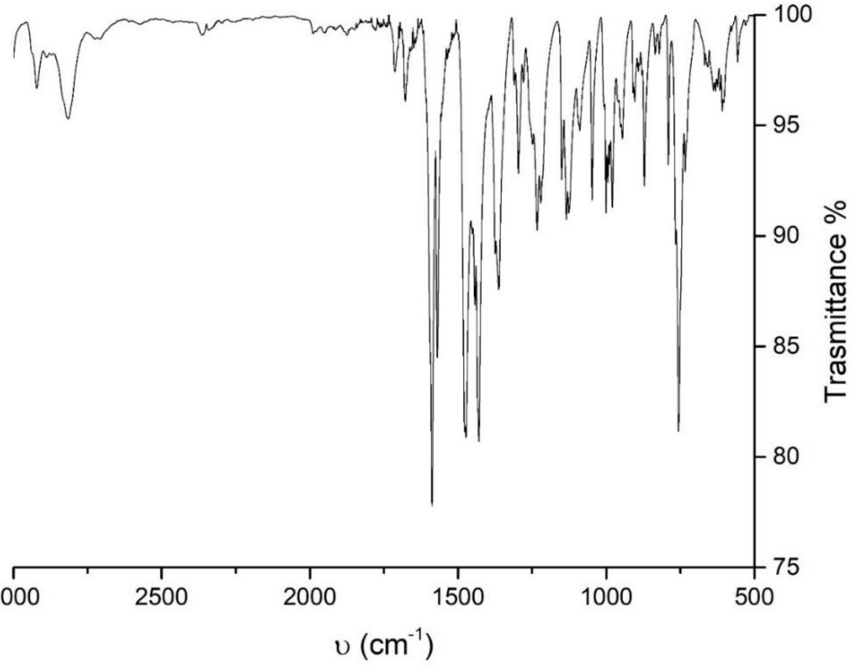

IR spectrum of the ligand HBPMP (KBr)

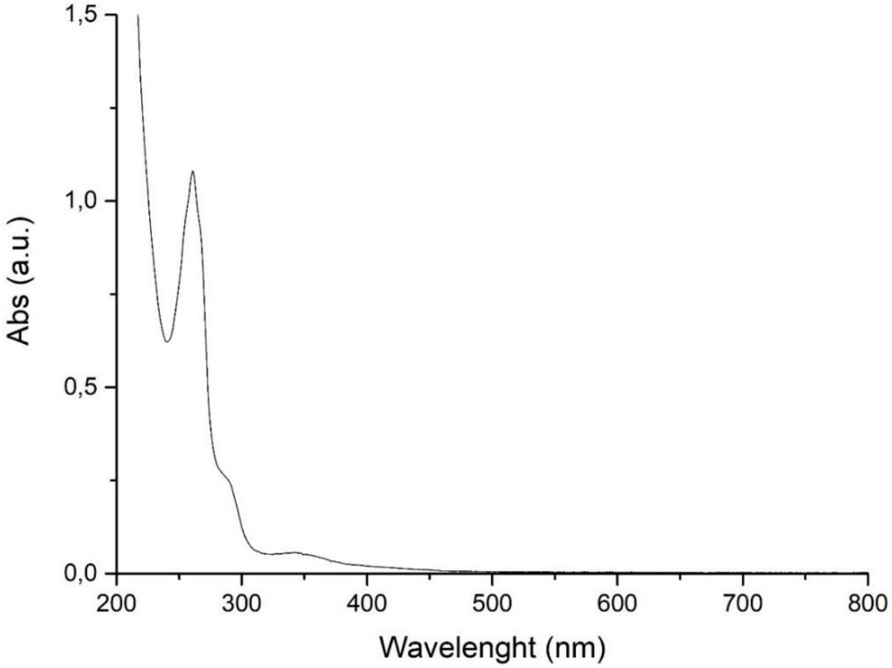

UV-vis spectrum of the ligand HBPMP (MeOH 5% v/v/H_2O, 0.1 mM, optical path= 1 cm)

5.1.7 Complex $Cu_2(BPMP)(H_2O)_2(ClO_4)_3$

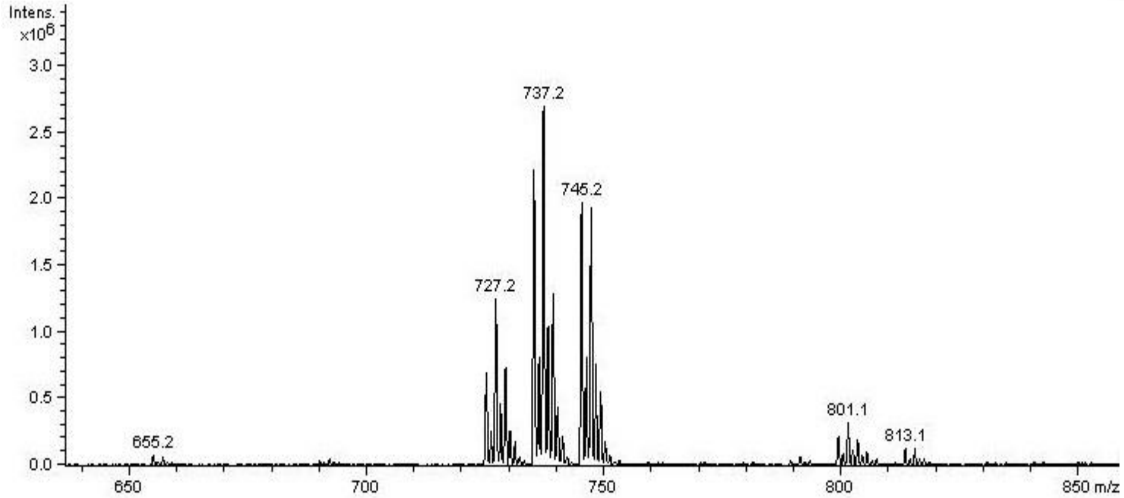

ESI-MS (+) spectrum of the complex $Cu_2(BPMP)(H_2O)_2(ClO_4)_3$ ($5*10^{-5}$M,H_2O, m/z)

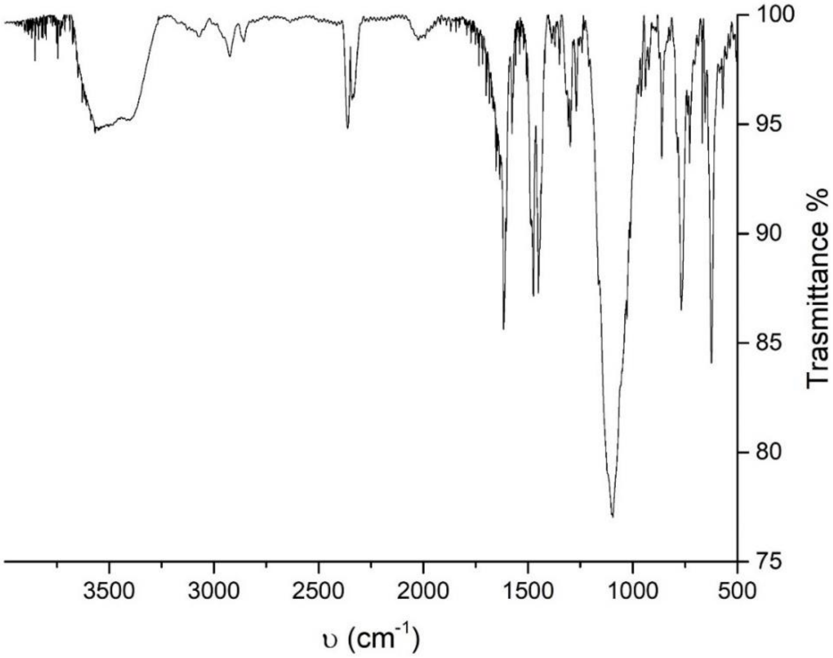

IR spectrum of the complex $Cu_2(BPMP)(H_2O)_2(ClO_4)_3$ (KBr)

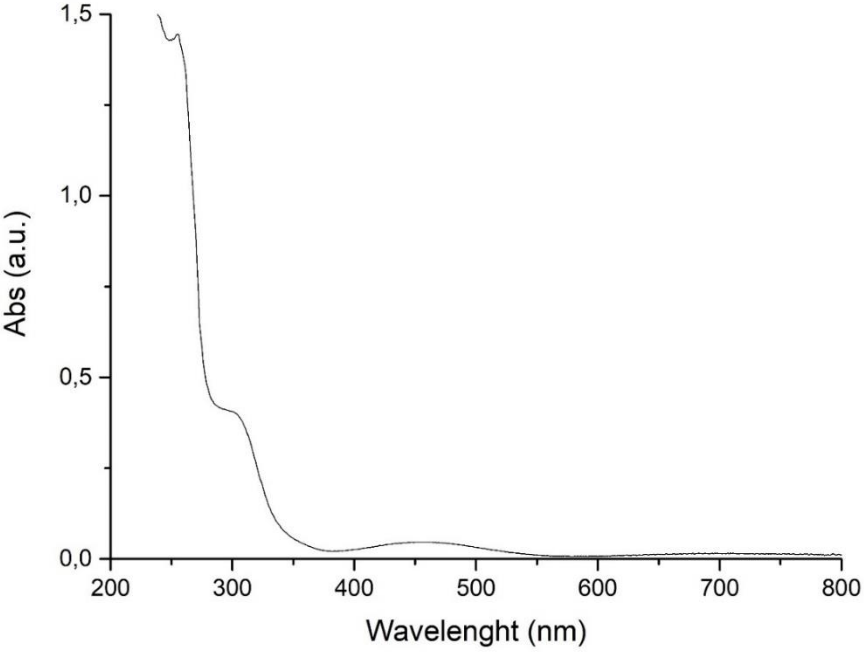

UV-vis spectrum of the complex $Cu_2(BPMP)(H_2O)_2(ClO_4)_3$ (MeOH 5% v/v/H_2O, 0.1 mM, optical path= 1 cm)

5.2 UV-vis titrations

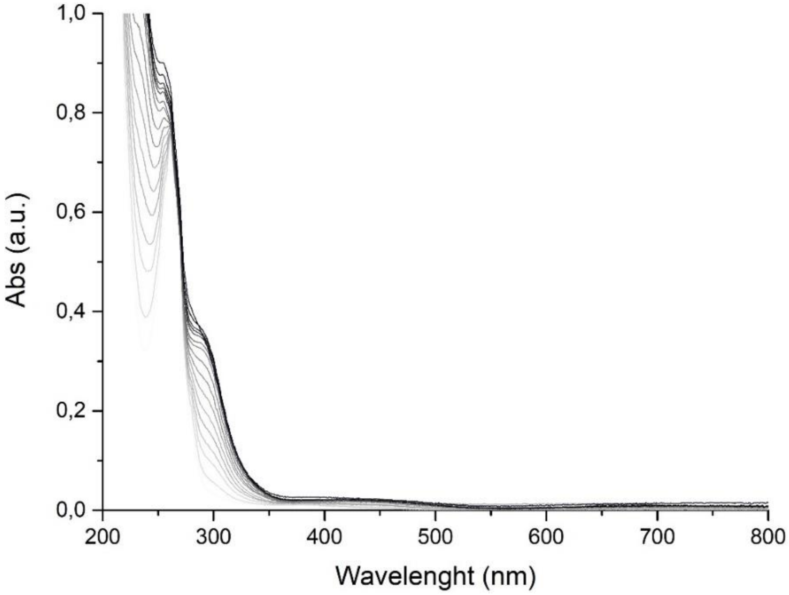

Titration of the ligand HL1 (0.1mM, Cu (II) 0.0-0.2mM H_2O MQ); the light line is the one of the ligand, each change in colour, till black represents the addition of 0.1 equivalent of copper.

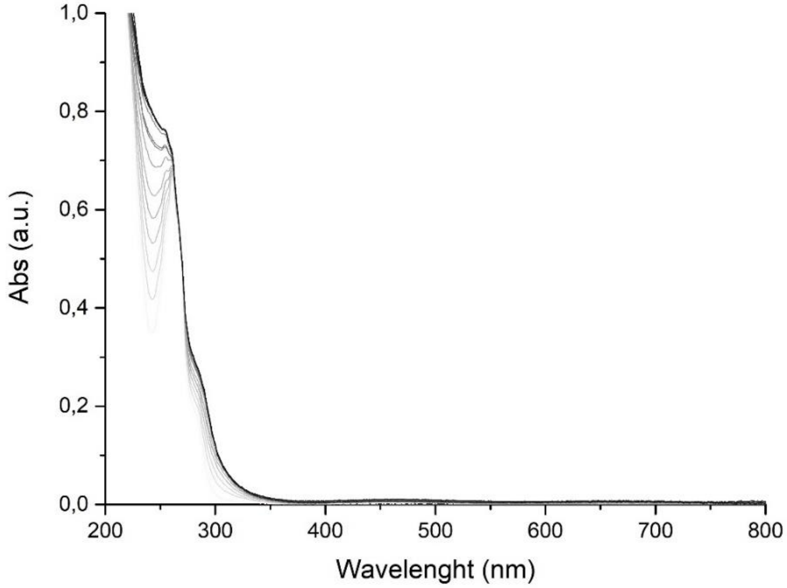

Titration of the ligand HL5 (0.1mM, Cu (II) 0.0-0.2mM H_2O MQ); the light line is the one of the ligand, each change in colour, till black represents the addition of 0.1 equivalent of copper.

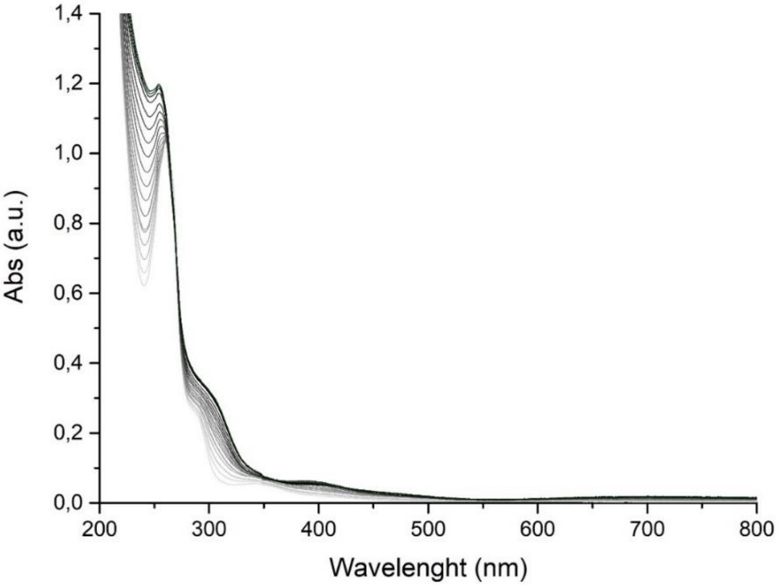

Titration of the ligand HBPMP (0.1mM, Cu (II) 0.0-0.2mM H_2O MQ); the light line is the one of the ligand, each change in colour, till black represents the addition of 0.1 equivalent of copper.

5.3 Peroxidase test

Morine

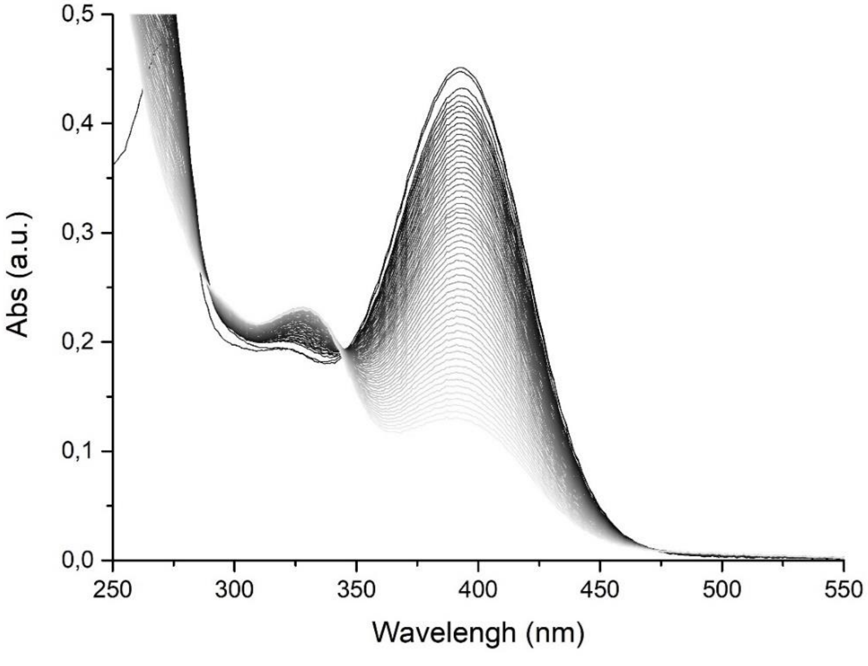

Absorbance variation of the morine, with the complex Cu(HL1)(ClO_4)$_2$. The black line is at t=0, while the light line is at t=18h. The concentration used were: PBS 50mM (0.1 M NaCl, pH=7.8),3.2 μM of Cu(HL1)(ClO_4)$_2$, 10 mM of H_2O_2 and 0.055 mM of morine

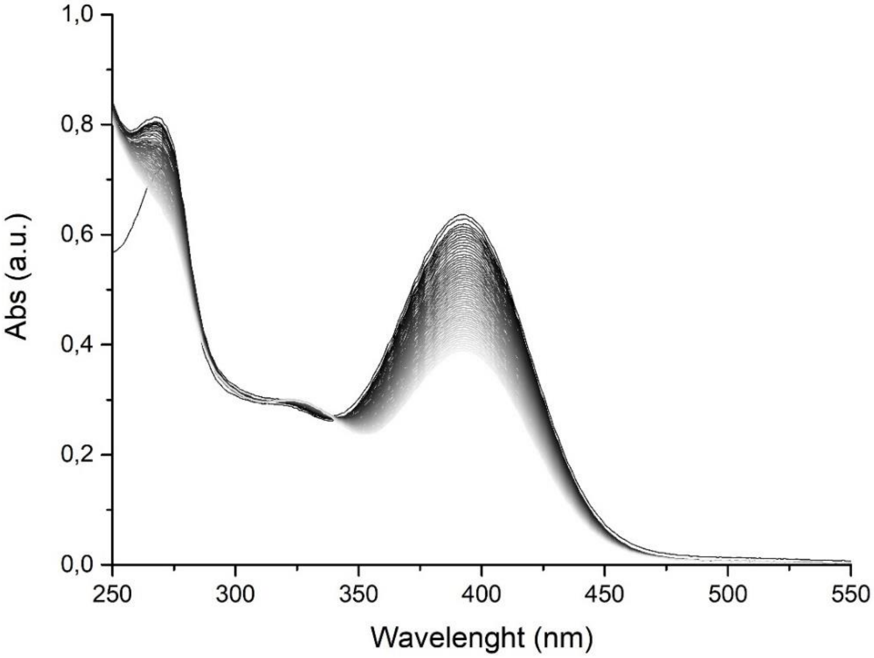

Absorbance variation of the morine, with the complex Cu(HL5)(ClO_4)$_2$. The black line is at t=0, while the light line is at t=18h. The concentration used were: PBS 50mM (0.1 M NaCl, pH=7.8),3.2 µM of Cu(HL5)(ClO_4)$_2$, 10 mM of H_2O_2 and 0.055 mM of morine.

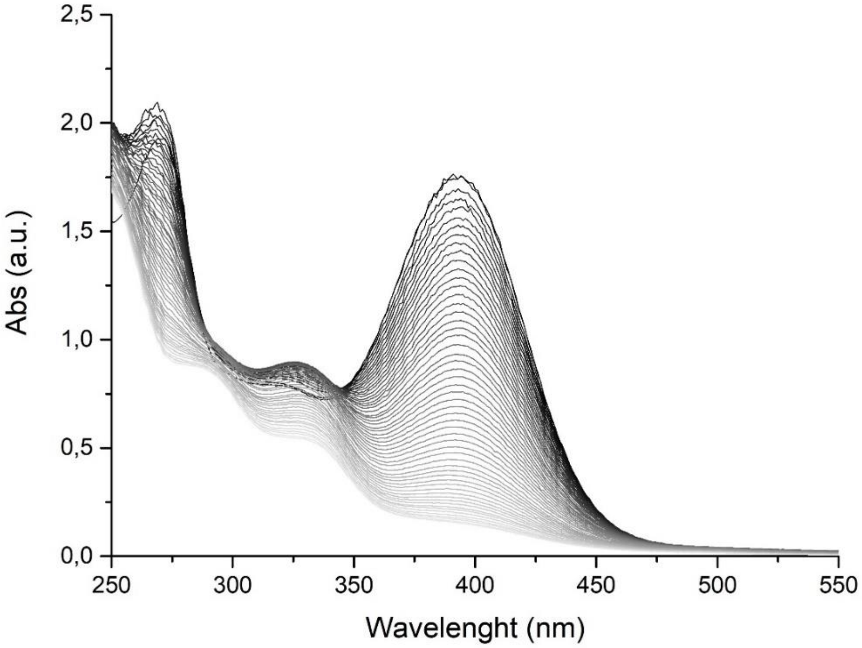

Absorbance variation of the morine, with the complex Cu_2(BPMP)(H_2O)$_2$(ClO_4)$_3$. The black line is at t=0, while the light line is at t=18h. The concentration used were: PBS 50mM (0.1 M NaCl, pH=7.8),3.2 µM of Cu_2(BPMP)(H_2O)$_2$(ClO_4)$_3$, 10 mM of H_2O_2 and 0.055 mM of morine

OPD

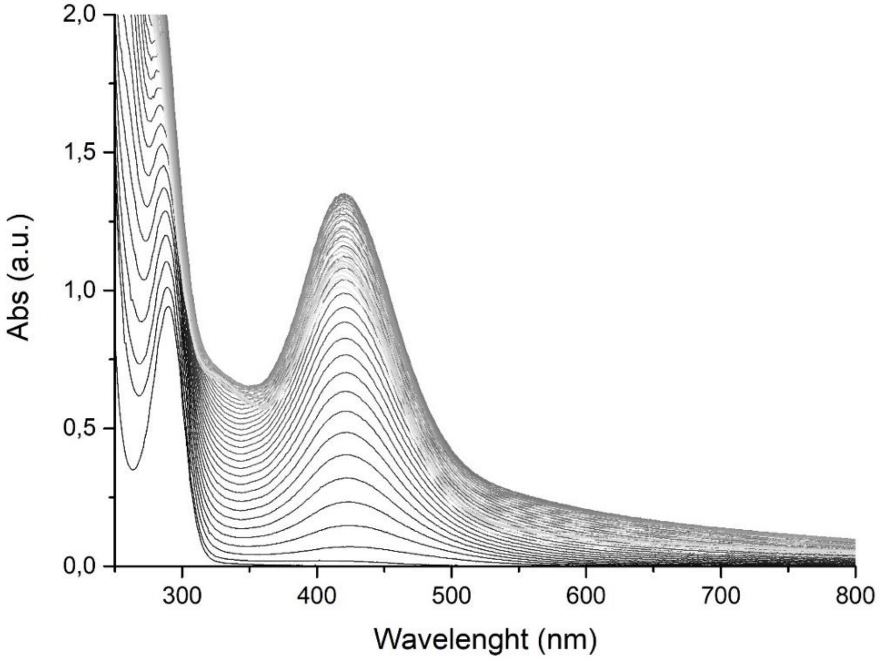

Increase in the absorbance at 420 nm of DAP in the presence of the complex Cu(HL1)(ClO_4)$_2$. The black line is at t=0, while the light line is at t=18h. The concentration used were: PBS 50mM (0.1 M NaCl, pH=7.8),3.2 μM of Cu(HL1)(ClO_4)$_2$, 0.024 M of H_2O_2 and 0.32 mM of OPD.

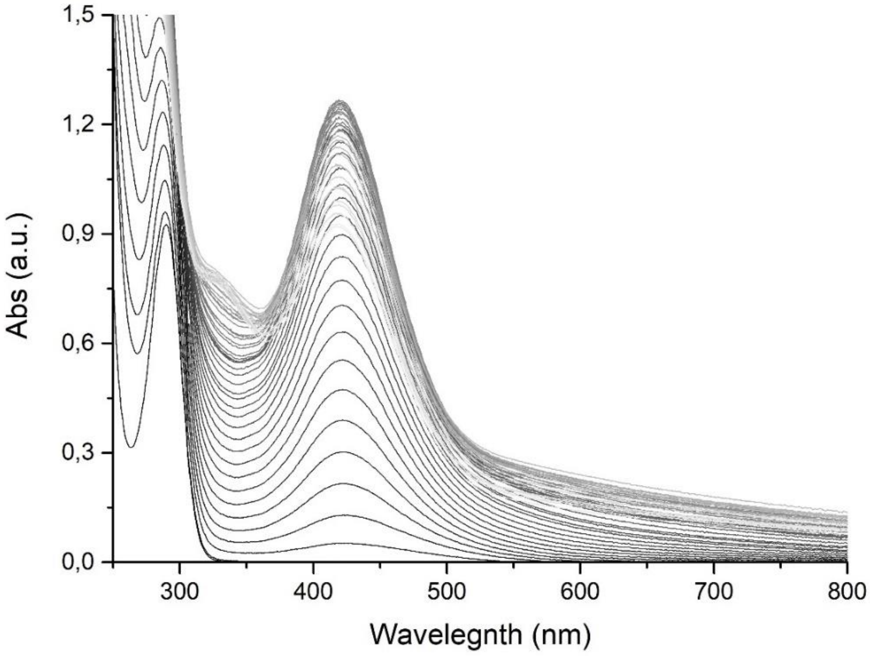

Increase in the absorbance at 420 nm of DAP in the presence of the complex Cu(HL5)(ClO_4)$_2$. The black line is at t=0, while the light green line is at t=18h. The concentration used were: PBS 50mM (0.1 M NaCl, pH=7.8),3.2 μM of Cu(HL5)(ClO_4)$_2$, 0.024 M of H_2O_2 and 0.32 mM of OPD.

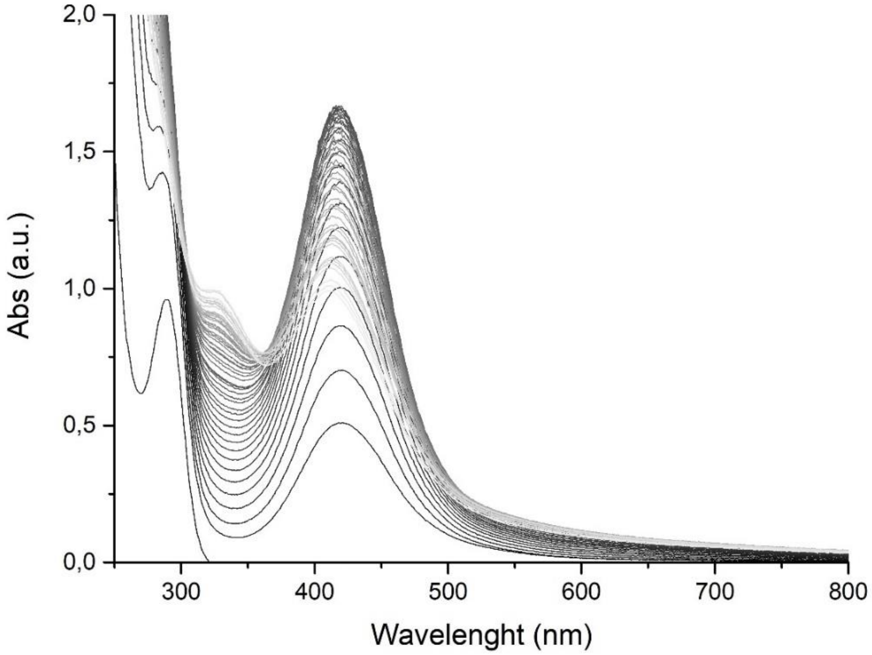

Increase in the absorbance at 420 nm of DAP in the presence of the complex $Cu_2(BPMP)(H_2O)_2(ClO_4)_3$. The black line is at t=0, while the light line is at t=18h. The concentration used were: PBS 50mM (0.1 M NaCl, pH=7.8),3.2 µM of $Cu_2(BPMP)(H_2O)_2(ClO_4)_3$, 0.024 M of H_2O_2 and 0.32 mM of OPD.

Bibliography

---

[1] Przedborski, S.; Vila, M.; Jackson-Lewis, V., *J. Clin. Invest.*, **2003**,111,3.

[2] S Pelak, V.; Hills, W., *Neurodegener. Dis.Manag.*,**2018**, 10.2217/nmt-2017-0030.

[3] Ballard, C.; Gauthier, S.; Corbett, A.; Brayne, C.; Aarsland, D.; Jones, E. *Lancet* **2011**, *377*, 1019–1031.

[4] Rajasekhar, K.; Chakrabarti, M.; Govindaraju, T. *Chem. Commun.* **2015**, *51* (70), 13434–13450.

[5] Vilatela, M.E.A.; López-López, M.; Yescas-Gómez, P.; *Arch. Med. Res.*, **2012**, 43, 622.

[6] Revett, T. J.; Baker, G. B.; Jhamanas, J.; Kar, S., J. Psychiatry Neurosci., 2013, 38 (1), 6-23.

[7] Voet, D.; Voer, J. G.; Pratt, C. W., *Foundamentals of Biochemistry*, third edition, **2017**.

[8] Ke Li; Qing Wei; Fang-Fang Liu; Fan HU; Ao-ji Xie; Ling-Qiang Zhu; Dan Liu, *Mol. Neurobiol.,* **2018**, 55, 3021–3032.

[9] Budimir, A., *Acta Pharm.*, **2011**, 61, 1–14.

[10] Huang, W.; Wei, W.; Shen, Z*., RSC Adv.*, **2014**, 4, 52088.

[11] Hureau, C.; Dorlet, P., *Coord. Chem. Rev*. **2012**, 256, 2175–2187.

[12] Gonzalez-Alvarez, M.; Alzuet, G.; Borras, J.; del Castillo Agudo, L.; Garcia-Granda, S.; Montejo-Bernardo, J. M., *Inorg. Chem.*, **2005**, 44, 9424-9433.

[13] Squarcina, A.; Sorarù, A.; Rigodanza, F.; Carraro, M.; Brancatelli, G.; Carofiglio, T.; Geremia, S.; Larosa, V.; Morosinotto, T.; Bonchio, M., *ACS Catalysis*, **2017**, 0.1021/acscatal.7b00004.

[14] Gaggelli, E.; Kozlowski, H.; Valensin,D.; Valensin, G., *Chem. Rev*., **2006**, 106, 1995−2044.

[15] Butterfield, D. A.; Swomley, A. M.; Sultana, R. *Antioxid. Redox Signal.* **2013**, *19* (8), 823–835.

[16] Santos, M.,A.; Chand, K.; Chaves, S., *Future Med. Chem*, **2016**, 10.4155/fmc-2016-0103.

[17] Kenche, V. B.; Barnham, K. J. *Br. J. Pharmacol.* **2011**, *163*, 211–219.

---

[18] Shariatizi, S.; Meratan, A. A.; Ghasemi, A.; Nemat-Gorgani, M. *Int. J. Biol. Macromol.* **2015**, *80*, 95–106.

[19] Bartolini, M.; Andrisano, V. *ChemBioChem* **2010**, *11* (8), 1018–1035.

[20] Tjernberg, L. O.; Näslund, J.; Lindqvist, F. *J. Biol. Chem.* **1996**, *271* (15), 8545–8548.

[21] Soto, C.; Sigurdsson, E. M. Nat. Med. 1998, 4 (7), 822–826.

[22] Ji, H.F. ; Zhang, H.Y. , *Acta Pharmacol. Sin.*, **2008**, 29, 143–151.

[23] Perry, J. J. P.; Shin, D. S.; Getzoff, E. D.; Tainer, J. A. *Biochim. Biophys. Acta - Proteins Proteomics,* **2010**, *1804* (2), 245–262.

[24] Abreu, I. A.; Cabelli, D. E. *Biochim. Biophys. Acta - Proteins Proteomics* **2010**, *1804* (2), 263–274.

[25] Pierre, J.-L. *Chem. Soc. Rev.* **2000**, *29* (4), 251–257.

[26] Squarcina, A.; Santoro, A.; Hickey, N.; De Zorzi, R.; Carraro, M.; Geremia, S.; Bonchio, M., *un published work*.

[27] Michel, E.; Nauser, T.; Sutter, B.; Bounds, P. L.; Koppenol, W. H. *Arch. Biochem. Biophys.* **2005**, 439, 234-24.

[28] Goldstein, S.; Fridovich, I.; Czapski, G. *Free Radic. Biol. Med.* **2006**, 41, 937-941.

[29] Alfonso-Prieto, M.; Biarnés, X.; Vidossich, P.; Rovira, C. *J. Am. Chem. Soc.* **2009**, 131 (33), 11751–11761.

[30] Signorella, S.; Hureau, C., *Coordination Chemistry Reviews*,**2012**, 56, 1229–1245.

[31] Whittaker, J. W. , *Arch. Biochem. Biophys.* **2012**, *525* (2), 111–120.

[32] Zhou, Y. H.; Tao, J.; Lv, Q. C.; Jia, W. G.; Yun, R. R.; Cheng, Y. *Inorganica Chim. Acta* **2015**, *426*, 211–220.

[33] Haber, A.; Gross, Z., *Chem. Commun.*, **2015**, 51, 5812.

[34] Ribeiro, T. P.; Fernandes, C.; Melo, K. V.; Ferreira, S., S.; Lessa, J., A.; Franco, R. W. A.; Schenk, G.; Pereira, M. D.; Horn A. *Free Radical Biology and Medicine*, **2015**, 80, 67–76.

[35] Pap, J.S.; Kripli, B.; Bors, I.; Bogáth, D.; Giorgi, M.; Kaizer, J.; Speier, G. *J. Inorg. Biochem.*, **2012**, 117, 60-70.

[36] Lu, C.; Guo, Y.; Yan, J.; Luo, Z.; Luo, H. B.; Yan, M.; Huang, L.; Li, X., *J. Med. Chem.*, **2013**, 56, 5843–5859.

---

[37] Dedeoglu, A.; Cormier, K.; Payton, S.; Tseitlin, K. A.; Kremsky, J. N.; Lai, L.; Li, X.; Moir, R. D.; Tanzi, R. E.; Bush, A. I.; Kowall, N. W.; Rogers, J. T.; Huang, X., *Exp. Gerontol*. **2004**, 39, 1641–1649.

[38] Gasque, L.; López-Rosales, A.; Bernès, S.; Mendoza-Díaz, G., *Polyhedron*, **2017**,127, 167–175.

[39] Hamman, J.N.; Rolff, M.; Tuczek, F., *Dalton Trans.*, **2015**, 44, 3251-3258.

[40] Connor, G. P. ; Mayer, K. J. ; Tribble, C. S. ; McNamara, W. R.; *Inorg. Chem.,* **2014**, 53, 5408−5410.

[41] Wendt, F; Rolff, M; Thimm, W.; Nather, C.; Tuczek, F., *Z. Anorg. Allg. Chem.*, **2013**, 639 (14), 2502-2509.

[42] Torelli, S.; Belle, C.; Gautier-Luneau, L.; Pierre, J.L., *Inorg.Chem.*, **2000**, 39, 3526-3536.

[43] Massound, S.,S.; Junk, T.; Mikuriya, M.; Naka, Y., Mautner, *Inorg. Chem. Commun*., **2014**, 50, 48-50.

[44] Zonzinz, M.; *Synthesis and study of ligands for the formation of antioxidant metallic complexes*, Master thesis, **2016-2017.**

[45] Kafentzi, M.C.; Papadakis, R.; Gennarini,F.; Kochem,A.;Iranzo, O.; Le Mest, Y.; Le Poul, N.; Tron, T.; Faure, B.; Simaan, A. J.; Réglier, M., *Chem. Eur. J.,* **2018**, 24, 5213 – 5224.

[46] Khalil, M. M.; Mahmoud, R. K.; *Journal of Saudi Chemical Society*,**2016**, 20, 607–614.

[47] Iranzo, O., *Bioinorganic Chemistry*, **2011**, 39, 73-87.

[48] Jitsukawa, K.; Harata, M., Arii, H.; Sakurai, H.; Masuda, H., *Inorg. Chem. Acta*, **2001**, 324, 108-116.

[49] Ramadan, M.; *Journal of Coordination Chemistry,* **2012,** 65 (8), 1417–1433.

[50] McCord, J.,M.; Fridovich, I., *The Journal of Biological Chemistry*, **1969**, 244 (22), 6049-6055.

[51] Fridovich, I.; *Ann. Rev. Pharmacol. Toxicol*., **1983**, 23, 239-257.

[52] Abuhijleh, A.; Khalaf, J., *European Journal of Medical Chemistry*, **2010**, 45, 3811-3817.

---

[53] Beloglazkina, K. E.; Barskaya, E.S.; Majouga, A. G.; Zyk, N. V., *Mendeleev Commun.*, **2015**, 25, 148-149

[54] Durackova, Z.; Mendiola, M. A.; Sevilla, M. T.; Valent, A., *Bioelectrochemistry and Bioenergetics*, **1999**, 48, 109–116.

[55] Saczewski, F.;Dziemidowicz-Borys, E.; Bednarski, P. J.; Grunert, R.; Gdaniec, G.; Tabin, P., *Journal of Inorganic Biochemistry*, **2006**, 100, 1389–1398.

[56] Batianic-Haberle I., Rebouc J. L. S.¸ Spasojevic´ I., *Antioxid. Redox Signal*., **2010**,13, 877.

[57] Martins, D.; English, A. M., *Redox Biology*, **2014**, 2, 308-313.

[58] Gao, J.; Martell, A. E.; Reibenspies, J. H.; *Inorganica Chimica Acta*, **2003**, 346, 32-42.

[59] Hureau, C.; Faller, P., *Biochimie*, **2009**, 91, 1212-1217.

[60] Cassagnes, L. E.; Hervé, V.; Nepveu, F.; Hureau, C.; Faller,P.; Collin, F., *Angew. Chem. Int. Ed.* **2013**, 52, 11110 –11113.

[61] Sheldrick, G. M. , *Acta Crystallogr*., Sect. A: Found. Crystallogr., **2008**, 64, 112.

[62] Müller, *Crystallogr. Rev*., **2009**, 15, 57.

[63] Müller, P. ; Herbst-Irmer, R. ; Spek, A. L. ; Schneider, T. R. ; Sawaya, M. R., *Crystal Structure Refinement: A Crystallographer's Guide to SHELXL*, ed. P. Müller, IUCR Texts on Crystallography, Oxford University Press, Oxford, **2006.**

Acknolwdgments

Ringrazio il mio relatore, il Prof. Mauro Carraro, per avermi accolto nel suo gruppo di ricerca e per avermi seguito in questo percorso con disponibilità, pazienza ed entusiasmo.

Ringrazio il mio controrelatore, il Porf. Andrea Biffis, per la disponibilità e l'interessamento mostrati nei colloqui e le osservazioni costruttive al fine di migliorare questo studio.

Grazie a Martina e Mirko, per avermi seguito nei primi mesi nell'attività di laboratorio, insegnandomi le cose con pazienza, per l'estrema disponibilità e gentilezza a qualsiasi dubbio o richiesta.

Thanks to Professor Justyna Brasun to welcome me in her research group and to follow me during the period in Wroclaw. You make me feel like home and I can only be grateful for this.

Grazie a tutti gli altri componenti del gruppo NanoMolCat: la Prof. Marcella Bonchio, il Dott. Andrea Sartorel, la Dott.ssa Nadia Marino, il Dott. Luca Dell'Amico, il Dott. Xavier Companyo, Andrea, Francesco, Alessio, Javier, Katia, Hadi, Jiaying e tutti i laureandi per tutti i momenti condivisi insieme.

Grazie ai miei genitori, per avermi seguito durante questo percorso di studi supportandomi economicamente e moralmente. A mia Mamma, che mi ha sempre spronato a dare il meglio di me e a non abbattermi mai, quando un esame non andava bene. A mio Papà che mi ha accompagnato alla stazione di Verona Porta Nuova almeno 280 volte in questi 5 anni. Grazie per tutte le volte che mi hai aspettato quando il treno era in ritardo, mentre a casa c'era l'Inter che giocava la Champions. Grazie per esserci sempre.

Grazie ai nonni vicini e lontani e a tutti i parenti che durante questi anni si sono interessati al mio percorso di studi.

Grazie a Ilaria e Raffaella, che ci sono sempre state.

Grazie alle mie coinquiline Alessandra e Veronica, che sono state molto di più di due ragazze con cui ho condiviso una casa per 3 anni. Abbiamo vissuto gioie e dolori, delusioni ma anche molte soddisfazioni. Grazie per tutte le risate e tutti i momenti condivisi insieme.

Grazie a Elisa, una compagna di corso speciale e tutti gli amici di Padova, agli amici di spritz in questi anni.

Grazie agli amici di Rosegaferro, per tutti i pranzi, feste, capannine e vacanze trascorse insieme.

Grazie al mio Nicola, che ha creduto in me più di quanto io non creda in me stessa. Non sarei la persona che sono se non ti avessi al mio fianco.